

MR-GUIDED REAL-TIME CONVECTION-ENHANCED DELIVERY

By

GARRETT WILLIAM ASTARY

A DISSERTATION PRESENTED TO THE GRADUATE SCHOOL  
OF THE UNIVERSITY OF FLORIDA IN PARTIAL FULFILLMENT  
OF THE REQUIREMENTS FOR THE DEGREE OF  
DOCTOR OF PHILOSOPHY

UNIVERSITY OF FLORIDA

2011

© 2011 Garrett William Astary

To my parents, Bill and Marile, and sister, Allison

## ACKNOWLEDGMENTS

I would like to thank my co-advisors, Dr. Malisa Sarntinoranont and Dr. Thomas H. Mareci, for their guidance and support throughout my tenure as a graduate student. Dr. Sarntinoranont provided encouragement and advice that was especially helpful when experiments were not initially successful. Her thoughtful ideas and constructive criticism made the work described in this dissertation possible. Dr. Sarntinoranont has also been an excellent teacher willing to explain fundamental concepts in fluid and tissue mechanics strengthening my abilities as an engineer. Dr. Mareci has been a wonderful mentor and has taught me to think critically as a scientist and to carefully consider all details of an experiment. He has played an instrumental role in my ability to thoroughly analyze data to be attentive to details when organizing and presenting results. He has also been an amazing tutor regarding all things MRI. His knowledge has inspired me to learn as much as I can and, perhaps more importantly, to recognize topics that I need to understand more completely. I would also like to thank the other members of my committee, Dr. Paul R. Carney and Dr. Stephen J. Blackband. Dr. Carney allowed me to use his lab for experimental procedures and has given great insight into the clinical relevance of our work. Dr. Blackband has provided advice and opened his lab to me allowing me to use supplies including the infusion pump used for all CED experiments.

I would also like to thank my lab mates who really shaped my graduate school career. Hector Sepulveda (Federal Bureau of Investigation) and Dr. Xiaoming Chen (Fox Chase Cancer Center) were instrumental in my learning the MR system and performing my first experiments as a graduate student. Dr. Greg L. Pishko (Oregon Health and Science University) provided excellent brainstorming sessions and advice for initial experiments. William Triplett provided coding expertise and had many

thoughtful suggestions regarding the analysis of my data. Luis Colon Perez has been helpful with experiments, a great friend, and a physics tutor. Sung Jin Lee was always willing to help with experiments, is a pleasure to be around and is an amazing experimentalist. I would also like to thank Svetlana Kantorovich for everything she has done to throughout my graduate career including performing rodent surgeries, teaching me surgical procedures, helping with imaging set up and performing histology. I would also like to thank other members of Dr. Carney's and Dr. Sarntinoranont's labs: Dr. Mansi B. Parekh, Dr. Rabia Zafar, Dr. Stephen Myers, Magdoom Mohamed, Fernando Cassonova, Tatiana Nobrega and Dai Wei for their help and support throughout my graduate school career.

I would also like to thank members of the AMRIS staff for their help with MR imaging experiments. Barbara Beck and Kelly Jenkins provided excellent guidance in the construction of my RF coil and were always willing to help with issues regarding MR hardware. Dr. Huadong Zeng was accommodating when scheduling imaging experiments and willing to troubleshoot any issues with the instruments. Jim Rocca was also a friendly face that would check on us during late imaging experiments. Additionally I would like to thank Dr. Mark Meisel, Marcus Peprah, Dr. Michelle Manuel, and Charles Fisher for their guidance and assistance in completing the susceptibility-matched alloys work.

Finally, I would like to thank my family and friends who have supported me in graduate school and throughout my life. Susan Craft has been my best friend throughout graduate school and has supported me in every way possible and kept me strong during times of adversity. My sister, Allison, has shown unconditional love and

support for her older brother. My parents, Bill and Marile, have been supportive my entire life, are wonderful people and have shaped the person I am today. I am forever grateful to have them in my life.

# TABLE OF CONTENTS

	<u>page</u>
ACKNOWLEDGMENTS.....	4
LIST OF TABLES.....	10
LIST OF FIGURES.....	11
LIST OF ABBREVIATIONS.....	14
ABSTRACT.....	16
CHAPTER	
1 MOTIVATION AND SPECIFIC AIMS.....	18
1.1 Motivation.....	18
1.2 Specific Aims.....	20
1.2.1 Specific Aim 1: Develop MR Imaging Methodology for Evaluating Contrast Agent Distributions in the Rat Hippocampus <i>In Vivo</i> following CED.....	21
1.2.2 Specific Aim 2: Measure Gd-Albumin <i>In Vivo</i> Relaxivity in the Rat Thalamus at 11.1 T.....	22
1.2.3 Specific Aim 3: Design and Test a Susceptibility-Matched Metal Alloy....	23
2 BACKGROUND AND PREVIOUS STUDIES.....	24
2.1 The Central Nervous System and the Blood-Brain Barrier.....	24
2.2 Convection-Enhanced Delivery.....	27
2.3 Magnetic Resonance Imaging.....	33
2.3.1 Overview.....	33
2.3.2 Magnetic Susceptibility.....	39
2.3.3 Relaxation Theory.....	47
2.3.3.1 Background.....	47
2.3.3.2 Spectral density function.....	52
2.3.3.3 Relaxation in nervous tissue.....	53
2.3.4 Contrast Agents.....	57
2.3.4.1 Background.....	57
2.3.4.2 Measurement.....	60
2.3.4.3 Determining contrast agent concentration.....	63
3 DEVELOPMENT OF MR IMAGING METHODOLOGY FOR EVALUATING CONTRAST AGENT DISTRIBUTIONS IN RAT NERVOUS TISSUE IN VIVO FOLLOWING CED.....	75
3.1 Introduction.....	75

3.2	Methods .....	78
3.2.1	Infusion System .....	78
3.2.2	Animal Preparation .....	79
3.2.3	MR Imaging .....	81
3.2.3.1	Initial studies .....	81
3.2.3.2	Extended studies .....	82
3.2.4	Image Segmentation .....	82
3.3	Results .....	83
3.3.1	Initial Studies .....	83
3.3.2	Extended Studies .....	86
3.4	Discussion .....	90
3.4.1	Distribution Profiles.....	91
3.4.2	Image Segmentation .....	93
3.4.3	Inline Pressure Measurements.....	98
3.4.4	Advantages and Limitations of MR Imaging .....	99
3.5	Conclusions .....	101
4	MEASUREMENT OF GD-ALBUMIN IN VIVO RELAXIVITY IN THE RAT THALAMUS AT 11.1 T.....	109
4.1	Introduction .....	109
4.2	Methods .....	112
4.2.1	MR Phantom Preparation .....	112
4.2.2	Animal Preparation and Surgical Procedures .....	113
4.2.3	MR Imaging .....	115
4.2.3.1	Phantom measurements .....	115
4.2.3.2	Rat brain <i>in vivo</i> .....	115
4.2.4	Measurement of Gd-albumin Concentration in Tissue.....	116
4.2.5	Data Analysis and Statistical Methods.....	118
4.3	Results .....	120
4.3.1	Relaxivity of Gd-albumin in aCSF.....	120
4.3.2	<i>In Vivo</i> Relaxivity of Gd-albumin in the Rat Thalamus.....	120
4.3.2	CED Concentration Profiles.....	122
4.4	Discussion .....	124
4.4.1	Gd-albumin Relaxivity in aCSF.....	124
4.4.2	Gd-albumin Relaxivity <i>In Vivo</i> .....	126
4.4.3	CED Concentration Profiles.....	130
4.5	Conclusions .....	133
5	DESIGN AND TEST A SUSCEPTIBILITY-MATCHED METAL ALLOY .....	142
5.1	Introduction .....	142
5.2	Theory.....	145
5.2.1	Simulation of Magnetic Field Perturbations .....	146
5.2.2	MR Measurement of Magnetic Field Perturbations .....	147
5.3	Methods .....	149
5.3.1	Preparation of Cu-Sn Alloys .....	149

5.3.2 SQUID Magnetometry .....	150
5.3.3 MR Imaging .....	152
5.3.4 Mapping B Field Perturbations .....	153
5.3.5 Estimating Magnetic Susceptibility .....	154
5.3.6 Data Analysis .....	154
5.4 Results .....	155
5.4.1 Cu-Sn Alloys.....	155
5.4.2 Mapping B Field Perturbations .....	155
5.4.3 Estimating Magnetic Susceptibility .....	157
5.5 Discussion .....	160
5.6 Conclusions .....	165
6 CONCLUSIONS AND FUTURE WORK .....	179
6.1 Summary .....	179
6.2 Future Work .....	181
LIST OF REFERENCES .....	185
BIOGRAPHICAL SKETCH .....	197

## LIST OF TABLES

<u>Table</u>		<u>page</u>
4-1	Summary of measured Gd-albumin relaxivity values.....	138
4-2	P-value of statistical comparisons between Gd-albumin $r_1$ relaxivity measured for various sample preparations. ....	138
4-3	P-value of statistical comparisons between Gd-albumin $r_2$ relaxivity measured for various sample preparations. ....	138
5-1	Comparison of $\chi_{v,obj}$ estimations performed at 4.7 T using line fit and image fit methods to SQUID magnetometry measurements. ....	171
5-2	Comparison of $\chi_{v,obj}$ estimations performed at 11.1 T using line fit and image fit methods to SQUID magnetometry measurements ....	171
5-3	Influence of image resolution on $\chi_{v,obj}$ estimations using the line fit method at 4.7 T. ....	176
5-4	Influence of image resolution on $\chi_{v,obj}$ estimations using the image fit method at 4.7 T. ....	176

## LIST OF FIGURES

<u>Figure</u>	<u>page</u>
2-1 Schematic of intrinsic bulk fluid flow in the brain.....	66
2-2 Schematic of albumin concentration profiles in brain GM due to diffusion-driven transport and CED. ....	67
2-3 Schematic of Fourier imaging. ....	68
2-4 A comparison of gradient echo MR images and simulated images of an aluminum cylinder at 11.1 T at two different bandwidths. ....	68
2-5 Simulations of artifact generated in spin echo (SE), gradient echo (GE), and echo planar (EPI) images by a 0.44 cm diameter cylinder ( $\chi_{v,obj} = -14$ ppm) immersed in water ( $\chi_{v,med} = -9.04$ ppm) at multiple field strengths.....	69
2-6 Simulations of artifact generated in spin echo (SE), gradient echo (GE), and echo planar (EPI) images by a 0.44 cm diameter tungsten cylinder ( $\chi_{v,obj} = 50$ ppm) immersed in water ( $\chi_{v,med} = -9.04$ ppm) at multiple field strengths.....	70
2-7 Simulations of artifact generated in gradient echo images by a 0.44 cm diameter cylinder ( $\chi_{v,obj} = -14$ ppm) immersed in water ( $\chi_{v,med} = -9.04$ ppm) at 11.1 T as a function of bandwidth and echo time. ....	71
2-8 Simulations of artifact generated in spin echo images by a 0.44 cm diameter cylinder ( $\chi_{v,obj} = -14$ ppm) immersed in water ( $\chi_{v,med} = -9.04$ ppm) at 11.1 T as a function of bandwidth and echo time. ....	72
2-9 Schematic of fluctuating fields due to intramolecular dipole-dipole interaction... ..	73
2-10 Examples of spectral density functions and their effect on $T_1$ and $T_2$ . ....	74
3-1 Sagittal images of a single rat demonstrating the apparent disconnect between the dorsal and ventral hippocampus. ....	103
3-2 High-resolution $T_1$ -weighted MR images of dorsal hippocampus infusions. ....	103
3-3 High-resolution $T_1$ -weighted MR images of ventral hippocampus infusions. ....	104
3-4 High-resolution $T_1$ -weighted MR image coronal slice of the dorsal hippocampus distribution volume and ventral hippocampus and corresponding segmentation. ....	104
3-5 Inline pressure measurements and corresponding MR images for mild and severe backflow.....	105

3-6	DCE-MR images of Gd-albumin infusion into dorsal hippocampus..	106
3-7	DCE-MR images of Gd-albumin infusion into the ventral hippocampus..	107
3-8	Schematic of transport properties in the rat dorsal and ventral hippocampus. .	108
4-1	The experimental setup used for measurements of Gd-albumin relaxivity in solution. ....	134
4-2	The experimental setup used for measurements of Gd-albumin relaxivity <i>in vivo</i> . ....	134
4-3	T <sub>1</sub> -weighed MR images of the four infusion sites in the rat thalamus .....	135
4-4	Relaxivity of Gd-albumin in aCSF.....	136
4-5	Linear regression was performed on relaxation time versus concentration data to determine the r <sub>1</sub> and r <sub>2</sub> relaxivity of Gd-albumin with Evans blue dye in the rat thalamus <i>in vivo</i> . ....	137
4-6	Sensitivity of relaxivity curve fit to measured porosity.....	137
4-7	The relaxivity of Gd-albumin measured in the rat thalamus <i>in vivo</i> was used to calculate concentration profiles of Gd-albumin infused into the rat dorsal hippocampus during CED.....	139
4-8	The relaxivity of Gd-albumin measured in the rat thalamus <i>in vivo</i> was used to calculate concentration profiles of Gd-albumin infused into the rat ventral hippocampus during CED.....	140
4-9	Schematic of the rat dorsal and ventral hippocampus adapted from the Paxinos rat atlas (Paxinos and Watson, 1998) with high-resolution MR images of the final contrast agent distribution. ....	141
5-1	Pictorial summary of method used to simulate magnetic field perturbations based on an arbitrary susceptibility distribution .....	166
5-2	Simulated magnitude images of a cylindrical object ( $\chi_{v,obj} = -14$ ppm) immersed in water ( $\chi_{v,media} = -9.05$ ppm) acquired with a spin echo (SE), gradient echo (GE), and echo planar (EPI) imaging sequence at 11.1 T. ....	167
5-3	Experimental setup for MR measurements.....	167
5-4	Phase maps of complex-divided asymmetric spin echo images with a difference in free precession delay times of 0 ms, 0.375 ms and 2.0 ms..	168
5-5	Flow-chart summarizing the process of estimating $\chi_{v,obj}$ from $\Delta B_{z,MR}$ .....	169

5-6	$\Delta B_{z,MR}$ maps acquired at 4.7 T for cylindrical Cu-Sn alloy samples composed of 1.5%, 3%, 5% and 7% Sn. ....	170
5-7	Comparison of $\Delta B_{z,MR}$ maps, normalized by acquisition field strength ( $B_0 = 4.7$ T or 11.1 T), for alloys composed of 3% Sn and 5% Sn. ....	170
5-8	Summary of $\chi_{v,obj}$ for each of the Cu-Sn alloys measured using SQUID magnetometry and estimated using the method outlined in this study at 4.7 T and 11.1 T. ....	172
5-9	Comparison of $\Delta B_{z,MR}$ and $\Delta B_{z,Sim}$ simulated using MR-derived measurements of $\chi_{v,obj}$ using the image fit method at 4.7 T. ....	173
5-10	Comparison of $\Delta B_{z,MR}$ and $\Delta B_{z,Sim}$ simulated using MR-derived measurements of $\chi_{v,obj}$ using the image fit method at 11.1 T. ....	174
5-11	The effect of in-plane resolution on MR-derived measurements of $\chi_{v,obj}$ for the line fit and image fit methods. ....	175
5-12	MR-derived measurements of $\chi_{v,obj}$ were performed on the 3.0% sample measured at 11.1 T after modulating the simulation model geometry. ....	177
5-13	Comparison of $\Delta B_{z,MR}$ collected at 4.7 T along a line profile in the phase encoding direction for the four Cu-Sn alloys. ....	178

## LIST OF ABBREVIATIONS

aCSF	artificial cerebrospinal fluid
AP	anterior-posterior anatomical direction
BBB	blood-brain barrier
BW	bandwidth
CA	cornu ammonis subfield of the hippocampus
CED	convection-enhanced delivery
CNS	central nervous system
CSF	cerebrospinal fluid
Cu	element abbreviation for copper
DCE-MRI	Dynamic contrast-enhanced magnetic resonance imaging
DV	dorsal-ventral anatomical direction
DWI	diffusion-weighted imaging
ECS	extracellular space
EEG	electroencephalography
EPI	echo planar imaging
fMRI	functional magnetic resonance imaging
FOV	field of view
Gd-albumin	human serum albumin labeled with gadolinium chelated by diethylene triamine pentaacetic acid, macromolecular magnetic resonance imaging contrast agent
Gd-DTPA	gadolinium chelated by diethylene triamine pentacetic acid, low molecular weight magnetic resonance imaging contrast agent
GE	gradient echo
GM	gray matter tissue in central nervous system
ICP-AES	inductively-coupled plasma atomic emission spectroscopy

ICP-MS	inductively-coupled plasma mass spectroscopy
ISF	interstitial fluid
ML	medial-lateral anatomical direction
MRI	magnetic resonance imaging
mRt	mesencephalic reticular formation, subregion of thalamus
NMR	nuclear magnetic resonance
ofMRI	functional magnetic resonance imaging applied to studying optical genetics
Po	posterior thalamic nuclear group, subregion of the thalamus
QSM	quantitative susceptibility mapping, an MRI method
$r_1$	longitudinal relaxivity of a contrast agent, lowercase “r” is used to avoid confusion with longitudinal relaxation rate ( $R_1$ )
$r_2$	transverse relaxivity of a contrast agent, lowercase “r” is used to avoid confusion with transverse relaxation rate ( $R_1$ )
RF	radiofrequency
ROI	region(s) of interest
SE	spin echo
Sn	elemental abbreviation for tin
SNR	signal-to-noise ratio
SQUID	superconducting quantum interference device
T	Tesla
$T_1$	longitudinal relaxation time constant
$T_2$	transverse relaxation time constant
TE	echo time
TR	recovery time
WM	white matter tissue in central nervous system

Abstract of Dissertation Presented to the Graduate School  
of the University of Florida in Partial Fulfillment of the  
Requirements for the Degree of Doctor of Philosophy

MR-GUIDED REAL-TIME CONVECTION-ENHANCED DELIVERY

By

Garrett William Astary

December 2011

Chair: Malisa Sarntinoranont  
Cochair: Thomas H. Mareci  
Major: Biomedical Engineering

Convection-enhanced delivery (CED) is a drug delivery method characterized by direct infusion into target tissues under a positive pressure gradient and shows promise for treating neurological diseases by circumventing the blood-brain barrier to deliver therapeutics directly to the central nervous system parenchyma. With the use of contrast agents, magnetic resonance (MR) imaging provides a means of non-invasively monitoring distribution profiles of agents delivered by CED and provides insight into the influence of anatomy on tracer distributions. To explore CED in a complex tissue structure, the MR contrast agent, Gd-albumin, was infused into the rat dorsal and ventral hippocampus to determine which neuroanatomical features within these structures influenced infusate distribution. MR methodologies were developed to visualize the dynamic and final distributions of the contrast agent *in vivo* at 11.1 T and a semi-automated segmentation routine was developed to calculate Gd-albumin distribution volumes for comparison predicted volumes.

Additionally, an MR-compatible stereotaxic frame and rat brain radiofrequency coil were designed and constructed for use in experiments to characterize the longitudinal ( $r_1$ ) and transverse ( $r_2$ ) relaxivity of Gd-albumin. Dilutions of the contrast agent were

delivered to four regions of the thalamus and relaxation times were measured at 11.1 T. In a separate experiment, large infusions of Gd-albumin were delivered to the rat thalamus to calculate tissue porosity. The tissue porosity and relaxation times as a function of tissue Gd-albumin concentration were used to calculate  $r_1$  and  $r_2$  which were measured to be 76% and 44% lower, respectively, *in vivo* than in solutions of artificial CSF. The relaxivity values were used to calculate dynamic concentration profiles of Gd-albumin infused into the rat dorsal and ventral hippocampus.

Finally, an MR method for measuring the magnetic susceptibility of objects with a constant cross-sectional profile was developed. This method was applied at 4.7 T and 11.1 T to measure the magnetic susceptibility of solid solution alloys of Cu and Sn demonstrating that the magnetic susceptibility of an alloy can be modulated by altering the volume fraction of component metals. MR-derived values of magnetic susceptibility for Cu-Sn alloys deviated by less than 3% from superconducting quantum interference device magnetometry measurements.

## CHAPTER 1 MOTIVATION AND SPECIFIC AIMS

### 1.1 Motivation

The blood-brain barrier (BBB) consists of a layer of endothelial cells that line blood vessels and are held together by tight junctions. These tight junctions limit the diffusion of large molecules through the endothelial cell layer, effectively isolating the extracellular space (ECS) in the brain from the intravascular compartment. In order for a therapeutic agent to readily cross the BBB it must be small (MW < 500 Da) and lipid soluble or pharmacologically altered to cross the BBB via a receptor-mediated mechanism (Pardridge, 1997). These criteria significantly limit the development of therapeutic agents that can be delivered systemically and transport sufficiently to the brain parenchyma. The BBB has proven to be a substantial obstacle in the treatment of central nervous system (CNS) diseases including brain cancer, Parkinson's disease, Alzheimer's disease, Creutzfeldt-Jakob disease (CJD) and epilepsy (Banks, 2008; Cobb and Surewicz, 2009; Motl et al., 2006; Neuwelt, 2004; Pardridge, 1997). Other factors limiting treatment of CNS diseases include drug metabolism before reaching the desired target region, side effects from exposing healthy components of the CNS to the drug and systemic toxicity. In the case of epilepsy, some potentially anticonvulsant therapeutic compounds, such as inhibitory neuropeptides, are inactive when administered orally and others may cause side effects due to systemic toxicity or interaction with healthy regions of the brain. These limitations have prompted researchers to investigate convection-enhanced delivery (CED) as a method of drug delivery to bypass the BBB and target specific regions of the CNS in a controllable manner (Rogawski, 2009).

In CED, a cannula connected to an infusion pump is placed directly in the target tissue. The infusion pump then supplies a small pressure gradient to cause bulk flow of infusate into the ECS. The target tissue will dilate in response to the pressure field around the cannula, thus reducing resistance and allowing for large distribution volumes (Raghavan et al., 2006). Because the cannula is placed directly into the target tissue, CED bypasses the BBB. CED also reduces systemic toxicity by only exposing the target tissue to the therapeutic agent. CED relies on bulk flow which for macromolecular agents, in contrast to diffusion-driven transport, results in nearly homogenous infusate concentration profiles within the perfused region with a steep drop off at the boundary (Song and Lonser, 2008). Because the infused agent is transported through the extracellular space, small infusion volumes can result in large distribution volumes with this relationship being inversely related to the porosity of the target tissue. CED has been found to be reproducible and clinically safe with minimal damage to cells in the vicinity of the infusion cannula and insignificant increases in interstitial or intracranial pressures (Lonser et al., 2002; Song and Lonser, 2008).

MRI provides a non-invasive means of studying biological structures *in vivo*. MRI possesses advantages over other *in vivo* imaging modalities, such as computed tomography (CT), because the subject is not exposed to ionizing radiation reducing the concern of performing recurrent scans on a single subject. With the use of contrast agents, MRI has been used to assess the efficacy of CED protocols and determine volume distributions of infused agents (Fiandaca et al., 2008; Varenika et al., 2008; Vogelbaum, 2005). Although there are several positive aspects to using MRI to evaluate the therapeutic potential of CED, some challenges still exist. Currently, a contrast agent

can be co-infused with a therapeutic agent in order to quantitatively determine the volume distribution of the infusate *in vivo*. However, concentration profiles of the contrast agent cannot be accurately determined unless the relaxivity of the contrast agent is measured *in vivo*. Calculation of contrast agent concentrations would enable researchers to determine the concentration profiles of drugs co-infused with MR contrast agents and provide another metric to compare computational models of tracer transport to experimental results. Also, real-time imaging of CED in order to observe the dynamics of infusion requires the use of a silica cannula. This is due to the fact that although some metal cannulae are non-magnetic they cause susceptibility artifacts that distort MR images proximal to location of the cannula tip. The development of a susceptibility-matched metal cannula would reduce the image artifact created by the alterations of the local magnetic field around the metal cannula and would also allow the use of a multi-functional metal cannula that could be used as a recording electrode for monitoring brain function or electrophysiological targeting.

## **1.2 Specific Aims**

The objective of this research was to improve the utility of MRI as a tool to investigate CED. This was accomplished by developing a methodology for visualizing contrast agents infused by CED into the rat hippocampus and determining distribution volumes using a developed semi-automatic segmentation routine. Additionally, the relaxivity of Gd-albumin was measured *in vivo* to enable concentration distributions of Gd-albumin, infused during CED, to be calculated and compared to predictive computational models of tracer transport. Finally, work towards developing and characterizing a brain susceptibility-matched metal alloy will be detailed. A susceptibility-matched metal alloy could be fabricated into a cannula that can double as

an electroencephalography (EEG) electrode. This susceptibility-matched metal cannula will reduce distortions in the MR image near the cannula which will yield more accurate placement information and improve accuracy of concentration calculations in the vicinity of the cannula. The advantage of a metal cannula is added electrode functionality which would allow structural targeting based on electrophysiology and EEG recordings to be taken from the infusion site before and after CED.

### **1.2.1 Specific Aim 1: Develop MR Imaging Methodology for Evaluating Contrast Agent Distributions in the Rat Hippocampus *In Vivo* following CED**

Surgical procedures and MR imaging protocols were developed to visualize Gd-albumin distributions, delivered by CED into the rat dorsal and ventral hippocampus, using T<sub>1</sub>-weighted imaging at 11.1 T. Dynamic images were acquired to determine preferential routes of transport in the hippocampus and to determine the origin and timing of backflow. The influence of the complex tissue structure in the hippocampus on Gd-albumin distributions was investigated by inspecting high-resolution MR images of the final distribution and comparing these images to histological sections of infused tissue. Final distribution volumes in the dorsal and ventral hippocampus were calculated using a developed semiautomatic segmentation routine and compared to determine the influence of infusion site on final distribution volumes. The segmentation routine was also applied to dynamic infusion data to determine the relationship between the distributed volume and infused volume of contrast agent in the dorsal and ventral hippocampus. Key features of convective transport within the rat hippocampus are summarized.

### **1.2.2 Specific Aim 2: Measure Gd-Albumin *In Vivo* Relaxivity in the Rat Thalamus at 11.1 T**

Determination of contrast agent concentration distributions after CED into the rat brain requires knowledge of contrast agent relaxivity. Contrast agent relaxivities are dependent on several physiological factors making it important to determine these values *in vivo* to improve the accuracy of concentration calculations. Contrast agent relaxivity is determined by quantifying the linear relationship between change in relaxation times and contrast agent concentration. Therefore, it is important that relaxation time changes are measured in regions of infused tissue with homogenous concentration profiles. In order to meet this requirement, the relaxivity of Gd-albumin was measured in the thalamus of the rat brain *in vivo*. The thalamus is a relatively homogenous structure, deep within the brain allowing for large infusions far from pial surfaces. Several different concentrations of Gd-albumin were infused into the posterior thalamic nucleus (Po) and mesencephalic reticular formation (mRt) and the  $T_1$  and  $T_2$  times of these regions were measured at 11.1 T. A custom rat stereotaxic frame and rat brain quadrature receive-only surface radiofrequency (RF) coil were developed to enable relaxation times to be measured using a volume coil for RF transmission and surface coil for RF reception. The porosity of the infused tissue was estimated in a separate set of experiments by infusing large volumes of contrast agent into the thalamus and measuring the tissue concentration of contrast agent in digested samples of tissue dissected from the fresh rat brain using inductively coupled plasma mass spectroscopy (ICP-MS). Contrast agent relaxivity was determined using a linear relationship between relaxation times and contrast agent concentration. The experimental method developed in this specific aim could be applied to other field

strengths and targeted tissue structures to determine contrast agent relaxivity for specific applications.

### **1.2.3 Specific Aim 3: Design and Test a Susceptibility-Matched Metal Alloy**

Currently, dynamic imaging of CED of contrast agents requires the use of a fused-silica cannula. The silica cannula is non-magnetic and has susceptibility properties that are similar to surrounding tissues which reduces image artifacts. However, fused-silica has poor conductivity which severely limits its use as a recording electrode. A metal cannula, designed to match the magnetic susceptibility of surrounding tissue, would be multifunctional by serving as a cannula and an EEG recording electrode enabling electrophysiological information to be obtained to guide targeting and monitor infused tissue. A binary metal solid solution alloy, composed of diamagnetic copper and paramagnetic tin, was developed as a proof of concept that the susceptibility of an alloy could be tuned by altering the volume fraction of the solute metal. The magnetic susceptibility of the alloy was characterized using previously established methods (i.e. superconducting quantum interference device magnetometry) and magnetic field perturbations around the metal were quantified using an MR method at 4.7 T and 11.1 T. A method was developed for comparing MR field perturbation maps to simulated maps to provide an MR method of estimating the volume susceptibility of a material.

## CHAPTER 2 BACKGROUND AND PREVIOUS STUDIES

### 2.1 The Central Nervous System and the Blood-Brain Barrier

The brain is the complex center of the nervous system made up of neurons, which act as information relays, as well as a supporting cast of cells. The brain can be subdivided into several different regions: white matter (WM), gray matter (GM), extracellular space (ECS), ventricles, cerebrospinal fluid (CSF), and the intravascular compartment.

**Gray Matter.** The GM, so named because of its gray appearance in living tissue, consists of neuronal cell bodies, dendrites, astrocytes, microglia, oligodendrocytes, ependymal cells, and penetrating capillaries. The neuronal cell bodies are the metabolic and genetic centers of the neuron and contain the cellular machinery necessary for protein synthesis. The dendrites are a series of highly-branched outgrowths from the cell body, or soma, which conduct signals from the terminating branches of axons from other neurons. The astrocytes provide structural support to the nervous tissue, supply nutrients to neurons, and maintain appropriate concentrations of ions in the ECS. The branches of the astrocyte cell body radiate in all directions and surround blood vessels contributing to a portion of the BBB (Abbott et al., 2006). The microglia are the macrophages or scavengers of the CNS and play a vital role in the immune system of the CNS.

**White Matter.** The WM is named after its white, pearly appearance due to the abundance of myelinated axons in this region of the brain. Axons are cylindrical tubes of cytoplasm that are supported by a cytoskeleton composed of microtubules and neurofilaments. The microtubules not only play a structural role in the axon but also

serve as a route of anterograde transport for kinesin and retrograde transport for dynein molecules for cellular cargo. In the CNS, myelin is formed by oligodendrocytes and consists of multiple, concentric layers of a lipid-rich membrane that improves the conductivity of axons. A single oligodendrocyte may have multiple branches that serve to myelinate portions of several axons.

**Extracellular Space.** The ECS comprises the narrow spaces that separate one cell membrane from another, accounting for ~20% of the total brain volume (Sykova and Nicholson, 2008). Neurons and other cells that constitute the brain tissue are bathed in interstitial fluid (ISF) that fills the ECS. The ECS also contains the extracellular matrix which is composed of macromolecules that may be tethered to cell membranes or free-floating in the ISF. The extracellular matrix in the brain consists primarily of proteoglycans, tenascins and free-floating hyaluronic acid (Ruoslahti, 1996). The ECS forms a labyrinth in which molecules travel giving the brain tissue the quality of a porous medium (Sykova and Nicholson, 2008). The ISF that fills the ECS is continuous with the CSF at the ventricular surfaces and connected to the CSF through the perivascular spaces. The CSF is a low protein concentration fluid that is generated by the choroid plexus located in the four ventricles of the brain. The CSF functions to cushion the brain in the skull and flows from the choroid plexuses in the lateral ventricles, to the third and fourth ventricles where small additional amounts of fluid are added, and finally to the cisterna magna which is continuous with the subarachnoid space. The subarachnoid space surrounds the entire brain and contains arachnoid villi which are connected to the large venous sinuses which allow the fluid to be absorbed into the venous blood. The perivascular space is a small, fluid-filled space that surrounds blood vessels, to the

arteriole and venule level, as they penetrate the brain tissue from the subarachnoid space. The perivascular space is connected with the ISF and provides a route of flow from the ISF to the CSF giving the brain an effective lymphatic system (Figure 2-1). The standard thought is that transport of molecules in the ECS is diffusion-dominated with potential removal of molecules by transport across the BBB or binding and uptake to cells (Sykova and Nicholson, 2008). Evidence has also suggested that there is bulk flow in the ISF, originating from fluid entering the perivascular space from the blood, along the perivascular spaces at the center of the brain and outward to the subarachnoid space (Abbott, 2004; Groothuis et al., 2007).

**Blood-Brain Barrier.** The BBB is formed by specialized endothelial cells that make up the walls of the blood vasculature throughout the brain as well as astrocytic endfeet that provide a connection to neurons (Abbott et al., 2006; Weiss et al., 2009). These endothelial cells express a unique characteristic in that they contain many intercellular tight junctions which prevent small molecules from diffusing across the gap between cells. This means that most molecules in the blood must take a transcellular route into the brain rather than a paracellular route between cells. Only small, water-soluble agents may cross the BBB through the paracellular aqueous pathway. The transcellular route is modulated by several transport mechanisms. Small, lipid-soluble agents (MW < 500 Da) are able to cross the BBB through the transcellular lipophilic pathway. Other molecules, such as glucose and amino acids, cross the BBB via transport proteins. Receptor-mediated endocytosis is a highly-regulated pathway that allows certain proteins such as insulin to cross the BBB. Adsorptive endocytosis allows native plasma proteins to be transported, although poorly, across the BBB. The purpose

of the BBB is to maintain the proper concentration of ions and other molecules in the ISF that bathes neurons. Neurotoxic levels of neurotransmitters glutamate and glycine are present in the blood but are present at concentrations 1000 times less in the CNS (Neuwelt, 2004). The BBB is also responsible for preventing fluctuations in hormones and nutrients that can occur, for example, after eating a meal (Bernacki et al., 2008).

## **2.2 Convection-Enhanced Delivery**

The BBB is a substantial obstacle to overcome when attempting to deliver therapeutics to the brain. Treating CNS disease with systemically-delivered therapeutics is possible if the therapeutic agents are limited to small (less than 500 Da), lipid-soluble molecules. An option for systemically-delivered agents that do not fall into the above category is to pharmacologically alter the drugs so that they may more readily cross the BBB. Such alterations include modifying to the agent to make it more lipophilic, linking it to a lipid-soluble drug carrier or conjugating it to a natural carrier, such as transferrin, that may cross the BBB through a receptor-mediated transport mechanism (Motl et al., 2006; Pardridge, 1997). Another option is to administer a hyperosmolar agent such as mannitol or labradmil. Hyperosmolar agents cause acute shrinking of the endothelial cells lining brain vasculature which widens the gaps between tight junctions allowing macromolecules to penetrate the brain parenchyma. Although these methods of bypassing the BBB show theoretical promise, they have only been successful for a limited amount of therapeutic agents and can allow undesirable molecules, such as inactive viruses, to enter the brain parenchyma. Issues inherent with systemic delivery include non-localized targeting, reliance on diffusive transport, and potential for systemic toxicity.

The problems with systemic delivery of therapeutic agents targeting the CNS have prompted researchers to develop several methods of localized drug delivery. Intrathecal drug delivery, characterized by direct infusion into the CSF spaces of the CNS, works on the premise that there is no transport barrier between the CSF and CNS parenchyma (Blasberg et al., 1975) and has been used to deliver chemotherapeutic agents to CNS tumors as well as delivering drugs to the CNS for pain management. This method relies on diffusive transport of the drug from the ventricles into the brain parenchyma which limits targeting to tissues close to the CSF spaces. There is also bulk flow between the ventricles and subarachnoid space, the entire CSF volume being produced and cleared within 5 hours, which eliminates any infused drug. Another option for local drug delivery is implantation of biocompatible sustained-release polymers. A drug loaded into these polymers, such as an ethylene vinyl acetate copolymer (EVAc), can diffuse through the polymer matrix and into the surrounding tissue. EVAc is a non-biodegradable polymer, thus the rate of diffusion into tissue is dependent on the loaded macromolecule. Other polymers, such as the polylactic-co-glycolic acid (PLGA) family of polymers, are biodegradable and the release of drug into surrounding tissue is dependent on the diffusivity of the loaded agent and the degradation rate of the polymer. Thus, biodegradable polymers can be tuned to release a drug at a controllable rate. Polymer implantation relies on diffusive transport yielding a concentration profile that drops off exponentially from the implantation site.

CED was pioneered at the NIH as a method of bypassing the BBB and overcoming the limitations of diffusion-driven, local methods of drug administration to the brain parenchyma (Bobo et al., 1994). CED involves the stereotactic placement of a

cannula directly into the target CNS tissue and using a pressure gradient to drive the infusate, by bulk flow, through the ECS of the CNS parenchyma. The term CED originates from the fact that diffusive transport is supplemented by convective flow in the ECS of targeted tissues. During CED, tissue near the cannula tip will dilate in response to the pressure gradient, transiently increasing the tissue porosity and resulting in a concomitant decrease in fluid resistance. This may enable more effective transport through the ECS. Distribution volumes generated by CED can be much larger than those produced by mechanisms of drug delivery that rely on diffusion alone. Additionally, because the infusate is driven by bulk flow, volume distributions of therapeutic agents delivered by CED are generally independent of molecular size (Bobo et al., 1994; Sampson et al., 2011). This property does not hold for macromolecules that are larger than the pore size in CNS tissues (~38-64 nm) (Thorne and Nicholson, 2006) and does not account for other factors that may influence transport such as binding or charge interactions between the infused molecule and native ECM. Aside from large volume distributions, another advantage to delivery by bulk flow is nearly constant concentration profiles for macromolecular agents within an infused region with a steep drop-off in infusate concentration at the boundary (Lieberman et al., 1995) leading to potentially therapeutic doses within the infused region of tissue but limited exposure of surrounding tissue to the infusate. This is in contrast to diffusion-driven mechanisms of delivery where infusate concentrations drop off exponentially from the source (Figure 2-2). In Figure 2-2, the black line indicates an idealized CED concentration profile while the green, red, and blue lines indicate concentration profiles as a result of diffusion from a 0.5 mm diameter spherical source. Finally, drug delivery by CED has been shown to

be reproducible and clinically safe (Bobo et al., 1994; Krauze et al., 2008; Laske et al., 1997; Lonser et al., 1998; Lonser et al., 2002).

Methodological and biological factors play a critical role in the distribution of an infused agent during CED into the CNS. Understanding how these factors influence CED distributions can help guide the development of CED protocols that ensure an effective dose at the target region while limiting systemic toxicity and exposure of healthy regions of CNS to the infused drug. Methodological factors include cannula design, choice of infusion site, infusion rate, duration of infusion and infusate properties. Previous studies aimed to improve cannula design to reduce backflow (Krauze et al., 2005; Yin et al., 2010), and to evaluate the performance of chronically implanted cannulae (Foley et al., 2009), while other studies have focused on the influence of infusion site (Astary et al., 2010; Sampson et al., 2007; Yin et al., 2010) or infusate viscosity (Jagannathan et al., 2008) on infusate distribution. Biological factors include anatomical structure of the infused region, endogenous fluid flow, substrate binding, and efflux of the infusate from tissue (Raghavan et al., 2006). As the infused-region tissue structure becomes more complex, anatomy may have an increasingly greater impact on infusate distributions. One method of anticipating the distribution of infused agents is to view the targeted tissue in terms of hydraulic conductivity. Hydraulic conductivity describes the ease at which fluid can move through the porous spaces in the tissue. In regions of GM, such as the cerebral cortex and thalamus, hydraulic conductivity is relatively isotropic and can be represented by a single value. In the corpus callosum, a WM region, the hydraulic conductivity is anisotropic with preferential flow parallel to the fiber directions. In this region of the brain, hydraulic conductivity is represented as a

tensor. Therefore, CED distributions are expected to be approximately spherical in regions of tissue with uniform porosity and isotropic hydraulic conductivity as no direction of transport is preferred. Conversely, in regions of anisotropic hydraulic conductivity, transport will occur preferentially along directions of high hydraulic conductivity. The perivascular spaces represent an additional region of tissue with a heterogeneous hydraulic conductivity; however, they also have been shown to contribute to CED distribution through the peristaltic action of blood-vessel walls (Hadaczek et al., 2006). This indicates that endogenous fluid flow, which can be heterogeneous, can also influence CED distributions especially in locations that are far from the infusion site. The ventricles, velum interpositum, hippocampal fissure, midbrain cisterns and perivascular spaces are contiguous, fluid-filled spaces that can serve as mass sinks by transporting infusate away from the infusion site towards the subarachnoid space. Binding and metabolism of infused agents as well as efflux from the CNS parenchyma through receptor-mediated mechanisms can also reduce the distribution of infused agents by serving as a mass sink. Thus, biological factors influencing CED represent a complex interplay between preferential transport within heterogeneous tissue structures, supplemental transport due to endogenous fluid flow and reduction of the distributed volume of agent due to the role of mass sinks.

Through clinical trials and animal studies, CED demonstrates potential for treating neurological disease. Direct infusion of interleukin-13 bound to *Pseudomonas* toxin into a pontine glioma showed clinical promise as progression of the aggressive brain-stem tumor was halted for 3-4 weeks after the infusion. CED of glucocerebrosidase into the region of the right facial and abducens nuclei was used to treat a patient with Gaucher

disease and demonstrated observable patient improvement and no signs of toxicity (Song and Lonser, 2008). CED of liposomes containing an MR contrast agent have been delivered to the primate brain to evaluate this method of delivery for the treatment of brain tumors (Krauze et al., 2008) and other investigators have explored the possibility of expanding the use of CED to the treatment of epilepsy (Rogawski, 2009). Recently, CED of topotecan, a drug that is cytotoxic to gliomas, was demonstrated to result in significant tumor regression with minimal patient toxicity indicating it may be a viable therapeutic avenue for treating patients with recurrent malignant gliomas (Bruce et al., 2011). The therapeutic potential of CED may be further enhanced through the development of hardware and methods of administration. Investigators have studied the feasibility of targeting a large region of the CNS with multiple catheters (Thomale et al., 2009) as well as improving cannula design to reduce backflow (Krauze et al., 2005; Yin et al., 2010). Flexible cannula designs and Micro-Electro-Mechanical Systems (MEMS) microfluidic devices have also been developed to improve the feasibility of long-term CED (Foley et al., 2009; Raghavan et al., 2006).

Another major component of CED research is the development of computational models for the prediction of CED distributions. Computational fluid dynamics (CFD) rigid-pore models have been used to predict the distribution of agents infused into the spinal cord (Kim et al., 2009; Sarntinoranont et al., 2003; Sarntinoranont et al., 2006) and brain (Kim et al., 2010). These models neglect deformation during infusion and utilize diffusion-weighted MR images (DWI) of excised and *in vivo* tissues to incorporate realistic anatomical boundaries in the models and capture the heterogeneity of hydraulic conductivity in CNS tissue. Biphasic models, which account for coupled fluid flow and

solid deformation, are under development to predict CED distributions in the CNS when deformation in response to infusion is linearly elastic (Chen and Sarntinoranont, 2007). Simple biphasic models, which model infusion into a spherical tissue volume, have been developed to predict distributions when brain tissue is modeled as a non-linear material (Smith and Garcia, 2009). Models have also been developed to better predict the geometry of the infusion source (i.e. - non-spherical) as a function of flow rate and catheter diameter during CED (Morrison et al., 1999). Additionally, work has been performed to better characterize brain tissue mechanical properties (Lee et al., 2011) which can then be imported into computational models of CED. As computational models evolve by incorporating new CNS tissue mechanical properties and more detailed *in vivo* anatomical information from MRI, they will become more accurate in predicting outcomes of CED protocols. The long-term goal of computational modeling research is the development of patient-specific modeling methods that could be used for surgical planning and optimization of CED protocols. Therefore, MRI will play a critical role in the development of CED as a therapeutic option by providing input into CED models as well as providing an avenue for validating models as they are developed.

## **2.3 Magnetic Resonance Imaging**

### **2.3.1 Overview**

MRI is a powerful diagnostic tool that allows investigators and clinicians to take non-invasive images of biological soft tissues without exposing the subject to radiation. The development of MRI dates back to initial investigations into nuclear magnetic resonance (NMR) by Rabi (Rabi et al., 1938) who was studying nuclear magnetic moments in molecular beams, work which earned a Nobel Prize in physics in 1944. Independent work by Bloch (Bloch et al., 1946), investigating nuclear induction in liquids

using electromagnetic radiation, and Purcell (Purcell et al., 1945), investigating nuclear induction in solids, expanded on the work by Rabi and earned a jointly-awarded Nobel prize in 1952. In 1948, work by Bloembergen, Pound and Purcell (Bloembergen et al., 1948) demonstrated the exchange of energy between nuclei immersed in an external field and their surrounding molecular environment as well as neighboring nuclei and developed a theoretical description of NMR relaxation that is still currently used to explain relaxation behavior in liquids and tissues. As early as 1971, the diagnostic potential of NMR was realized when Damadian (Damadian, 1971) demonstrated the ability to detect tumors by differences in NMR relaxation times. The diagnostic potential of NMR was part of the driving force behind the development of MR imaging. MRI in its current state can be attributed to the pioneering work of Lauterbur (Lauterbur, 1973) in 1973 and Mansfield (Garroway et al., 1974; Mansfield et al., 1976) in 1974 who used magnetic field gradients to localize NMR signals and create proton density images and were recognized for their contribution to the field of medicine by receiving the Nobel prize in Medicine in 2003.

MRI works by taking advantage of the intrinsic quantum mechanical property of spin, specifically non-zero spin, in protons that make up a substance. In biological tissues,  $^1\text{H}$  protons make up the most readily-available source of non-zero spins. When nuclear spins are placed in a strong magnetic field ( $\mathbf{B} = B_0\mathbf{z}$ ), the magnetic dipole moment vector,  $\boldsymbol{\mu}$ , will begin to precess about the field direction and will tend to align along the external static magnetic field. The frequency ( $\omega$ ) at which  $\boldsymbol{\mu}$  precesses around the external magnetic field direction is dependent on the gyromagnetic ratio ( $\gamma$ ) of the proton as well as the strength of the external magnetic field,

$$\omega = B_0 \gamma . \quad (2-1)$$

The ratio of spins that align along the field direction (parallel) to those that do not (anti-parallel) is dependent upon the thermal energy of the substance. Typically, the number of parallel spins is greater than the number the antiparallel spins by only a small amount. Fortunately, because there exists an approximately Avogadro's number of spins in a gram of tissue, a significant MR signal can be detected at room temperature (Haacke et al., 1999). A radiofrequency (RF) coil is used to excite spins and detect the MR signal from a sample. The RF coil excites the tissue by tipping spins originally aligned along the external magnetic field direction (Z) into the transverse (XY) plane. Because this transverse magnetization is in a higher energy state, the spins will tend to realign with the external magnetic field in the absence of the transient magnetic field generated by an RF coil. There are two equilibrium states that are reestablished once the magnetic field generated by the RF coil is removed. The first is realignment of magnetization along the z-axis. This relaxation can be described by an exponential time constant,  $T_1$ , the longitudinal relaxation time. The second is the decay of the transverse (XY) magnetization back to its equilibrium value of zero which is characterized, similarly to the longitudinal relaxation, by an exponential time constant  $T_2$  or the transverse relaxation time (Levitt, 2001). The relaxation from the perturbed state back to realignment with the static magnetic field is different for different tissue types and is a function of the spin's microenvironment as well as the external magnetic field. Imaging sequences can be designed to take advantage of  $T_1$  ( $T_1$ -weighted imaging),  $T_2$  ( $T_2$ -weighted imaging), or relative proton density (proton density-weighted imaging) differences between different tissues to gain image contrast.

The MR signal is generated by the precessing magnetization in the transverse plane. Faraday's law of induction states that, in response to a time variant magnetic flux, a current will be generated in a conductive coil. As a means of energy conservation, the generated current flows in a direction such that it creates a magnetic field in opposition to the time variant magnetic flux. Viewing the transverse magnetization from a reference frame that rotates at the precessional frequency,  $\omega_0$ , and neglecting relaxation, the complex form of the time-dependent signal,

$$s(t) = \int_V \rho(\vec{r}) e^{i\phi(\vec{r},t)} d\vec{r}, \quad (2-2)$$

can be expressed in terms of the spatially varying proton density,

$$\rho(\vec{r}) \equiv \omega_0(\vec{r}) |B_{\perp}(\vec{r})| |M_{\perp}(\vec{r},0)|, \quad (2-3)$$

and phase (Equation 2-4) (Haacke et al., 1999),

$$\phi(\vec{r}, t) = -\gamma \int_0^t \vec{G}(t') \cdot \vec{r} dt' = -2\pi \vec{k} \cdot \vec{r} \quad \text{with} \quad \vec{k} = \frac{\gamma}{2\pi} \int_0^t \vec{G}(t') dt'. \quad (2-4)$$

In Equation 2-4,  $G(t')$  is a magnetic field gradient. The proton density in Equation 2-3 is proportional to the magnitude of the transverse magnetization,  $M_{\perp}$ , the spatially-dependent sensitivity of the RF coil,  $B_{\perp}$ , and the Larmor frequency of precession. Equation 2-3 identifies one source of increased signal-to-noise ratio (SNR) when imaging at higher field strengths. As the precession frequency increases with field strength, according to Equation 2-1, the magnetic flux through the coil varies more rapidly generating a greater signal. The position and time-dependent phase, in a rotating frame of reference, is due solely to the local deviations in the magnetic field generated intentionally by imaging gradients for spatial encoding or unintentionally due

to background gradients (Section 2.4). The expression for the phase can be simplified by introducing the wavevector,  $k$ .

The Nobel prize winning work by Mansfield (Mansfield and Grannell, 1975; Mansfield et al., 1976) took advantage of the fundamental relationship (Equation 2-1) between the gyromagnetic ratio of a nuclei, the strength of the external field and the precessional frequency of the nuclei. Because the precessional frequency of the nuclei is dependent on the strength of the external field, the resonance frequency of nuclei in a sample can be varied spatially by applying a linearly varying magnetic field gradient (it is not a requirement that the magnetic field gradient vary linearly, only that a one-to-one mapping exists between spatial position and frequency). MRI relies on three, orthogonal magnetic field gradients to spatially encode spins throughout a sample,

$$\vec{G} = \frac{\partial B_z}{\partial x} \hat{x} + \frac{\partial B_z}{\partial y} \hat{y} + \frac{\partial B_z}{\partial z} \hat{z}. \quad (2-5)$$

In 2D imaging, a slice-encoding gradient ( $G_s$ ) is applied, in conjunction with a slice-selective RF pulse to excite a slab ( $\Delta z$ ) of spins within a sample (Garraway et al., 1974). The frequency content of the RF pulse has a finite bandwidth (i.e., bandlimited) and ideally only spins within the desired slab will be perturbed with all other spins remaining aligned with the external field. The frequency content of a sample, in the presence of a slice-select gradient, is determined by a combination of the external field and  $G_s$ , which varies linearly along the slice axis,

$$\omega(z) = \gamma B_0 + \gamma G_s z. \quad (2-6)$$

The center of the slab,  $z_c$ , is determined by the excitation frequency of the RF pulse,  $\omega_c$ , as shown in Equation 2-7,

$$\omega_c = \gamma B_0 + \gamma G_s z_c. \quad (2-7)$$

By defining the boundaries of the slab,  $z_1 - z_2 = \Delta z$ , and inserting these positions into Equation 2-7, one can find that the bandwidth of the RF pulse is proportional to  $G_s$  and the slice thickness  $\Delta z$ ,

$$\Delta\omega = \gamma G_s \Delta z. \quad (2-8)$$

Therefore, the position of the desired slice can be controlled by the frequency of excitation of the RF pulse and the thickness of the slab can be controlled by the frequency response, or bandwidth, of the RF pulse exciting spins within the slab defined by

$$z_c - \frac{\Delta z}{2} < z < z_c + \frac{\Delta z}{2}. \quad (2-9)$$

In 3D imaging, a second phase-encoding gradient can be applied in place of the slice encoding gradient to partition the spins along the slice axis. The phase-encoding gradient ( $G_p$ ) is applied for a brief period of time to alter the phase of spins in a sample based on position in the phase-encoding direction (Figure 2-3B). Finally, a read gradient ( $G_r$ ) is applied during acquisition of the free-induction decay signal (FID) to encode the frequency of precession of spins in the read gradient direction (Figure 2-3C). The time-dependent signal in the rotating frame of reference can be found by combining Equation 2-4 and Equation 2-2 for the imaging gradients in the slice ( $G_s$ ), phase ( $G_p$ ) and read ( $G_r$ ) directions,

$$s(k_r, k_p, k_s) = \int \rho(\vec{r}) e^{-i2\pi(k_r r_r + k_p r_p + k_s r_s)} d^3\vec{r}. \quad (2-10)$$

Equation 2-10 is known as the 3D imaging equation and has the form of the Fourier transform of the proton density in the spatial domain to the wavevector, or k-space

domain. The inverse Fourier transform of Equation 2-10 yields an image of the proton density in the spatial domain,

$$\hat{\rho}(\vec{r}) = \mathcal{F}^{-1}(s(k_r, k_p, k_s)). \quad (2-11)$$

Therefore, the time-dependent signal, acquired from a sample, can be spatially encoded by the presence of orthogonal gradients. The signal can then be reconstructed into an image of the proton density by the use of a 3D inverse Fourier transform (3D imaging) or 2D inverse Fourier transform (2D imaging, applied for each slice or slab of spins).

### 2.3.2 Magnetic Susceptibility

In linear materials, magnetic susceptibility ( $\chi_v$ ) describes how the magnetization (M) in a material is linearly related to an applied magnetic field (H) (Haacke et al., 1999),

$$M = \chi_v H. \quad (2-12)$$

The magnetic induction, B, in a material is proportional to the applied magnetic field and the magnetization in the material with the constant of proportionality equal to the permeability of free space,  $\mu_0$ ,

$$B = \mu_0(M + H) = \mu_0(1 + \chi_v)H. \quad (2-13)$$

Therefore, as the applied magnetic field permeates through a substance with spatially varying susceptibility, the local magnetic induction will be altered at the interface between regions with different susceptibilities. MRI measures the precession of nuclei embedded in an external field hence the MR frequency is determined by the magnetic induction within a substance (Equation 2-1). If the magnetic susceptibility distribution within a sample is nearly uniform, the magnetic induction throughout a sample will be homogeneous. Interfaces between regions with large susceptibility differences, such as brain tissue ( $\chi_v = -9.64$  ppm) and the sinuses ( $\chi_v = 0.36$  ppm) (Schenck, 1996),

generate gradients in the local magnetic field that can generate signal loss or distort MR images.

Bone, the sinuses, blood vessels and in-dwelling cannula are a few examples of objects in the body that can cause variations in the local magnetic field. In terms of susceptibility, materials can be classified into four categories: (1) diamagnetic ( $\chi < 0$ ), (2) non-magnetic ( $\chi = 0$ ), (3) paramagnetic ( $\chi > 0$ ) and (4) ferromagnetic ( $\chi \gg 1$ ). During *in vivo* imaging, the susceptibility is usually small ( $|\chi| \ll 1$ ) and ferromagnetic materials must be excluded. Diamagnetic materials tend to generate a weak magnetic field that opposes an applied magnetic field whereas paramagnetic materials generate a weak field that augments the external field. Diamagnetic materials have an induced dipole moment in the presence of an external magnetic field. Atomic currents are created by orbiting electrons and the orbital motion in diamagnetic materials will change slightly such that the atomic current produces a weak magnetic field that opposes the external field. Paramagnetism originates in materials that contain atoms with an unpaired electron. This unpaired electron has an intrinsic magnetic moment that will tend to align with the external magnetic field. The result is the applied magnetic field is slightly weaker around diamagnetic materials and slightly intensified near paramagnetic materials.

Minor susceptibility variation across an object can be advantageously used to gain information about dynamic biological processes or provide an additional source of MR image contrast when the variability does not result in geometric distortions. For instance, the blood-oxygen level dependent (BOLD) contrast generated by the susceptibility difference between paramagnetic deoxy-hemoglobin and diamagnetic oxy-

hemoglobin (Ogawa and Lee, 1990) is used in functional magnetic resonance imaging (fMRI) to localize activation in the brain based on an increase in blood flow due to concomitant increases in oxygen demand in response to neural activity (Belliveau et al., 1991). Additionally, quantitative susceptibility mapping (QSM) of the brain can be used to detect alterations in myelin content (Liu et al., 2011) and shows potential in determining changes in iron metabolism (Schweser et al., 2011). However, large discontinuities in magnetic susceptibility, such as those found at the boundaries between implanted devices and native tissue, result in geometric distortions that can severely impact the diagnostic potential of MRI. For example, complications of arthroplasty procedures are difficult to evaluate with MRI, despite exhibiting excellent soft tissue contrast, due to image distortion arising from metal prosthetic/tissue boundary (Koch et al., 2010). Additionally, increasing interest in determining the relationship between structure and function in brain processes has led to the combination of electrophysiological monitoring and fMRI (Martinez-Santesteban et al., 2007) as well as optogenetics and fMRI (ofMRI) (Lee et al., 2010). Combining these experimental procedures requires implanting cannulae or electrodes necessarily proximal the region of study which may then be obfuscated by susceptibility-induced image artifacts.

The origin of susceptibility-induced object distortion and signal loss in MR images is the frequency shift and intravoxel phase dispersion, respectively, caused by the local magnetic field gradient generated at the interface of regions with large differences in magnetic susceptibility. The presence of large susceptibility variations within a sample introduces a static background magnetic field gradient with a spatial dependence that

can be complex and non-linear. The background magnetic field gradient induces a phase evolution of the excited spin population in addition to the evolution due to the applied linear magnetic field gradients for the purposes of spatially encoding the image.

Recall from Section 2.3.1, that an imaging slice is defined by a frequency-selective RF pulse applied in the presence of a gradient (Equation 2-6). In the presence of a background gradient, the frequency of precession of the spin population ( $\omega$ ) is modulated by the background gradient,  $\Delta B(x,y,z)$ , in addition to the external field ( $B_0$ ) and slice encoding gradient ( $G_s$ ),

$$\omega(z) = \gamma B_0 + \gamma G_s z + \gamma \Delta B(x, y, z). \quad (2-14)$$

The bandlimited RF pulse centered at frequency  $\omega_c$ , intended to excite the slab of spins within the range  $[z_c - \Delta z_0/2, z_c + \Delta z_0/2]$  as shown in Equation 2-9, will now excite spins within a slab defined by

$$z_c - \frac{\Delta z_0}{2} < z + \frac{\Delta B(x, y, z)}{G_s} < z_c + \frac{\Delta z_0}{2}. \quad (2-15)$$

The background gradient results in slice profiles that may have a position-dependent distortion (Koch et al., 2010).

Additionally, the sample is partitioned in the phase-encoded direction by applying a brief, incremented, gradient prior to signal acquisition and partitioned in the frequency-encoded (read) direction by applying a gradient during signal acquisition. The spatial encoding gradients result in a spatially-dependent phase where the phase due to a constant read gradient ( $G_x$ ) is

$$\phi(\vec{r}, t) = -\gamma \int_0^t \vec{G}(t') \cdot \vec{r} dt' = -\gamma G_x r_x (t - TE) = -2\pi k_x x, \quad (2-16)$$

and the spatially dependent phase due to a constant phase gradient ( $G_y$ ) is

$$\phi(\vec{r}, t) = -\gamma \int_0^t \vec{G}(t') \cdot \vec{r} dt' = -\gamma G_y r_y \tau_y = -2\pi k_y y. \quad (2-17)$$

In the above equations, the term  $t - TE$  originates in the use of balanced readout gradients as the first half of the read gradient during the acquisition interval serves to rephase spins modulated by the dephasing read gradient. Therefore, any phase contributed to the spins by the readout gradient occurs during a time  $t$  in the acquisition interval relative to  $TE$ . The term  $\tau_y$  is the duration of the phase encoding gradient. The susceptibility-induced background gradient results in a phase term that is superimposed upon the phase terms generated by the spatial encoding gradients. In spin echo imaging, dephasing of the spins due to the background gradient prior to the  $\pi$  RF pulse is effectively reversed at the echo time. As a result, spin dephasing only develops for time periods relative to the echo time and the susceptibility-induced perturbing phase factor for spin echo imaging becomes

$$\phi'_{SE}(\vec{r}, t) = -\gamma \Delta B(r)(t - TE). \quad (2-18)$$

Conversely, spin dephasing due to the background gradient in gradient echo imaging occurs during the entire interval between the excitation RF pulse and some time,  $t$ , within the acquisition window. The susceptibility-induced perturbing phase factor for gradient echo imaging becomes

$$\phi'_{GE}(\vec{r}, t) = -\gamma \Delta B(r)t = -\gamma \Delta B(r)(t - TE) - \gamma \Delta B(r)TE. \quad (2-19)$$

The rearrangement of Equation 2-19 simplifies the combination of phase terms originating from the spatial encoding and susceptibility-induced gradients. The perturbing phase factor for echo planar images has a similar form to  $\phi'_{GE}$ ; however,  $TE$  is replaced by  $TE_{eff}$  as the effective echo time is dependent on the phase encoding step.

The sequence-dependent perturbing phase factors can be included in the 2D or 3D imaging equations, described in Equation 2-10, by combining the accumulated phase due to the spatial encoding gradients and background gradient and collecting like terms. The 2D imaging equation for spin echo imaging is

$$s_{SE}(k_x, k_y) = \int dx dy \rho(x, y) e^{-i2\pi[k_x(x+\Delta B(x,y)/G_x)+k_y y]}, \quad (2-20)$$

while the 2D imaging equation for gradient echo imaging is

$$s_{GE}(k_x, k_y) = \int dx dy \rho(x, y) e^{-i2\pi[k_x(x+\Delta B(x,y)/G_x)+k_y y]} e^{-i2\pi\gamma\Delta B(x,y)TE}. \quad (2-21)$$

As can be inferred from Equation 2-20 and Equation 2-21, geometric distortion occurs in the read gradient direction as spins that should be appropriated to a particular position,  $x$ , are misappropriated to the position  $x + \Delta B(x,y)/G_x$ . Additionally, no distortion is generated in the phase encoding direction in spin echo or gradient echo images. The lack of a refocusing RF pulse in gradient echo images leads to signal loss due to intravoxel dephasing as indicated by the last term in Equation 2-21. As spins probe the volume within a voxel, they experience the local, susceptibility-induced, magnetic field gradient which results in phase incoherence and signal loss. In echo planar imaging, TE is replaced by  $TE_{eff}$  and the intravoxel phase dispersion is dependent on the phase encoding increment. This can lead to an effective distortion of the object in the phase encoding direction.

The 2D imaging equations which account for susceptibility-induced phase perturbations in a sample can be used to simulate MR images of geometries for which the perturbations of the external magnetic field ( $\Delta B$ ) are known (Bakker et al., 1993; Bakker et al., 1994). Simulations of susceptibility-induced image distortions around an infinitely-long cylinder can be produced easily as there is an analytical solution for  $\Delta B$

(see Figure 2-4). Figure 2-5 demonstrates the distortions generated when imaging a 0.44 cm diameter cylinder ( $\chi_v = -14$  ppm) in water ( $\chi_v = -9.05$  ppm) using spin echo, gradient echo and echo planar imaging protocols at 1.5 T, 3.0 T, 4.7 T, 11.1 T and 17.6 T. Spin echo and gradient echo images were simulated with a 3 × 3 cm FOV, 128 × 128 matrix, 50 kHz BW, phase encoding gradient duration ( $\tau_s$ ) of 544  $\mu$ s and TE of 10 ms. Echo planar images were simulated with a 3 × 3 cm FOV, 64 × 64 matrix, 250 kHz BW, phase encoding gradient duration ( $\tau_s$ ) of 120  $\mu$ s and TE of 20 ms. In all imaging protocols, increasing the imaging field strength results in increased distortion of the object (actual object geometry indicated by green circle). As shown in Equation 2-13, the induced magnetic field is linearly related to the applied magnetic field; therefore,  $\Delta B$  increases with field strength causing more severe object distortions. In spin echo images, the geometric distortion occurs only in the read encode direction with signal pile-up artifacts causing hyperintense signal regions near the edge of the object. In gradient echo images, the geometric distortion is accompanied by a signal loss distortion that results in the object appearing larger in the read and phase encoding directions. In echo planar images, the object is severely distorted in the phase encoding direction because the signal-dephasing term is scaled by the phase encoding step. Figure 2-6 demonstrates the same field strength dependence of image distortions for a tungsten cylinder ( $\chi_v = 50$  ppm) in water.

In all three imaging protocols, the distortion in the read encoding direction is dependent on the ratio of the susceptibility-induced magnetic field gradient and the readout gradient ( $\Delta B/G_x$ ). The amplitude of the readout gradient is protocol dependent and equal to  $BW/(\gamma \cdot FOV)$ , where BW is the imaging bandwidth and FOV is the imaging

field of view. As the readout gradient amplitude increases, the relative contribution of  $\Delta B$  to frequency encoding the spins decreases and distortion is reduced. Additionally, the phase dispersion term in gradient echo and echo planar imaging is scaled by TE. Therefore, signal intensity distortions are linearly dependent on TE. The effect of bandwidth and TE on image distortions in gradient echo and spin echo imaging is demonstrated in Figure 2-7 and Figure 2-8, respectively. In both figures, simulations were performed using the following imaging parameters: 3 × 3 cm FOV, 128 × 128 matrix, and phase encoding gradient duration ( $\tau_s$ ) of 544  $\mu$ s. It is clear from Figures 2-5 to 2-8 that geometric distortions are lowest in spin echo images. Thus, one option for reducing susceptibility-induced image distortions is to avoid using gradient echo or echo planar imaging protocols. The drawback to this approach is that spin echo images may take longer to acquire, reducing imaging efficiency and temporal resolution. Another option for reducing susceptibility artifact in MR images is to shorten TE to minimize the time available for spins to dephase in the presence of the susceptibility-induced magnetic field gradient. Furthermore, at the cost of SNR, the bandwidth of the MR imaging experiment can be increased to reduced geometric distortions in the readout gradient direction. Although adjustments to imaging protocols can reduce sensitivity to susceptibility-induced distortions, in some instances, such as fMRI, high sensitivity to changes in susceptibility is desired.

Aside from optimizing the use of standard MR pulse sequences, techniques such as z-shimming (Du et al., 2007; Tang and Huang), passive shimming (Lee et al.), localized shimming (Hsu and Glover, 2005) and application of specialized RF pulses (Yang et al.) have also been implemented to mitigate susceptibility-induced artifacts.

Recently, novel image acquisition schemes have also been developed for the purpose of minimizing susceptibility artifacts near orthopedic implants (Koch et al., 2010; Koch et al., 2009; Lu et al., 2009). An alternative approach is to design MR hardware and implantable devices such that the amalgamation of component materials results in limited distortion (Kc et al., 2010; Muller-Bierl et al., 2008) or to develop new materials that minimize external field perturbations (Suyalatu et al., 2011). Theoretically, the image distortion around implanted devices could be minimized or even eliminated by matching the magnetic susceptibility of the implant material to the magnetic susceptibility of the implanted tissue. This would be especially useful in applications such as ofMRI where sensitivity to susceptibility changes in tissue is desired and the use of implanted materials is required.

### **2.3.3 Relaxation Theory**

#### **2.3.3.1 Background**

Each atomic nucleus has three important physical properties: mass, electric charge, and spin. The spin of a nucleus indicates that it behaves as if it were spinning around, rotating in space. Spin is not due to some rotation of the nucleus but is an intrinsic property of the nucleus itself – much in the same way that mass or electric charge is an intrinsic property of a nucleus. In quantum mechanics, classical angular momentum (due to a body rotating in space) is quantized to certain allowed values and cannot vary continuously. Similarly, the spin angular momentum of a particle can only take on discrete values that can be given by an integer (bosons) or by a half-integer (fermions). Nuclear spins that are greater than 0 are said to be  $(2I + 1)$ -fold degenerate, where  $I$  is the nuclear spin. That is to say that there exist multiple spin configurations with the same energy. Immersing the spin in an external magnetic field eliminates this

degeneracy through a phenomenon known as the Zeeman effect. Nuclear Zeeman splitting divides the ground state spin levels into sublevels. For example, the  $^1\text{H}$  nucleus has  $I=1/2$  that is divided into two distinct energy levels when immersed in an applied magnetic field.

Based on quantum mechanical theory,  $^1\text{H}$  spins immersed in an external magnetic field will take on one of two possible energy states: one aligned with the external magnetic field (lower energy state) and one aligned opposite to the external magnetic field (higher energy state). The energy difference between these two states is equal to  $2\mu H_0$ , where  $\mu$  is the magnetic moment and  $H_0$  is the applied magnetic field. The ensemble of spins themselves is immersed in a "lattice" which is nothing more than the material or environment in which the ensemble of spins exists. The spin ensemble and the lattice will each have their own temperature,  $T_S$  and  $T_L$  respectively. Because the spin system is able to weakly interact with the lattice, the two temperatures will come to an equilibrium temperature. This temperature is usually the same temperature of the lattice as the heat capacity of the spin system is quite small. The thermal energy at a given equilibrium temperature,  $T$ , is determined by  $E = k_b T$  where  $k_b$  is Boltzmann's constant. Therefore, the ratio of spins populating the lower energy level to the higher energy level is dependent upon the relative importance of the energy associated with magnetic alignment ( $2\mu H_0$ ) and the thermal energy ( $k_b T$ ). The excess of spins in the lower energy state can be described by a Boltzmann factor ( $\exp(2\mu H_0/k_b T)$ ). This results in a small excess of spins in the lower energy state than the higher energy state. Although the excess of spins is small, the total number of spins in the ensemble is quite large, generating a detectable signal in MR.

Due to the slight excess of spins in the lower energy state, the spin system is able to absorb energy from an external source. If an RF field is applied to the spin system, from an RF coil for example, the absorbed energy will serve to raise the spin temperature of the system. When this perturbing RF field is removed, the spin system will once again return to an equilibrium temperature with the lattice. At this point, the small excess of spins in the lower energy state has vanished and the population of spins in both energy states is nearly identical. In order for the spin temperature to cool down and reach the equilibrium with the lattice temperature, there must be a net transfer of nuclei from the higher energy level to the lower energy level. Because the number of spins occupying both energy levels is equal, this means that the probability of transfer from the higher energy level to the lower energy level is greater (Andrew, 1955). The time rate of change of the spin excess in the lower energy state,  $n$ , is proportional to the mean transition probability (average of transition probability from the higher to lower energy state and vice versa),  $W$ , and the difference between the equilibrium lower energy state spin excess (when  $T_S = T_L$ ),  $n_o$ , and the current lower energy state spin excess,

$$\frac{dn}{dt} = 2W(n_o - n). \quad (2-22)$$

The solution to Equation 2-22 yields the time-dependent behavior of the spin excess as it approaches equilibrium after some perturbation, such as raising the spin temperature with a radiofrequency coil, which generates an initial value of spin excess,  $n_a$  given by

$$n_o - n = (n_o - n_a)e^{-2Wt}. \quad (2-23)$$

The time constant with which the spin excess approaches equilibrium is thus  $2W$ . The inverse of this relaxation rate is  $T_1$  or the spin-lattice relaxation time as this is the time it

takes for the spins to come to thermal equilibrium with the surrounding lattice. Thus,  $T_1$  can be determined theoretically with some knowledge of the mean transition probability,  $W$ . MR physicists have used quantum mechanics to make estimations about  $W$  and predict  $T_1$  behavior.

When an ensemble of spins, immersed in a static magnetic field ( $B_0$ ), is exposed to an RF field (perpendicular to the direction of  $B_0$ ) at the Larmor frequency, the spin temperature is raised, as the number of spins in the higher energy state increases, and a net magnetization is formed in the transverse plane. When the RF field is removed, the spin temperature will decrease and approach an equilibrium temperature with the lattice ( $T_1$  relaxation). An additional equilibrium state is recovered when the transverse magnetization vanishes. The time-rate constant that describes the decay of transverse magnetization is  $1/T_2$ . An effect of the RF field on a spin ensemble is an increase in the coherence of the spin system as the spins precess with the same phase. Although the ensemble of spins is immersed in the same static magnetic field, each individual spin experiences a slightly different local magnetic field ( $H_{loc}$ ) and thus frequency of precession. The variability in  $H_{loc}$  is due to the many sources of magnetic fields surrounding a given spin. Each spin experiences fluctuating local magnetic fields originating from the magnetic moments of spins on the same molecule (intramolecular dipole-dipole interaction) and spins on neighboring molecules (intermolecular dipole-dipole interaction). Additionally, the external field,  $B_0$ , may not be completely homogeneous as objects immersed in the field can cause local perturbations of the magnetic field (Section 2.4, Magnetic Susceptibility). Interaction between spins with

slightly different precessional frequencies results in a loss of phase coherence and contributes to  $T_2$  relaxation.

The various factors that can influence the  $T_1$  and  $T_2$  relaxation time of spins, at a molecular scale, all relate to the presence of local, fluctuating magnetic fields. These fluctuating magnetic fields can induce spins to gain or release a quanta of energy through interaction with the lattice ( $T_1$  relaxation) or to mutually exchange energy with each other ( $T_2$  relaxation). Sources of locally fluctuating magnetic fields include:

- Dipole-Dipole interaction
- Chemical shift anisotropy
- J-coupling
- Spin rotation
- Quadrupolar effects

In the absence of quadrupolar effects (absent in  $^1\text{H}$ ), the dipole-dipole interaction gives the greatest relative contribution to relaxation. The dipole-dipole interaction arises from the tumbling motion of molecules containing aligned spins (Figure 2-9). The field experienced at spin I is a combination of the static magnetic field and the contributions of any neighboring magnetic moments including that which arises from the spin S. As the molecule tumbles the contribution of I to the local field at S changes. The fluctuating magnetic field, experienced at S, may contain many frequency components; however, it is the components of the field that fluctuate at  $\omega_0$  (single quantum transitions, one spin, I or S, changes energy levels) and  $2\omega_0$  (double quantum transitions, both spins are at the same energy level and change energy levels) that are capable of inducing energy exchange with the lattice ( $T_1$  relaxation) or mutual energy exchange ( $T_2$  relaxation). The dipole-dipole interaction depicted in Figure 2-9 demonstrates the effect for spins located on the same molecule (intramolecular dipole-dipole interaction); however, the same

effect can take place for spins on neighboring molecules (intermolecular dipole-dipole interaction). The magnitude of the magnetic field of a magnetic dipole decays with distance,  $r$ , from the dipole by a factor of  $1/r^3$ . Therefore, the magnetic field associated with each spin falls off rapidly with distance so only the nearest neighbors to a spin,  $I$ , have an effect on the local magnetic field it experiences.

### 2.3.3.2 Spectral density function

The frequency content of the local, fluctuating magnetic fields can be described by a spectral density function,

$$J(\omega) = \frac{\tau_c}{1 + \omega^2 \tau_c^2} \quad (2-24)$$

The rotational correlation time,  $\tau_c$ , describes the average time it takes for a molecule to rotate 1 radian therefore molecules that undergo rapid movement have small  $\tau_c$  while molecules that rotate less-rapidly have a large  $\tau_c$ . The spectral density function is derived by taking twice the Fourier transform of the autocorrelation function of a randomly fluctuating field. The autocorrelation function,

$$G(\tau) = \langle B(t)B(t + \tau) \rangle, \quad (2-25)$$

describes how rapidly the field changes with time as its magnitude is dependent on the product of the field at time  $t$  and a time  $t+\tau$ , where  $\tau$  is some interval of time. For short intervals of time,  $\tau$ ,  $B(t)$  and  $B(t+\tau)$  are likely to be similar and the result is equal to  $B^2$ . For longer intervals of time,  $\tau$ ,  $B(t)$  and  $B(t+\tau)$  are more likely to be dissimilar and have opposite sign and will average out over time to be equal to zero. The influence of the spectral density function of the local fluctuating magnetic fields on  $T_1$  and  $T_2$  relaxation becomes apparent when evaluating theoretical models of  $T_1$  and  $T_2$  relaxation. In 1948,

Bloembergen, Purcell and Pound described the contribution of the intramolecular dipole-dipole interaction to the relaxation of pure water as (Bloembergen et al., 1948)

$$\frac{1}{T_1} = \frac{3}{10} b^2 (J(\omega) + 4J(2\omega)) \quad (2-26a)$$

$$\text{and } \frac{1}{T_2} = \frac{3}{20} b^2 (3J(0) + 5J(\omega) + 2J(2\omega)) \quad (2-26b)$$

$$\text{with } b = -\frac{\mu_0 \hbar \gamma^2}{4\pi r^3}. \quad (2-26c)$$

The longitudinal relaxation rate,  $1/T_1$ , is scaled by the spectral density functions associated with single quantum ( $\omega$ ) and double quantum ( $2\omega$ ) transitions. The transverse relaxation rate,  $1/T_2$ , is scaled by the spectral density functions associated with zero, single and double quantum transitions. Evaluating the spectral density functions for water in different environments (different  $\tau_c$ ) can give some clue as to how  $T_1$  and  $T_2$  will change with field strength (Figure 2-10). The estimation of  $T_1$  in Figure 2-10 includes only the intramolecular dipole-dipole interaction term in pure water and neglects other sources of local fluctuating fields and effects due to exchange of water in different environments.

### 2.3.3.3 Relaxation in nervous tissue

Relaxation of protons in nervous tissue is driven by local fluctuating magnetic fields as described in the discussion of relaxation mechanisms of pure water above; however, in tissue, the sources of fluctuating fields increase in complexity and the rotational mobility of  $^1\text{H}$  protons are altered as they experience various microenvironments ( $\tau_c$  is heterogeneous). For example,  $^1\text{H}$  may be found in water that can exist in a “free bulk” state or “ice-like” water that behaves as pure water ( $\tau_c \sim 3.5$  ps),

in a rotationally bound state, water that may be bound to macromolecules but still able to rotate ( $\tau_c \sim .01$  ns), or in a non-rotationally bound state, water that is tightly bound to macromolecules and is unable to rotate ( $\tau_c \sim 10$  ns) (Grösch and Noack, 1976). Protons in these various states, relating to varying amounts of rotational freedom, exhibit different rotational correlation times ( $\tau_c$ ) and thus different spectral density functions and ultimately different relaxation times (Figure 2-10). Protons may also be found in macromolecules, such as hyaluronic acid and chondroitin sulfate proteoglycans which are uniquely predominate in the nervous system extracellular matrix (Zimmermann and Dours-Zimmermann, 2008), which may experience varying local magnetic fields (due to chemical shift anisotropies and j-coupling) and degrees of mobility. Additionally,  $^1\text{H}$  may be constantly exchanging between states experiencing various microenvironments within the tissue (e.g. bound to free water, hindered water, macromolecules, etc.). If this exchange process is fast, in comparison to the relaxation rate each environment, the observed relaxation rates ( $1/T_{i,\text{obs}}$  where  $i = 1,2$ ) may be viewed as a weighted-average of proton relaxation in each state ( $1/T_{i,j}$  where  $i=1,2$ ,  $j=1,2..n$  states) (Fung, 1977; Grösch and Noack, 1976; Zimmerman and Brittin, 1957) where the weights are determined by the probability that  $^1\text{H}$  is in a particular state. The observed relaxation rates in a fast exchange regime are given by

$$\frac{1}{T_{i,\text{obs}}} = \sum_j \frac{P_j}{T_{i,j}} . \quad (2-27)$$

Alternatively, if the exchange process is in an intermediate or slow regime, the effects of cross-relaxation, where energy is exchanged between  $^1\text{H}$  in different states (e.g. protons in water bound to glycosaminoglycans of the extracellular matrix and protons in

neighboring free water), may have a significant impact on relaxation times in tissue (Edzes and Samulski, 1978; McConnell, 1958).

The relaxation behavior of protons in neural tissues is further complicated by water diffusion in the presence of local magnetic field gradients, generated by susceptibility differences between regions of tissue (Section 2.4), that can contribute to  $T_2$  relaxation through spin de-phasing (Cherubini et al., 2009; Denk et al., 2010; Li et al., 2011). MR measurements of the relative susceptibility in the human brain indicate spatial variation in the magnetic susceptibility on the order of 0.1 ppm (Schweser et al., 2010), a difference in WM and GM susceptibility and WM susceptibility orientation dependence (Li et al., 2011). Susceptibility weighted imaging of shiverer mice, with a mutation that results in oligodendrocyte dysfunction and associated lack of myelinated axons, demonstrates a reduction in WM and GM susceptibility contrast indicating lipid-rich myelin contributes to susceptibility differences in the brain (Liu et al., 2011). Diamagnetic oxy-hemoglobin, paramagnetic deoxy-hemoglobin (Higashi et al., 1997), iron transport (transferrin) and storage (ferritin) molecules (Wang and Pantopoulos), and various other biological molecules can contribute to susceptibility variation within an imaging voxel that can contribute to  $T_2$  relaxation.

Because  $T_1$  and  $T_2$  relaxation times are related to the structural (e.g. various water environments, presence of myelin, etc.) and chemical (e.g. presence of ferritin, deoxy-hemoglobin, etc.) environments of the tissues being imaged they can give important diagnostic information when differences between normal and disease-state relaxation times are understood (Deoni). For example, changes in WM and GM relaxation times have been used to evaluate injury progression in the spinal cord (Mihai

et al., 2008; Narayana et al., 1999a; Weber et al., 2006). Also, relaxation time changes in the parahippocampal gyrus have been observed in the rat prior to the onset of spontaneous seizures (Parekh et al., 2010). Baseline tissue  $T_1$  and  $T_2$  values can also be used for planning the appropriate contrast agent infusate concentration for CED experiments based on knowledge of contrast agent relaxivity (Chen et al., 2008).

Furthermore, the dispersion, or field strength dependence, of NMR relaxation times in tissue is related to the interaction between free water, water hindered through interaction with macromolecules, and macromolecular protons and understanding this frequency dispersion may give insight into the fundamental dynamic processes that contribute to relaxation. The dispersion of NMR relaxation times may also limit gains in SNR when imaging at higher field strengths. As supplemental research to the work presented in this dissertation, the relaxation times in spinal cord WM and GM were measured at 4.7 T and 11.1 T. This work adds to the existing body of data which consists of measurements at 3 T (Narayana et al., 1999b) and 7 T (Franconi et al., 2000; Meyerand et al., 1998). At both 4.7 T and 11.1 T, no significant difference was seen between WM and GM  $T_1$  values; however, a statistically significant difference was observed between WM and GM  $T_2$  values. These trends mimic those observed by Narayana et. al and Franconi et. al. The combined  $T_1$  and  $T_2$  data (at 3.0 T, 4.7 T, 7.0 T and 11.1 T) demonstrate a trend of increasing  $T_1$  with field strength and decreasing  $T_2$  with field strength. A similar trend was noted by de Graaf et. al. (de Graaf et al., 2006) when measuring relaxation in the rat brain at 4.0 T, 9.4 T and 11.7 T. The trend of increasing  $T_1$  with field strength follows field strength dependence of the dipolar relaxation mechanism when the relaxation is dominated by rapid intermolecular

exchange between free molecules (field strength independent) and molecules bound to the tissue substrate (field strength dependent) (Korb and Bryant, 2001). The trend toward decreasing  $T_2$  with increasing field strength cannot be explained by the dipolar relaxation mechanism which suggests  $T_2$  would increase with field strength. Michaeli, et al. (Michaeli et al., 2002) demonstrated that  $T_2$  in the brain is shortened by water translational diffusion in the presence of susceptibility gradients which generate perturbations in the local magnetic field that increase linearly with field strength (Haacke et al., 1999).

## **2.3.4 Contrast Agents**

### **2.3.4.1 Background**

In Section 2.3.3, which discussed background relaxation theory, the fundamental mechanisms of  $T_1$  and  $T_2$  relaxation were identified as fluctuating local magnetic fields that may arise from a number of sources including neighboring magnetic dipole moments. The idea behind imaging with contrast agents is to introduce paramagnetic molecules into a sample to artificially create an additional source of fluctuating fields generating a supplementary avenue of relaxation for surrounding protons. Gadolinium chelated with diethylenetriaminepentaacetic acid (Gd-DTPA) and Gd-DTPA-labeled albumin (Gd-albumin) are two examples of paramagnetic contrast agents that have been used to enhance relaxation of surrounding protons. Unlike radiopharmaceuticals, the signal changes from paramagnetic contrast agents are not observed directly, rather, the effect of the contrast agent on surrounding proton relaxation times is measured. This effect can be expressed as

$$\frac{1}{T_i} = \frac{1}{T_{i0}} + \frac{1}{T_{i,p}} \quad i = 1,2, \quad (2-28)$$

where  $T_i$  represents the observed relaxation time,  $T_{i0}$  is the diamagnetic or solvent relaxation rate and  $T_{i,p}$  is the paramagnetic contribution to the observed relaxation rate (Burtea et al., 2008). As can be inferred in Equation 2-28, the contribution of the paramagnetic species affects observed longitudinal and transverse relaxation times in the same manner. Contrast agents interact with surrounding protons to alter relaxation times by primarily two mechanisms: inner-sphere and outer-sphere relaxation. Inner-sphere relaxation occurs when a water molecule binds with the primary coordination sphere of the paramagnetic molecule and the electron spins of the paramagnetic species interact with the water protons. This mechanism is limited by the number of coordination sites on the paramagnetic species as well as the chemical exchange rate between bound water molecules and the bulk solvent (Laufer, 1987). Outer-sphere relaxation is dominated by the large and fluctuating magnetic field located close to the paramagnetic center. Because this magnetic field drops off exponentially away from the paramagnetic center, outer-sphere relaxation is highly dependent on the relative diffusion between the paramagnetic species and water molecules (Toth et al., 2002). The inner sphere (IS) and outer sphere (OS) relaxation contributions are additive and combine to form the overall relaxation efficiency of the paramagnetic species,

$$\frac{1}{T_{i,p}} = \frac{1}{T_{i,IS}} + \frac{1}{T_{i,OS}} \quad i = 1,2. \quad (2-29)$$

The relaxation efficiency, or relaxivity ( $r_i$ ), describes the overall ability of the contrast agent to enhance the relaxation rates,  $1/T_1$  and  $1/T_2$ , of water protons and is dependent on the many factors that affect inner-sphere and outer-sphere relaxation

including external field strength, microenvironment (pH, temperature, microviscosity), relative translational diffusion and binding of the contrast agent to larger molecules. The inner-sphere relaxation contributions can be described by the Solomon-Bloembergen-Morgan equations (Bloembergen, 1957; Bloembergen and Morgan, 1961; Solomon, 1955) that define the inner-sphere relaxation in terms of dipole-dipole (“through space”) and scalar contact (“through bonds”) mechanisms. The derivation of these equations has been described in detail by Bertini and Luchinat (Bertini and Luchinat, 1996). The form of these equations is similar to those derived by Bloembergen, Pound and Purcell to describe relaxation in pure water (Equation 2-26) in that they include spectral density terms that scale the relaxation rate of water molecules within the first coordination sphere of the paramagnetic complex. The spectral density terms contain contributions from proton and electron Larmor frequencies as well as correlation times that are modulated by the lifetime of coordinated water, reorientation of the hydrogen-paramagnetic ion complex (rotational correlation time) and electronic relaxation rates (Bertini and Luchinat, 1996; Caravan et al., 1999). Thus, factors that alter these spectral density terms, such as field strength (alters proton/electron Larmor frequency, electron relaxation rates), pH (alters residence lifetime of water), and molecular binding (alters rotational correlation time), will alter inner-sphere relaxation. The contribution of outer-sphere relaxation to overall contrast agent relaxivity is more difficult to define as it includes effects protons hydrogen bonding to the paramagnetic complex as well as diffusion in close vicinity to the complex. The outer-sphere relaxation contribution to diffusing molecules has been described in terms of spectral density functions that are a function of frequency and modulated by the rate of diffusion of protons near the

paramagnetic molecule (Freed, 1978; Hwang and Freed, 1975). The change in observed relaxation times due to a paramagnetic contrast agent is linearly proportional to the concentration of the paramagnetic species,

$$\frac{1}{T_i} = \frac{1}{T_{i0}} + r_i C_i \quad i = 1, 2. \quad (2-30)$$

The relaxivity of paramagnetic agents in tissue is most influenced by two factors. The first is the chemical environment of the tissue. Binding of low molecular weight agents, such as Gd-DTPA, to macromolecules can significantly enhance relaxivity due to a reduction of the rotational correlation time of the contrast agent. The rotational correlation time can also be reduced by increases in microviscosity. The local pH of the tissue can alter proton exchange rates that affect the inner-sphere relaxation mechanism. The second factor is compartmentalization of the contrast agent within the tissue. As described in section 2.1, the brain is a complex structure with various compartments including cellular compartments (neurons, astrocytes, oligodendrocytes, microglia), axonal compartments, the ECS, perivascular space, and intravascular compartment. During CED, the contrast agent is infused into the ECS and efficient water exchange must occur between all of these compartments in order for all of the tissue water in a voxel to encounter the paramagnetic agent. If all of the tissue water does not encounter the paramagnetic species, then the effective relaxivity will be reduced. The compartmentalization of different tissue types and the water exchange rates between these compartments can influence the effective relaxivity (Lauffer, 1987).

#### **2.3.4.2 Measurement**

The relaxivity of a particular contrast agent can be calculated, according to Equation 2-30, by measuring the relaxation times of a solute as a function of contrast

agent concentration. A linear fit can then be used to calculate relaxivity. This method has been used to calculate relaxivities of several contrast agents in water, plasma and whole blood at multiple field strengths (Pintaske et al., 2006; Rohrer et al., 2005). Relaxivity of Gd-DTPA has also been investigated in homogenous solutions of varying degrees of macromolecular content (Stanisz and Henkelman, 2000). Agar and skim milk solids were added to solutions of Gd-DTPA to increase the macromolecular content and it was found that  $r_1$  increased with macromolecular content. The increase in relaxivity was probably due to a reduction in rotational correlation time of the Gd-DTPA. Studies of paramagnetic contrast agent relaxivities in tissue have also been conducted with the most challenging aspect of these measurements being related to quantifying the tissue concentration of the paramagnetic species. Measurements of Gd-DTPA relaxivities in cartilage *ex vivo* at 8.5 T revealed no difference between relaxivities measured in saline, plasma and cartilage (Donahue et al., 1994). Cartilage concentrations were determined by inductively couple plasma emission spectroscopy. *In vivo* measurements of Gd-DTPA relaxivity in the rat kidney cortex have been measured at 7 T (Pedersen et al., 2000). The concentration of Gd-DTPA in the rat kidney cortex was controlled by assuming a two-compartment model of Gd-DTPA distribution and determining the steady-state concentration of Gd-DTPA that would need to be maintained in the blood in order to have a constant concentration in the tissue. Gd-DTPA was also coinjected with the radiotracer  $^{99m}\text{Tc}$ -DTPA. Sections from the kidney cortex were frozen in liquid nitrogen and scintillation counting was used to determine  $^{99m}\text{Tc}$ -DTPA concentration. A similar study was also conducted in the kidney cortex of a pig *in vivo* at 1.5 T

(Morkenborg et al., 1998) and  $r_1$  and  $r_2$  in the kidney cortex were found to decrease by a factor of 3.9 and 2.5, respectively, in comparison to values calculated in human plasma.

Gadodiamide (Gd-DTPA-BMA) relaxivity measurements in the rat brain have been performed *in vivo* at 4.7 T (Pickup et al., 2005). In these measurements, a burr hole was drilled into the parietal bone of the skull revealing the dura. A brass rod was chilled in liquid nitrogen and then placed on the dura to disrupt the BBB. Evans blue was then systemically injected so that regions of BBB permeability could be determined during post-mortem analysis. Gd-DTPA-BMA was injected via a tail vein catheter at different doses to multiple rats. After euthanasia, the injured region of the rat brain and a section of normal tissue were removed and digested in nitric acid and Gd content was measured using inductively-coupled plasma mass spectroscopy (ICP-MS). The relaxivity of Gd-DTPA-BMA was shown to be lower in the rat brain than in saline. In fact, the relaxivity in tissue differed significantly from saline/albumin solutions of similar macromolecular content suggesting that macromolecular content was not the only factor in determining *in vivo* relaxivity. A low field (2.4 T) study of *in vivo* Gd-DTPA relaxivity in rat brain tissue has also been conducted (Haar et al., 2010). In this study, Gd-DTPA was delivered by CED, unilaterally, to the caudate putamen in three groups consisting of five rats. Each group of rats received a different concentration of contrast agent. After measuring  $T_1$  with a series of inversion-recovery images, a 2 mm thick section of fresh brain tissue corresponding to the infusion site was collected, weighed, and digested with nitric acid. The tissue concentration of Gd was then measured using ICP-Atomic Emission Spectroscopy (ICP-AES). Relaxivity was determined for each concentration group by fitting Equation 2-30 using two data points (the corresponding concentration

and zero concentration from the ipsilateral caudate putamen). Their measured value of relaxivity at 2.4 T,  $5.35 \text{ mM}^{-1}\text{s}^{-1}$ , is higher than relaxivity values calculated for Gd-DTPA in water at 1.5 T or 3 T (Rohrer et al., 2005). The discrepancy between Gd-DTPA-BMA (decreased relaxivity at 4.7 T) and Gd-DTPA (increased relaxivity at 2.4 T) *in vivo* rat brain relaxivities may be due to several reasons. The relative importance of contrast agent binding, which leads to reduced correlation times and generally increased relaxivity, may be different at 2.4 T and 4.7 T (Caravan et al., 2009). Additionally, the inclusion of BMA in the chelating molecule may affect the ability of Gd-DTPA to bind macromolecules. Studies of Gd-albumin *in vivo* relaxivity have not been reported.

#### 2.3.4.3 Determining contrast agent concentration

Knowledge of contrast agent relaxivity permits concentration calculations when the change in MR signal is known. For enhancement in spin echo images, the contrast agent concentration can be calculated by inserting Equation 2-30 into the expression for signal intensity in a spin echo image, i.e.

$$S(C) = S_0 \cdot [1 - e^{-\text{TR}(1/T_{10} + r_1 C)}] \cdot e^{-\text{TE}(1/T_{20} + r_2 C)}. \quad (2-31)$$

Here  $S(C)$  is the measured signal in the presence of a contrast agent,  $S_0$  is the maximum signal intensity determined by proton density and instrument factors, TR and TE are the recovery time and echo time respectively,  $T_{10}$  and  $T_{20}$  are the relaxation times without contrast agent,  $r_1$  and  $r_2$  are the relaxivities of the contrast agent and C is the concentration of contrast agent. Calculation of C in Equation 2-31 requires  $T_{10}$ ,  $T_{20}$  and  $S_0$  maps for the tissue of interest to be calculated. Taking the ratio of  $S(C)$  to  $S(0)$  (the signal in the absence of a contrast agent) simplifies this expression even further by eliminating the need for  $S_0$  and  $T_{20}$  calculations, such that

$$\frac{S(C)}{S(0)} = \frac{[1 - e^{-TR(1/T_{10} + r_1 C)}] \cdot e^{-TE \cdot r_2 \cdot C}}{1 - e^{-TR/T_{10}}} \quad (2-32)$$

Equation 2-32 can be solved explicitly for C when the transverse relaxation term is approximately equal to unity,

$$C = \frac{1}{r_1} \left[ \frac{1}{TR} \ln \frac{S(0)}{S(0) - S(C) \cdot [1 - e^{-TR/T_{10}}]} - \frac{1}{T_{10}} \right], e^{-TE \cdot r_2 \cdot C} \approx 1. \quad (2-33)$$

Application of this assumption requires some *a priori* knowledge of expected concentrations and this condition is generally more easily met when TE times are kept short. Concentrations of Gd-albumin labeled with Evans blue dye infused into a hydrogel have been calculated using this method after the relaxivity of the contrast agent was measured in water (Chen et al., 2008). It was assumed that the contrast agent  $r_1$  and  $r_2$  would not vary significantly in a hydrogel composed of 99% water (wt/wt). Concentrations calculated by MRI were compared to concentrations calculated using an optical imaging method and revealed a good correspondence between both methods. If the contribution of the transverse relaxation term in Equation 2-32 is found to be significant, a numerical method such as Newton's Method, must be used in order to iteratively solve for C.

Other investigators have implemented methods that avoid the need for contrast agent relaxivity calculation in determining contrast agent concentrations. In the study of Gd-DTPA profiles from a polymer-based implant in the rabbit vitreous, concentration profiles were determined from calibration vials that were included in the field-of-view of images of the rabbit's eye (Kim et al., 2005). The calibration vials were solutions of several concentrations of Gd-DTPA. Signals from these vials were placed into a look-up table that enabled the investigators to determine Gd-DTPA concentration profiles near

the polymer implant. Errors introduced from this method applied to brain tissue are two-fold. First, errors are introduced in the  $T_{10}$  and  $T_{20}$  differences between the solvent used in the Gd-DTPA solutions and the brain tissue. Second, the relaxivity of the contrast agent may be different in solution than in tissue leading to changes in the relative signal enhancement seen in water vs. tissue.

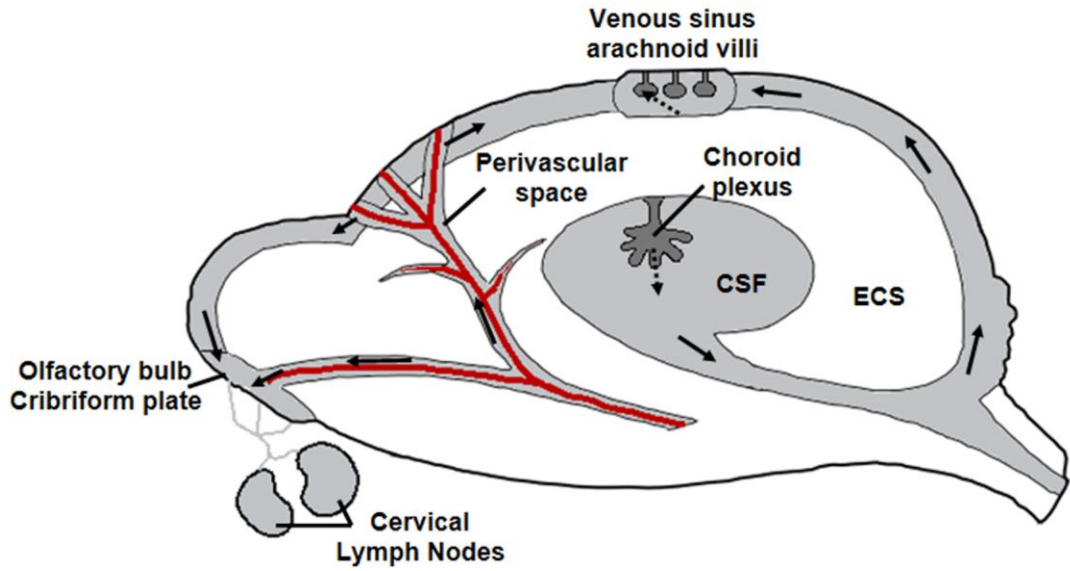


Figure 2-1. Schematic of intrinsic bulk fluid flow in the brain. Fluid is introduced into the brain at the Choroid plexus in the ventricles and by crossing the BBB and entering the perivascular space. It then flows through the ventricles, ECS and perivascular space to be reabsorbed into the venous system at the arachnoid villi. Dashed arrows indicate fluid crossing the BBB.

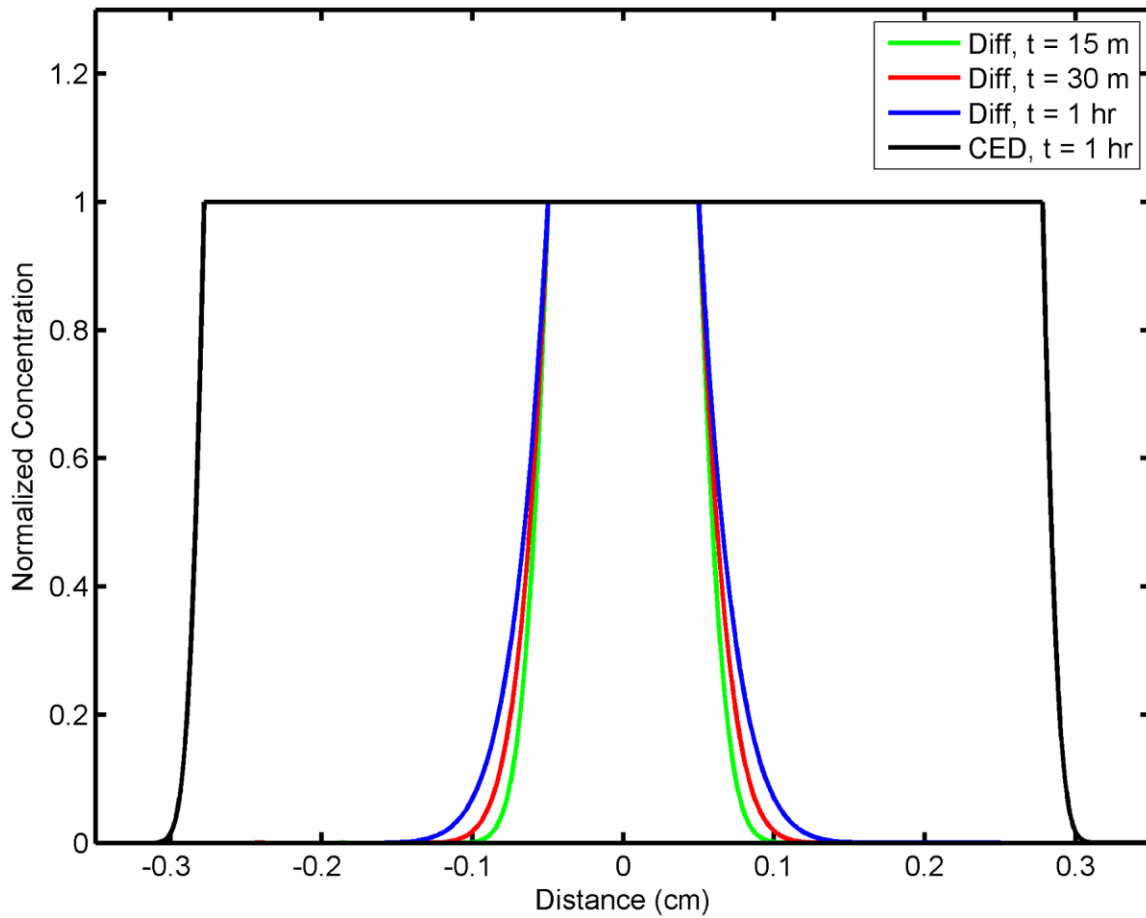


Figure 2-2. Schematic of albumin concentration profiles in brain GM due to diffusion-driven transport and CED. Diffusion profiles were simulated as isotropic diffusion from a 500  $\mu\text{m}$  sphere with  $D_{\text{eff}} = 1.6 \times 10^{-7} \text{ cm}^2/\text{s}$ . CED profiles were approximated for a 1 hour infusion at a rate of 0.3  $\mu\text{L}/\text{min}$  into an isotropic medium with a porosity of 0.2.

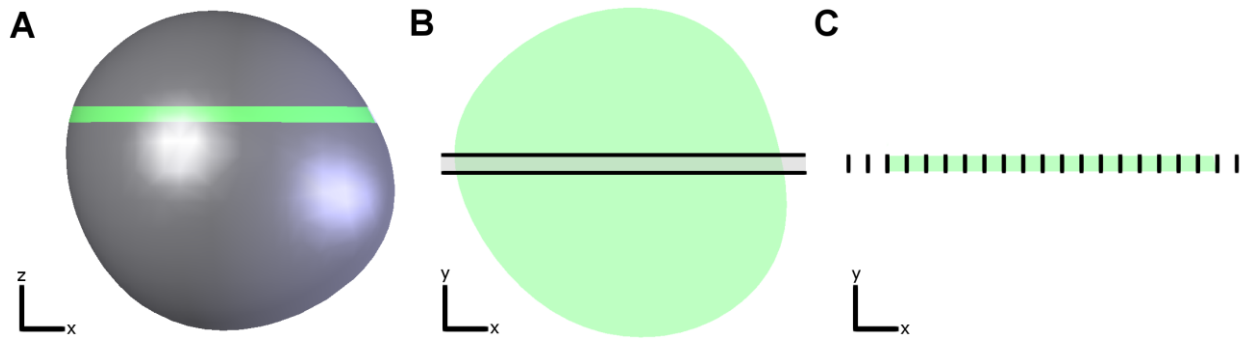


Figure 2-3. Schematic of Fourier imaging. A slice-selective RF pulse is applied in the presence of a linear magnetic gradient to excite a slab of spins in the sample (A). A linearly varying magnetic field is applied in the y-direction for a short time to encode a row of spins (B). Finally, a gradient is applied in the x-direction during signal acquisition to encode the spins along that axis (C).

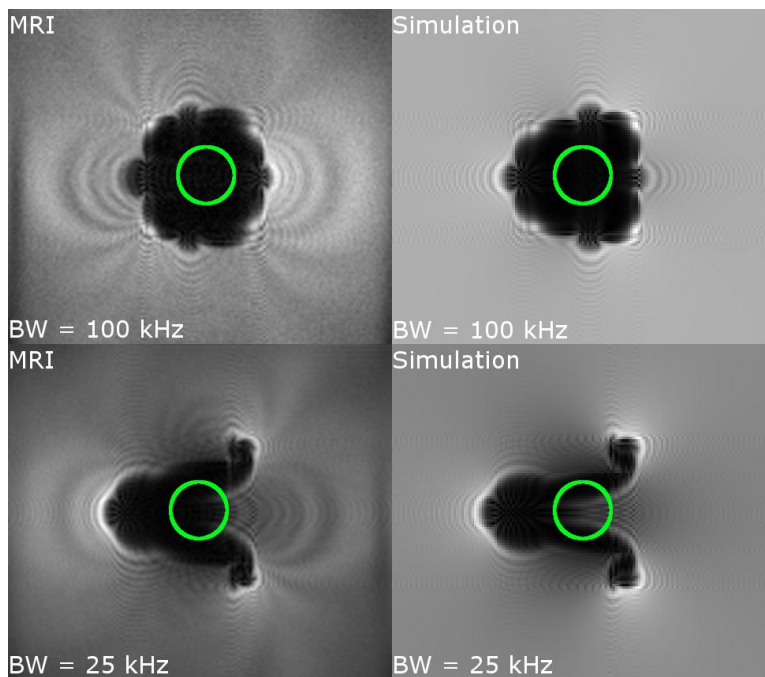


Figure 2-4. A comparison of gradient echo MR images and simulated images of an aluminum cylinder at 11.1 T at two different bandwidths. The green circle indicates the location and outer diameter of the aluminum cylinder.

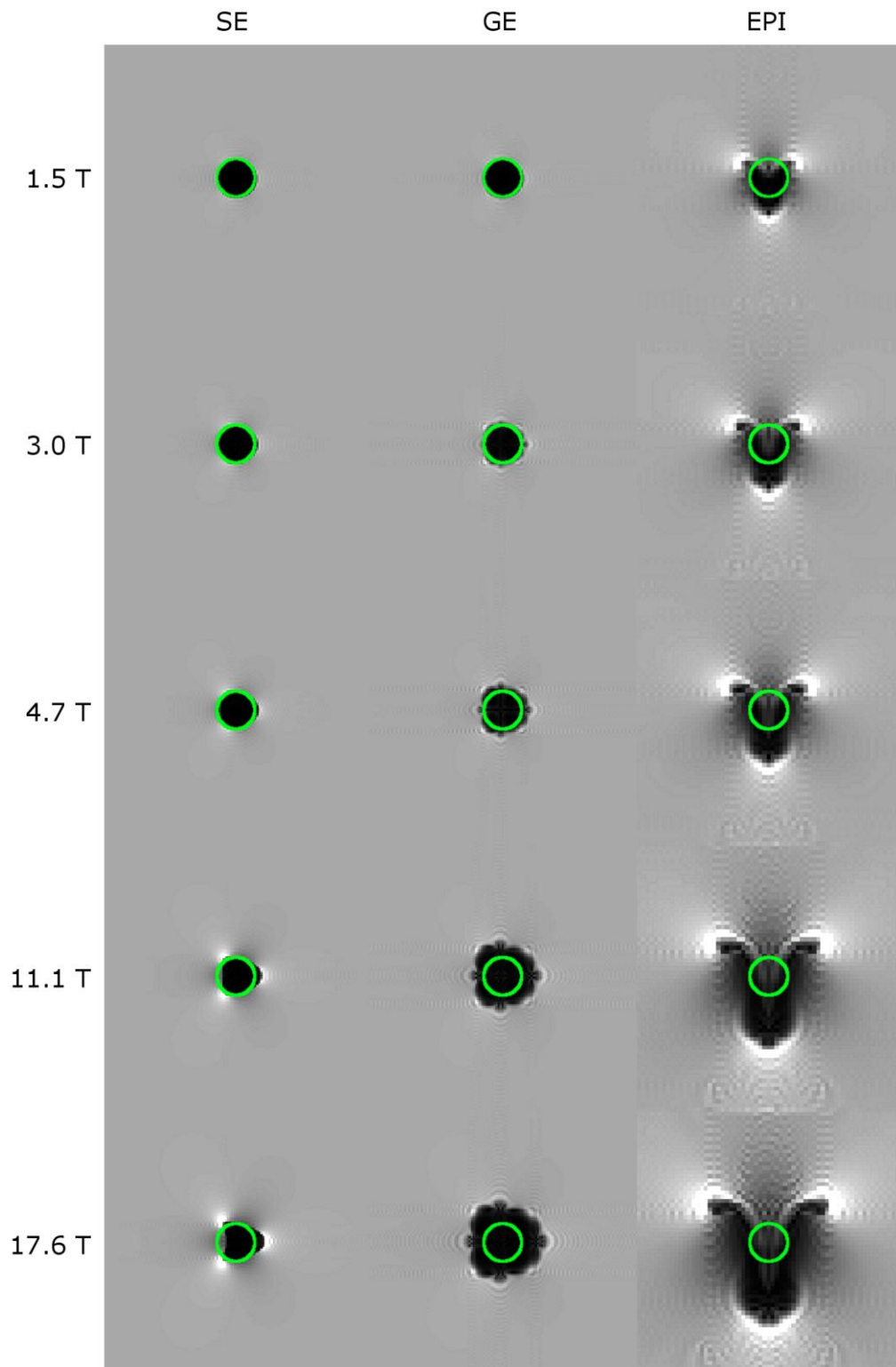


Figure 2-5. Simulations of artifact generated in spin echo (SE), gradient echo (GE), and echo planar (EPI) images by a 0.44 cm diameter cylinder ( $\chi_{v,obj} = -14$  ppm) immersed in water ( $\chi_{v,med} = -9.04$  ppm) at multiple field strengths. The green circle indicates the position and size of the cylinder.

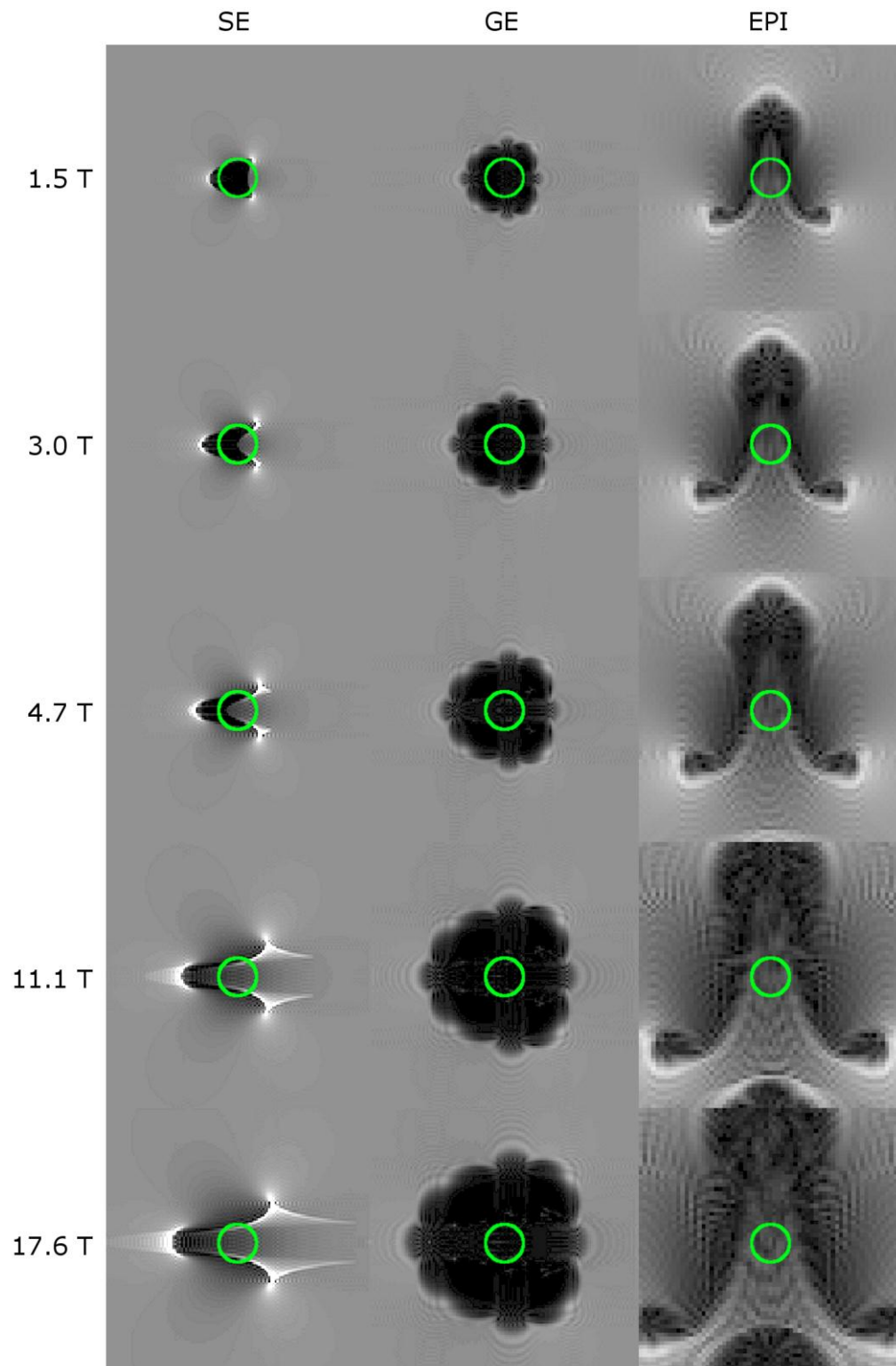


Figure 2-6. Simulations of artifact generated in spin echo (SE), gradient echo (GE), and echo planar (EPI) images by a 0.44 cm diameter tungsten cylinder ( $\chi_{v,obj} = 50$  ppm) immersed in water ( $\chi_{v,med} = -9.04$  ppm) at multiple field strengths. The green circle indicates the position and size of the cylinder.

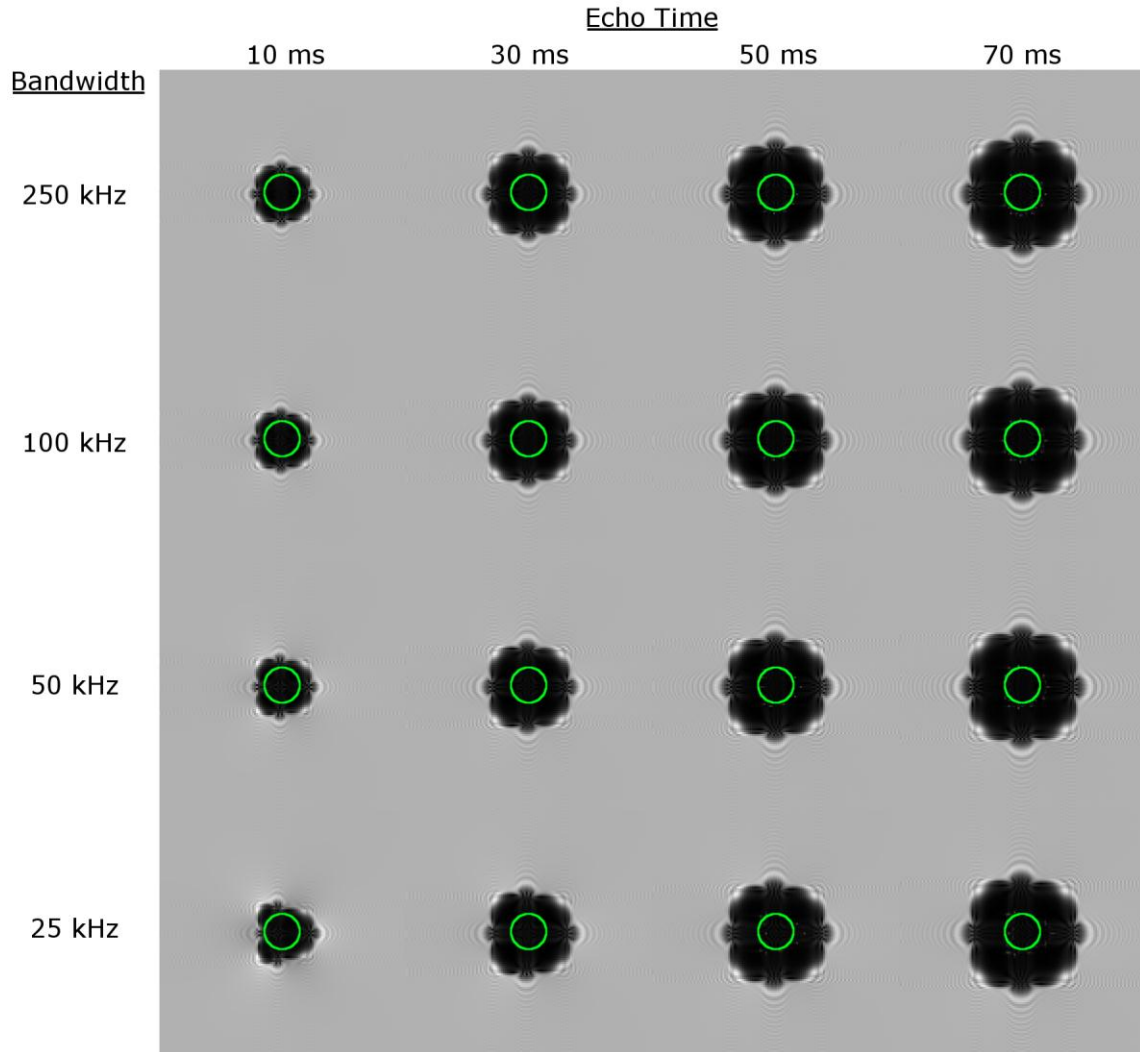


Figure 2-7. Simulations of artifact generated in gradient echo images by a 0.44 cm diameter cylinder ( $\chi_{v,obj} = -14$  ppm) immersed in water ( $\chi_{v,med} = -9.04$  ppm) at 11.1 T as a function of bandwidth and echo time. The green circle indicates the position and size of the cylinder.

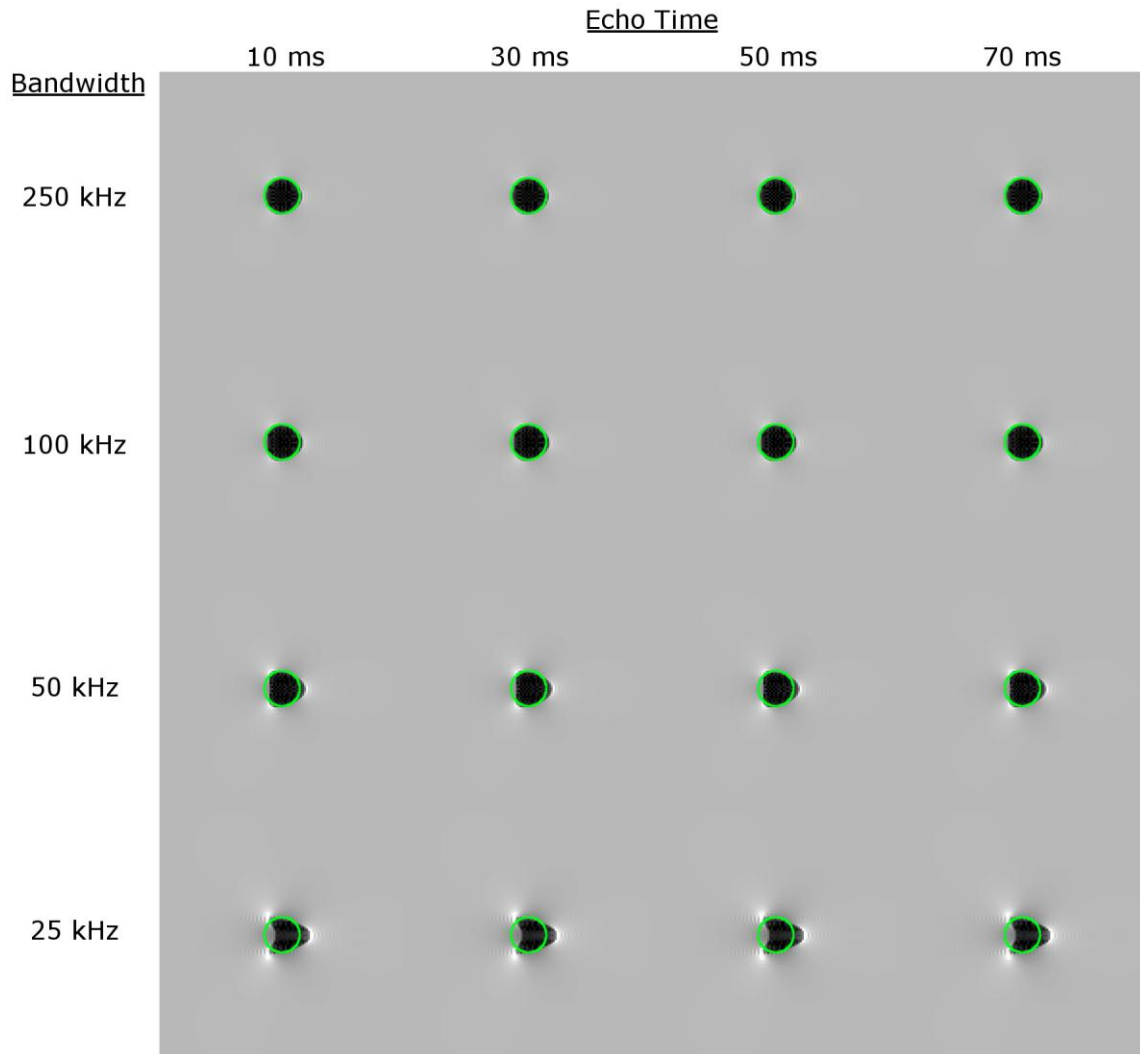


Figure 2-8. Simulations of artifact generated in spin echo images by a 0.44 cm diameter cylinder ( $\chi_{v,obj} = -14$  ppm) immersed in water ( $\chi_{v,med} = -9.04$  ppm) at 11.1 T as a function of bandwidth and echo time. The green circle indicates the position and size of the cylinder.

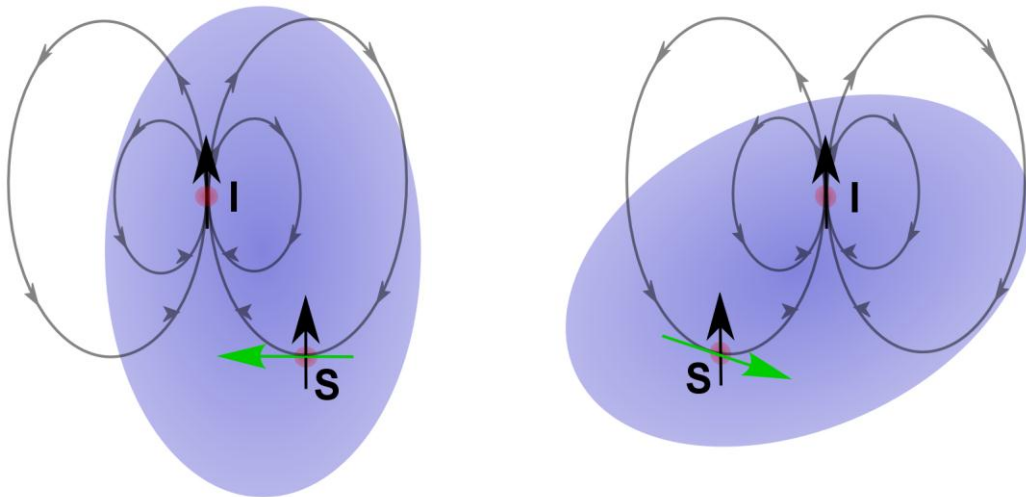


Figure 2-9. Schematic of fluctuating fields due to intramolecular dipole-dipole interaction. Initially, the magnetic dipole moment associated with spin I generates a magnetic field orthogonal to the magnetic dipole moment of spin S. As the molecule tumbles clockwise, the orientations of spin I and S remain unchanged; however, the magnetic field experienced at spin S has changed direction. Continued molecular tumbling would create a dynamic local field at S due to the change in its orientation relative to field generated by the magnetic dipole moment of I.

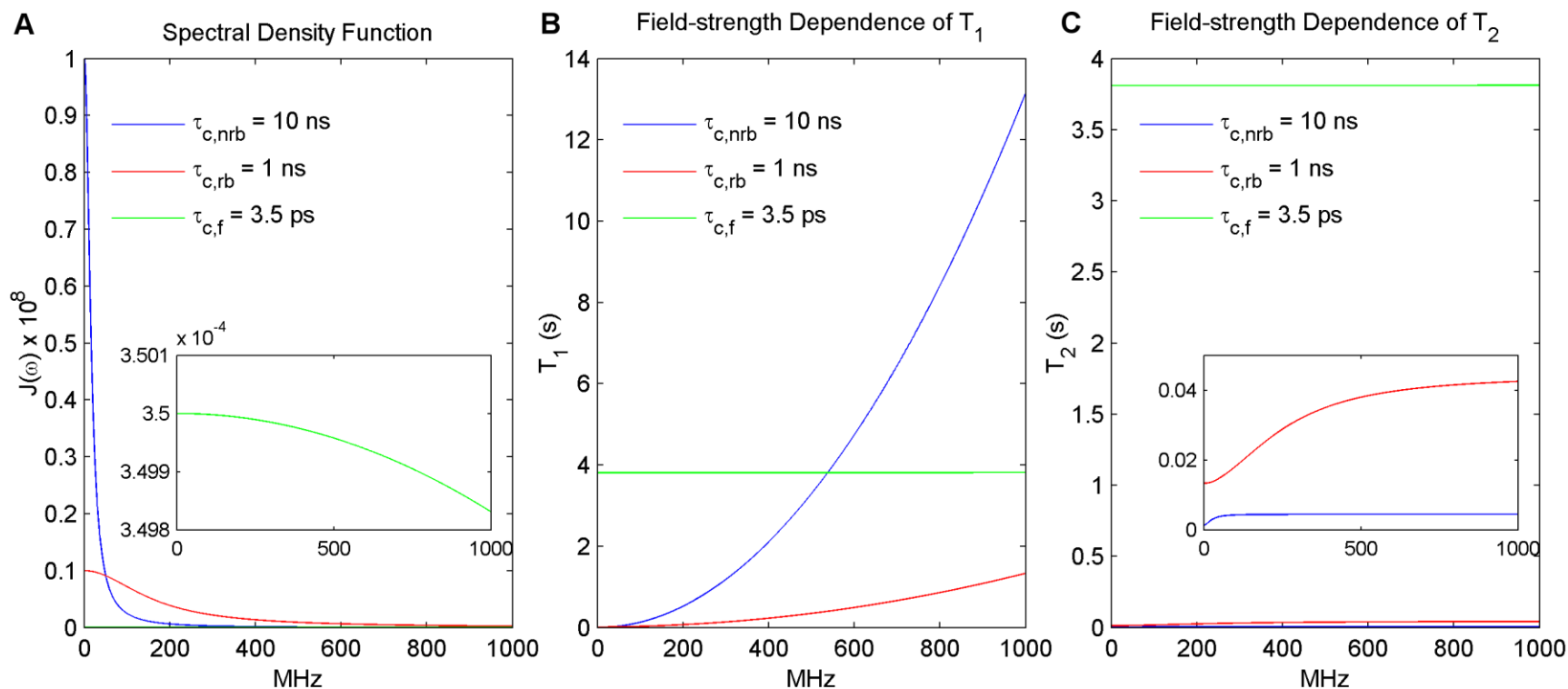


Figure 2-10. Examples of spectral density functions and their effect on  $T_1$  and  $T_2$ . The spectral density functions associated with non-rotationally bound ( $\tau_{c,nrb}$ ), rotationally bound ( $\tau_{c,rb}$ ) and free water ( $\tau_{c,f}$ ) are plotted as a function of frequency up to 1000 MHz (A).  $T_1$  and  $T_2$ , estimated using the BPP theory of dipole-dipole intramolecular relaxation, are plotted as a function of frequency in B and C respectively. The spectral density function of free water changes little with frequency yielding nearly frequency independent relaxation times.  $T_1$  and  $T_2$  relaxation both increase with frequency for non-rotationally bound and rotationally bound water due to the diminishing spectral density function with increasing frequency.

CHAPTER 3  
DEVELOPMENT OF MR IMAGING METHODOLOGY FOR EVALUATING CONTRAST  
AGENT DISTRIBUTIONS IN RAT NERVOUS TISSUE IN VIVO FOLLOWING CED

**3.1 Introduction**

The work outlined in this chapter was devoted to using MRI as a tool to study the anatomical influences of MR contrast agent distributions in two regions of the rat hippocampus, *in vivo*<sup>1</sup>. The hippocampus is a complex structure comprised of both white matter (WM) and gray matter (GM) regions. The GM regions consist of densely packed pyramidal cell bodies in the cornu ammonis (CA) subfields within the hippocampus proper, and the granule cell bodies within the stratum granulosum of the dentate gyrus. Projections to and from these densely packed cell layers constitute the WM regions of the hippocampus. Furthering the complexity, the hippocampus is also a rolled structure, surrounded by pial surfaces and containing penetrating fissures. The fissures and pial boundaries communicate with the extracellular spaces and the ventricular compartments. From a transport perspective, the dense GM regions could serve as isotropic domains resistant to flow whereas WM regions may function as anisotropic domains with lower resistance to flow along directions parallel to fiber projections. The hippocampal fissures and pial boundaries may serve as mass sinks that hinder the penetration of infusate to regions of the hippocampus greater distances from the infusion site. Thus, the combined effect of these anatomical influences could result in a heterogeneous distribution of therapeutic agents within the hippocampus when using CED to treat various disorders. An understanding of the anatomical

---

<sup>1</sup> Parts of this chapter are reprinted from the Journal of Neuroscience Methods, 187/1, Astarly GW, Kantorovich S, Carney PR, Mareci TH, Sarntinoranont M. Regional convection-enhanced delivery of gadolinium-labeled albumin in the rat hippocampus *in vivo*, 129-137, Copyright 2010, with permission from Elsevier

influences on infusate distribution is needed to appropriately plan therapies to maximize treatment in the affected area and limit exposure of healthy brain regions.

This chapter details initial studies which used MRI, along with the contrast agent diethylene triamene pentaacetic acid chelated gadolinium labeled albumin (Gd-albumin) as a surrogate for therapeutic agents, to investigate the effect of anatomical structure on final distribution profiles of an infusate delivered to the rat hippocampus by CED. The final distribution images were valuable in comparing distribution differences between two infusion sites, determining barriers to transport and the overall extent of hippocampal exposure to the contrast agent including an apparent disconnect between the dorsal and ventral regions of the hippocampus. However, from end-point images only inferences can be made as to what factors contribute to determining the final distribution profile of the contrast agent. Dynamic images revealing the temporal evolution of the contrast agent distribution may give more information regarding the influence of tissue architecture on final infusate distribution. For instance, Krauze et al. (Krauze et al., 2008) have used dynamic MR imaging to monitor the ratio of distributed volume ( $V_d$ ) to infused volume ( $V_i$ ) to assess the safety of long-term CED to the primate brainstem and to determine direction of distribution of their contrast agent, Gadoteridol loaded liposomes. Additionally, Mardor et al. (Mardor et al., 2005) have used real-time MR imaging to evaluate the effect of infusate viscosity on infusate distribution by co-infusing with the contrast agent Gd-DTPA. Jagannathan et al. (Jagannathan et al., 2008) have used dynamic MR imaging of CED to investigate leakage of Gd-DTPA and Gd-albumin across pial surfaces of the caudate by monitoring the ratio of  $V_d/V_i$  during infusion into this structure. Dynamic MR imaging of CED in the hippocampus could give

greater insight into the preferential route of tracer transport, the role of the hippocampal fissures and pial boundaries and the cause and timing of backflow along the cannula tract.

Therefore, in addition to initial studies of the final distribution profile of Gd-albumin in the rat hippocampus, extended studies used dynamic contrast-enhanced magnetic resonance imaging (DCE-MRI) to observe the distribution of Gd-albumin, labeled with Evans blue dye, in the rat dorsal and ventral hippocampus during delivery by CED. Large volumes of the tracer were infused into both structures to further investigate the apparent disconnect between the dorsal and ventral hippocampus (Astary et al., 2010). For some subjects, inline pressure was measured throughout the duration of the constant-velocity infusion. Additionally, high-resolution MR images were employed to visualize the final distributions of the contrast agent with finer anatomical detail.

This work was completed through the combined efforts of colleagues in several departments. Svetlana Kantorovich (Neuroscience) performed the surgeries on all animals for the initial studies, conducted histological analysis for initial studies and provided surgical guidance and neuroanatomical expertise for extended studies. Tatiana Nobrega (Biomedical Engineering) designed the experimental apparatus and data collection scheme necessary for inline pressure measurements as well as helped conduct surgeries and prepared animals for MR imaging in extended studies. Jung Hwan Kim (Mechanical and Aerospace Engineering) performed animal surgeries, prepared animals for MR imaging and analyzed data in extended studies. My role, in both initial and extended studies, was to prepare the contrast agent and prime infusions

systems, assist in animal surgeries, perform the MR imaging, develop the data processing routines and analyze the MR data.

## 3.2 Methods

### 3.2.1 Infusion System

Gadolinium-diethylene-triamine pentaacetic acid (Gd-DTPA) labeled human serum albumin (Gd-albumin, MW ~ 86 kDa with ~35 molecules of Gd-DTPA per albumin molecule, R. Brasch Laboratory, University of California, San Francisco, CA) tagged with Evans Blue dye was prepared as a tracer for contrast enhancement in MR imaging. Phosphate buffered saline (PBS) was used to dilute Gd-albumin to a concentration of 10 mg/mL (0.117 mM) for optimal contrast enhancement in MR images. In pilot studies, this concentration was determined to result in contrast enhancement within the hippocampus without significant  $T_2$  shortening resulting in signal loss. Over concerns that the Gd-albumin may be aggregating, high performance liquid chromatography (HPLC) was used to evaluate the macromolecular constituents of the infusate solution. HPLC resulted in a single elutant peak suggesting the Gd-albumin was not aggregating and the covalent bonds attaching the Gd-DTPA molecules to albumin were intact. The infusion system consisted of a 100  $\mu$ L gas-tight syringe (Hamilton<sup>®</sup>, Reno, NV) driven by a syringe pump (Cole-Parmer<sup>®</sup>, Vernon Hills, IL) connected to polyaryletheretherketone (PEEK) tubing (Initial studies: ID = 0.381 mm, OD = 0.794 mm, length ~ 0.5 m; Extended studies: ID = 0.254 mm, OD = 1.588 mm, length ~ 3 m; Upchurch Scientific<sup>®</sup>, Oak Harbor, WA). The PEEK tubing was coupled to a silica cannula (Initial studies: ID = 50  $\mu$ m, OD = 147  $\mu$ m; Extended studies: ID = 40  $\mu$ m, OD = 104  $\mu$ m; Polymicro Technologies<sup>®</sup>, Phoenix, AZ) via a microfluidic connector. During extended studies, a

two-way valve served as a connection between the syringe and a PEEK tubing adapter to prevent undesired infusion during transportation and handling.

For experiments including pressure measurements, an additional three-way connector (Valco<sup>®</sup> Instrument, Houston, TX) was placed between the two-way valve and PEEK tubing to couple a fiber optic pressure sensor (FISO Technologies<sup>®</sup>, Québec, CA) to the infusion system. Fiber optic pressure transducers have an extrinsic optical cavity which interfaces with the optical fiber on one end and a diaphragm on the opposing end. The diaphragm deforms in response to applied pressure in turn changing the cavity length. Prior to infusion, the transducers were zeroed to obtain baseline intracranial pressure values. The transducers operational range was 60-260 kPa (460-1960 mmHg), with a resolution of less than 130 Pa (1 mmHg). Data was acquired using a UMI4 signal conditioner (FISO Technologies<sup>®</sup>, Quebec, CA) at a sampling frequency of 20 Hz. In initial calibration experiments, the cannula tip was placed into a beaker of water at a depth of 4 mm below the surface and inline pressures were measured at constant flow rate to determine the pressure drop across the infusion system from the transducer to the cannula tip under the given infusion parameters. This measured infusion system pressure drop (6.9 kPa or 52 mmHg) was subtracted from all steady state pressure measurements taken in tissue to estimate the infusion pressure at the cannula tip.

### **3.2.2 Animal Preparation**

Experiments were conducted on male Sprague-Dawley rats (Initial studies: n = 7; Extended studies: n = 6) weighing 250-350 g using protocols and procedures approved by the University of Florida Institutional Animal Care and Use Committee. Anesthesia was initiated with xylazine (10 mg/kg, SQ) and isoflurane (4%) in 1 L/min oxygen, then

animals were placed in a stereotaxic Kopf<sup>®</sup> apparatus, and inhalation anesthesia (1.5% in 1.5 L/min oxygen) was delivered via a nose mask. The skull was exposed by a mid-sagittal incision that began between the eyes and extended caudally to the level of the ears to expose bregma and lambdoidal sutures. Burr holes, 3 mm in diameter, were drilled into the skull above the left-side dorsal hippocampus and the right-side ventral hippocampus. For initial studies, the silica cannula was stereotaxically guided to the infusion sites and 5.0  $\mu$ L of Gd-albumin was infused into the dorsal dentate gyrus of the hippocampus (AP = -3.7, ML = -2.2, DV = -3.4) and another 5.0  $\mu$ L into the ventral CA1 subregion of the hippocampus (AP = -5.0, ML = 4.9, DV = 5.0) at a rate of 0.3  $\mu$ L/min. Immediately following the infusion surgery (~30 min), animals were transported to the 11.1 T magnet for MR imaging.

For extended studies, the silica cannula, connected to an infusion system primed with Gd-albumin with Evans Blue dye, was stereotaxically inserted into the brain 0.25 mm deeper than the targeted dorsal dentate gyrus of the hippocampus (AP = -3.7 mm, ML = -2.2 mm, DV = -2.75 mm). After 5-10 minutes, the cannula was retracted 0.25 mm and then secured in place using skull fixture adhesive (Cranioplastic, PlasticsOne<sup>®</sup> Inc., Roanoke, VA, USA). This cannula retraction method was implemented to reduce delayed infusion due to obstruction of the cannula aperture. A second silica cannula was also implanted into the ventral CA1 sub-region of the hippocampus (AP = -5.88 mm, ML = 5.1 mm, DV = 5.2 mm) in the same manner. Immediately following the infusion surgery (~2 hours) animals were transported to the 11.1 T magnet where they were placed in a MR compatible stereotaxic frame to secure the positioning of the head and support placement of the RF coil. Saline (2 mL) was administered to animals to

avoid dehydration and anesthesia was maintained (2% isoflurane in 1 L/min oxygen) throughout MR imaging. Respiration and body temperature were also measured (SAI Inc., Stony Brook, NY) to monitor physiological conditions. After animals were placed within the magnet bore, 8.0  $\mu$ L and 10.0  $\mu$ L of Gd-albumin were infused at a rate of 0.2  $\mu$ L/min into the dorsal and ventral hippocampus, respectively, with infusion lines extending from the bore of the magnet to a safe operational distance for the syringe pumps.

At the end of the experiment, animals under inhalation anesthesia (1.5% in 1.5 L/min oxygen) were given xylazine (10 mg/kg, SQ) and ketamine (80 mg/kg, IP). Upon ensuring deep anesthesia, the chest activity was opened to expose the heart, and a needle connected to an infusion pump was inserted into the left ventricle. 200-300 mL of 0.9% saline solution was circulated by the heart, followed by 200-300 mL of 4% paraformaldehyde solution. The brain was then extracted from the skull following decapitation and stored in 4% paraformaldehyde solution overnight.

### **3.2.3 MR Imaging**

MR experiments were performed using a Bruker<sup>®</sup> Avance imaging console (Bruker<sup>®</sup> NMR Instruments, Billerica, MA) connected to a Magnex Scientific<sup>®</sup> 11.1 T horizontal bore magnet system (Varian, Inc., Magnex Scientific<sup>®</sup> Products, Walnut Creek California). A custom-made 130° arc, 3.5 cm rectangular linear-field surface coil constructed on a 4 cm diameter half-cylinder was used for linear transmission and detection of MR signal.

#### **3.2.3.1 Initial studies**

Two sets of high-resolution T<sub>1</sub>-weighted images, with slices oriented in the coronal and sagittal directions, were acquired using a spin-echo sequence with a 2 cm × 2 cm

field-of-view (FOV) in a matrix of  $160 \times 160$ , recovery time of 1000 ms, echo time of 10 ms and 20 slices. Coronally-oriented and sagittally-oriented data were acquired with 8 averages and 6 averages, respectively.

### **3.2.3.2 Extended studies**

Before infusion, three transverse  $T_1$ -weighted spin echo images were obtained with a  $24 \times 24 \times 10 \text{ mm}^3$  (read  $\times$  phase  $\times$  slice) FOV in a matrix  $104 \times 104$  with 10 slices with read in the lateral-medial direction to determine the baseline signal in the brain tissue. Measurements were performed with a TR = 330 ms, TE of 9.4 ms and NA = 6. During the infusion,  $T_1$ -weighted spin echo images were repeated serially to capture the evolution of the infusate distribution. Each scan was obtained with a total acquisition time of ~ 3.5 min. Following the infusion, high-resolution  $T_1$ -weighted spin echo images (TR = 1000 ms, TE = 15 ms, 30 slices at 0.5 mm thickness, NA = 8,  $24 \times 24 \text{ mm}^2$  FOV with  $200 \times 200$  matrix) were acquired to confirm the final distribution pattern.

### **3.2.4 Image Segmentation**

Dynamic and final distribution volumes ( $V_d$ ) of Gd-albumin were calculated by performing semi-automatic image segmentation on the  $T_1$ -weighted coronal images using routines written in MATLAB<sup>®</sup> (The MathWorks<sup>®</sup> Inc., Natick, MA, USA). Dorsal and ventral hippocampus infusion volumes were segmented separately with the following specific threshold criteria. Voxels were included in the infusion volume if their signal intensity was at least 6 standard deviations of noise higher than the signal intensity in the corresponding region contralateral to the site of infusion (controls regions containing no Gd-albumin). The segmentation output of the MATLAB<sup>®</sup> routine was refined using the ITK-SNAP open-source medical image segmentation tool (Yushkevich et al., 2006). Dynamic and final  $V_d$  in the dorsal and ventral hippocampus were

calculated by counting the number of voxels included in each segmented region and multiplying by the volume of a single voxel.

The projected areas of the segmented Gd-albumin final  $V_d$  were calculated to provide another means of characterizing the distributions by determining the principle planes of transport of the infusate within the dorsal and ventral hippocampus. The projected areas were calculated by collapsing the segmented volume onto the medial-lateral / inferior-superior (ML/IS) plane, the medial-lateral / anterior-posterior (ML/AP) plane and the inferior-superior / anterior-posterior (IS/AP) plane. The area of the collapsed segmented volume within each plane was then calculated and compared using a student's t-test for heteroscedastic variance in R (Ihaka and Gentleman, 1996).

### 3.3 Results

#### 3.3.1 Initial Studies

**Infusion site:** Infusions (n=14) were targeted into the dentate gyrus of the left-side dorsal hippocampus (n=7) and into the right-side CA1 of the ventral hippocampus (n=7). Actual infusion sites were confirmed with MR and histology. Contrast agent infused into the dorsal hippocampus was observed to have only limited penetration into the ipsilateral ventral hippocampus (Figure 3-1A and C). Similarly, contrast agent infused into the ventral hippocampus showed severely limited penetration into the ipsilateral dorsal hippocampus (Figure 3-1B and D) with small amounts observed in the fimbria.

Infusion sites were clearly identifiable in all subjects in the dorsal hippocampus and 6 of the 7 subjects in the ventral hippocampus. In the dorsal hippocampus infusions, 6 of 7 infusion sites were located at the interface between the fissure and CA1 subregion of the hippocampus. One infusion site was located in the polymorphic layer of the dentate gyrus. In 4 of 7 ventral hippocampus infusion subjects, the infusion

site was located at the interface between the hippocampal fissure and CA1 subfield of the hippocampus. In 2 of the subjects, the infusion site was determined to be at the interface between the CA1 subfield and alveus of the hippocampus.

**Gd-albumin distribution in the dorsal hippocampus:** The profile of the contrast agent distribution into the dorsal hippocampus was easily distinguishable from surrounding tissue. Exposed regions displayed a hyperintense signal with respect to surrounding regions in T<sub>1</sub>-weighted images (Figure 3-2). MR images showed that the contrast agent entered the CA1, CA3 and dentate gyrus subfields of the hippocampus in all animals (Figure 3-2) and suggest that contrast agent penetrated poorly into the dense dentate gyrus granule cell layer and CA1 pyramidal cell layer, since these regions remain hypointense with respect to the surrounding subfields and are clearly distinguishable in coronal images (arrowheads in Figure 3-2). The contrast agent was seen to cross the midline of the brain in 3 of the 7 subjects. In two of these subjects, the contrast agent crossed the midline of the brain by entering the corpus callosum and traveling medially to the side of the brain contralateral to the infusion site. In one subject, the contrast agent also entered the dorsal hippocampal commissure and was visible in a small portion of the CA1 subfield of the contralateral hippocampus. Contrast agent penetration into the fimbria subfield of the hippocampus was not seen in any of the subjects suggesting the densely packed cell layer CA1 and CA3 subfields served as a barrier to transport into this region (Figure 3-2).

**Gd-albumin distribution in the ventral hippocampus:** The contrast agent penetrated the CA1 and CA2 subfields of ventral hippocampus in all subjects. In 5 of 7 subjects, contrast agent was seen in the dentate gyrus, CA1, CA2, and CA3 subfields of

the hippocampus (Figure 3-3B, C, E, and F). However in two of the subjects, penetration of the contrast agent into CA1 and CA2 was limited and primarily located in the alveus of the hippocampus (Figure 3-3G and H), most likely due to the lateral location of the infusion site (see above discussion of infusion site). The contrast agent did not appear to enter the granule cell layer and hippocampal fissure, since these regions were hypointense relative to the neighboring dentate gyrus. Contrast agent was also observed at the interface between the corpus callosum and the cortex in these subjects.

**Backflow:** Severe backflow, resulting in a significant amount of contrast agent entering the cortex, was seen in 3 of the 7 dorsal infusions (Figure 3-2C, E, and F). Mild backflow resulted in minor exposure of the cortex to contrast agent in 2 of the 7 subjects (Figure 3-2D and H). In 3 of the 7 subjects, backflow allowed the contrast agent to enter the corpus callosum and travel in both the medial and lateral directions along this white matter fibrous structure (Figure 3-2B, C and F).

Severe backflow in ventral infusions resulted in significant amounts of the contrast agent entering the cortex in 3 of the 7 subjects (Figure 3-3B, C and E). Minor backflow was observed in 3 of the 7 subjects (Figure 3-3D, F and G) and no backflow was seen in 1 subject (Figure 3-3H). In cases of minor backflow, contrast agent did not enter the cortex and remained in the hippocampus, usually penetrating the alveus of the hippocampus.

**Image Segmentation:** The three dimensional contrast agent distributions were visualized with a semi-automated segmentation of the contrast agent enhanced regions (Figure 3-4). Because MR imaging was conducted approximately 30 minutes after CED,

the observed distribution profiles include the effects of CED as well as post-CED diffusion.  $V_d$ , including the effects of CED and diffusion, were calculated from the segmentations for each data set and included back flow volumes. For the dorsal hippocampus infusion, the mean and standard deviation of the calculated  $V_d$  was  $23.4 \pm 1.8 \mu\text{L}$ . For the ventral hippocampus infusion, the mean and standard deviation of the calculated  $V_d$  was  $36.4 \pm 5.1 \mu\text{L}$ . The ventral hippocampus  $V_d$  was greater than the dorsal hippocampus  $V_d$  ( $p \leq 0.0003$ , power of test = 0.99). The contribution of diffusion after the end of CED to the measured  $V_d$  was estimated using an analytical solution of one-dimensional diffusion from a sphere. The radius of the sphere was determined such that the volume of the sphere would be equal to  $V_d$  of the contrast agent in the dorsal and ventral hippocampus. The diffusion coefficient of albumin in rat cortical slices,  $D = 1.63 \times 10^{-7} \text{ cm}^2/\text{s}$  (Tao and Nicholson, 1996), was used in this estimation. Based on these results, it can be estimated that the diffusion after the end of CED may increase  $V_d$  up to 40%. This diffusional spread is equivalent to the contrast agent traveling 2-3 voxels (0.250-0.375 mm) during the time-delay between CED and MR imaging (for comparison, the average anterior-posterior spread of the tracer was measured to be 5.4 mm for dorsal infusions and 4.75 mm for ventral infusions) .

### 3.3.2 Extended Studies

**Infusion site:** The placement of the cannula tip within the dorsal or ventral hippocampus was not consistently observable in DCE-MRI images due to limited in-plane resolution and volume averaging due to slice thickness (1 mm). The location of the cannula tip was, however, identifiable in all high-resolution  $T_1$ -weighted images. The cannula tip was located in the polymorphic layer of the dentate gyrus for half of infusions into the dorsal hippocampus and the molecular layer of the dentate gyrus for

the remaining half of infusions. For ventral hippocampus infusions, the cannula tip was located in the molecular layer of the dentate gyrus in 4 of 6 infusions and the border between the hippocampal fissure and CA1 subfield of the hippocampus in 2 of 6 infusions.

**Pressure measurements:** Inline pressure was measured to determine the cause of backflow observed in initial studies. The results of inline pressure measurements, collected during CED and dynamic T<sub>1</sub>-weighted imaging, are reported for a mild backflow case (Figure 3-5, Case 1) and severe backflow case (Figure 3-5, Case 2). For case 1, infusion was delayed for ~750 seconds until inline pressure reached approximately 22 kPa (165 mmHg). The contrast agent then infused into the dorsal hippocampus (polymorphic and molecular layers of dentate gyrus) with minimal distribution in the corpus callosum. The pressure then remained steady throughout the remainder of the infusion with contrast agent distributing primarily in the dorsal hippocampus. As in case 1, contrast agent infusion was delayed for ~800 seconds in case 2; however, the inline pressure during initial accumulation of contrast agent was significantly higher (33 kPa or 250 mmHg). The immediate result of infusion was contrast agent accumulation in the polymorphic layer of the dentate gyrus (dorsal hippocampus), cortex and surface of the brain with a transient increase in pressure. The pressure then decreased throughout the remainder of infusion with the majority of contrast agent accumulating in the corpus callosum, cortex and surface of the brain. Little change was observed in the distribution profile of contrast agent in the dorsal hippocampus.

**Gd-albumin distribution in the dorsal hippocampus:** As in initial studies, tissue exposed to the contrast agent was easily distinguished from unexposed regions by a hyperintense signal (Figure 3-6). The average delay of infusion, defined by the time between activation of the infusion pump and first observation of contrast agent in DCE-MR images, was approximately 4.5 minutes. This delay can only be approximated because of the limited temporal resolution of the DCE-MRI protocol used in this study (3.5 minutes per scan). For all infusions, underlying tissue structures, as well as backflow affected the contrast agent distribution. The infusate was observed to initially enter at the site of cannula tip, substructures within the hippocampus superior to the tip and the corpus callosum. For example, infusions executed with the cannula tip located in the polymorphic layer of the dentate gyrus (3 of 6 infusions) resulted in initial distributions in the polymorphic and molecular layers of the dentate gyrus, the CA1 subfield of the hippocampus and the corpus callosum. As the infusion continued, the distribution evolved by spreading mediolaterally from the infusion site within these substructures of the hippocampus as well as the corpus callosum. Within the hippocampus, the infusate was bound laterally by the border of the hippocampus with the corpus callosum and fimbria and medially by the border formed by the corpus callosum and contralateral hippocampus. The infusate was also observed to travel in the anterior-posterior direction. For infusions into the dentate suprapyramidal blade (3 of 6 infusions) contrast agent was observed to initially distribute within the molecular layer of the dentate gyrus, the CA1 subfield of the hippocampus and the corpus callosum. The evolution of the contrast agent distribution was the same as infusions into the polymorphic layer of the dentate gyrus; however, the contrast agent showed limited

penetration into the dense granule cell layer and had to travel medially, around the granule cell layer to enter the infrapyramidal blade.

**Gd-albumin distribution in the ventral hippocampus:** For ventral hippocampus infusions, the cannula tip was located in the stratum lacunosum-moleculare of the CA1 for 4 of the 6 infusions. For 2 of the 6 infusions, the infusion site was more lateral with the cannula tip being located in the stratum radiatum of the CA1. The contrast agent traveled primarily in the inferior-superior and anterior-posterior directions. For infusions into the stratum lacunosum-moleculare and the stratum radiatum, the contrast agent traveled within the CA1 subfield of the hippocampus and the molecular layer of the dentate gyrus. The infusate was bound laterally by the pyramidal cell layer of the CA1 and, at early time points, medially by limited penetration into the granular layer of the dentate gyrus (Figure 3-7). Due to backflow, the contrast agent was also able to enter the corpus callosum and in extreme cases the cortex. At later time points of the infusion, the contrast agent was able to enter the polymorphic layer of the dentate gyrus as well as the medial portion of the molecular layer of the dentate gyrus. The contrast agent was also observed to enter extraventricular, CSF-filled regions (e.g. velum interpositum, midbrain cisterns between the hippocampus and midbrain). This occurred at early time points indicating the contrast agent was entering the fissure, a fluid-filled region continuous with the extraventricular regions.

**Image Segmentation:** Similar to initial studies, the final  $V_d$  of the contrast agent in the dorsal and ventral hippocampus was calculated using a semi-automated segmentation routine. The mean and standard deviation of the final  $V_d$  was calculated to be  $39.37 \pm 3.42 \mu\text{L}$  in the dorsal hippocampus (after an  $8 \mu\text{L}$  infusion) and  $45.91 \pm 9.19$

$\mu\text{L}$  in the ventral hippocampus (after a 10  $\mu\text{L}$  infusion). In addition to segmentation of final  $V_d$ , dynamic  $V_d$  were calculated using a similar semi-automated routine. The dynamic  $V_d$  were plotted as a function of infusion volume ( $V_i$ ) and a linear curvefit was performed to determine the ratio of  $V_d$  to  $V_i$ . The mean and standard deviation of  $V_d/V_i$  was determined to be  $5.51 \pm 0.55$  and  $5.30 \pm 0.83$  for dorsal and ventral hippocampus infusions, respectively with an r-squared value of  $>0.98$  for linear fits to both sets of data. Projected areas were calculated for each final  $V_d$  to determine the preferential planes of transport for dorsal and ventral hippocampus infusions. For dorsal hippocampus infusions, projected areas in the ML/AP (avg:  $25.3 \text{ mm}^2$ , sd:  $2.8 \text{ mm}^2$ ) and IS/AP (avg:  $25.6 \text{ mm}^2$ , sd:  $4.3 \text{ mm}^2$ ) planes were both larger (p-value  $< 0.01$ ) than in the ML/IS plane (avg:  $17.2 \text{ mm}^2$ , sd:  $1.8 \text{ mm}^2$ ). No statistically significant difference was seen between projected areas in the ML/AP and ML/AP planes (p-value  $\sim 0.88$ ). For ventral hippocampus infusions, the only significant difference between projected areas were found to be between the ML/IS (mean:  $22.5 \text{ mm}^2$ , sd:  $3.8 \text{ mm}^2$ ) and IS/AP (mean:  $29.7 \text{ mm}^2$ , sd:  $4.9 \text{ mm}^2$ ) planes (p-value = 0.02). No significant difference was found between projected areas in the ML/AP (mean:  $23.7 \text{ mm}^2$ , sd:  $5.2 \text{ mm}^2$ ) and IS/AP planes (p-value = 0.06) or ML/AP and ML/IS planes (p-value = 0.65).

### 3.4 Discussion

*In vivo* CED experiments were performed in the dorsal and ventral hippocampus to explore the effects of tissue structure on distribution profiles. Initial studies used high-resolution MR to evaluate the final, static, distribution of Gd-albumin in these regions of the rat brain. Extended studies were performed to observe the temporal evolution of the contrast agent distribution. The advantages of dynamic infusion data include the ability to 1) visualize transport routes within the hippocampus, 2) assess the role of the

hippocampal fissure and pial boundaries in determining final distribution profiles and 3) discern the timing and impact of backflow. In addition to dynamic imaging data, inline pressure measurements were acquired for selected subjects. The combination of imaging and pressure data provided useful knowledge relating to the cause of backflow and may provide a method of testing new cannula designs in the future.

### **3.4.1 Distribution Profiles**

High-resolution  $T_1$ -weighted imaging provided information about the final distribution of the contrast agent with high anatomical detail. Low spatial resolution, dynamic MR images provided temporal information about the distribution of the contrast agent. The combination of these data results in a more complete picture of how the distribution of infusate in the hippocampus is influenced by various factors. For instance, high-resolution MR images of final distribution profiles revealed the position of the contrast agent relative to the granule cell layer of the dentate gyrus and the hippocampal fissure – anatomical structures within the hippocampus that were too small to resolve with the time-limited, DCE-MRI protocol. It was observed in DCE-MR images, for infusions into both the dorsal and ventral hippocampus, that the distribution of contrast agent was dependent upon tissue structure as well as backflow along the cannula track.

The transport of the contrast agent in preferential directions for a given position along the anterior-posterior axis, mediolaterally for dorsal hippocampus infusions and superoinferiorly for ventral hippocampus infusions, may be explained by the anatomical structure of the hippocampus. The molecular layer of the dentate gyrus, the polymorphic layer of the dentate gyrus and the CA1 subfield of the hippocampus are all bordered by pyramidal cell layers characterized by densely packed cell bodies. Furthermore, this

description of hippocampal tissue architecture in the coronal plane extends in the anterior-posterior direction as the hippocampus forms a banana-shaped structure in three-dimensions. These regions of cell bodies may present a higher resistance to fluid flow (or lower hydraulic conductivity) than regions comprised mainly of neuronal projections. Therefore, the infusate will tend to flow parallel to the borders of pyramidal cell layers, rather than perpendicular or across dense cell layers, resulting in mediolateral transport in the dorsal hippocampus and superoinferior transport in the ventral hippocampus. Although the pyramidal cell layers are resistant to flow, they are not impermeable as contrast agent was observed within the cell layers in light microscopy images of brain sections. Therefore, contrast agent distribution patterns in the hippocampus are dictated, in part, by the configuration of high hydraulic conductivity regions (e.g. layers consisting of predominately neuronal projections) and low hydraulic conductivity regions (e.g. dense pyramidal cell layers).

Mass sinks, that serve to eliminate an infusate from surrounding tissue, are another factor postulated to influence the distribution of contrast agents within the hippocampus. The hippocampal fissure, velum interpositum and midbrain cistern all represent additional regions of high hydraulic conductivity that can function as mass sinks. The hippocampal fissure, a sulcus separating the dentate gyrus from the CA1 field in the hippocampus, traverses the dorsal hippocampus along the medial-lateral axis and the ventral hippocampus along the inferior-superior axis. The velum interpositum and midbrain cistern are fluid filled spaces located at the border between the midbrain and dorsal hippocampus and ventral hippocampus, respectively. Each of these three regions is continuous with the ventricular compartment and could act as

mass sinks to infusate distributing within the hippocampus. DCE-MR images of the contrast agent infusion did not have high enough spatial resolution to distinguish enhancement in surrounding structures (e.g. the CA1 subfield of the hippocampus, molecular layer of dentate gyrus) from enhancement in the hippocampal fissure. High-resolution images of the final distribution show hypointense signal in the region of the hippocampal fissure with respect to surrounding regions of the infused hippocampus indicating a lack of contrast agent uptake in this region. However, histological images show high concentrations of Evans blue dye in this region. The potential cause of this observation will be described later. DCE-MR images were well enough resolved to demonstrate the distribution of contrast agent within the velum interpositum (Figure 3-6) and midbrain cistern (Figure 3-7).

In both dorsal and ventral hippocampus infusions, the contrast agent demonstrated access to fluid-filled spaces that are continuous with the ventricles. Therefore, it is probable that the removal of contrast agent from infused tissue, through the action of mass sinks, impacts the distribution of agents delivered by CED in the hippocampus. This could explain, in part, the apparent disconnect between the dorsal and ventral hippocampus observed in both initial and extended studies despite the large infusion volumes used in the extended studies.

### **3.4.2 Image Segmentation**

In addition to qualitative analysis of MR images, quantitative image segmentation of dynamic and final contrast agent distribution volumes was employed to gain supplementary insight into infusions into the dorsal and ventral hippocampus. A semi-automatic segmentation routine was used in this study that compared signal intensity in infused regions of tissue to contralateral, baseline tissue signal intensities. To avoid

observer bias, the segmentation of contrast agent distribution within the infused structures was conducted by employing the selection of a lower-limit threshold that was set high to assure accurate segmentation. All voxels above the threshold within the infused regions of the brain were included in the segmented volumes. This lower-limit threshold was not based on a percentage of the maximum signal observed in the MR images. The absolute value of the signal in the presence of the contrast agent depends on the contrast agent relaxivity and the baseline  $T_1$  values within that particular tissue (Burtea et al., 2008; Caravan et al., 1999). Thus, establishing a threshold based solely on a percentage of the maximum observed signal is not adequate for the quantitative determination of contrast agent distribution. To establish the threshold value, the average signal was measured in the contralateral, unexposed structure. The threshold value was then set to six times the standard deviation of noise above this average signal. In order to establish a lower-limit threshold using this method, the sensitivity of the MR coil must be homogenous. Asymmetry in the sensitivity of the MR coil may erroneously alter the lower limit threshold by introducing bias in baseline signal value measurements of the contralateral, unexposed structures. In these MR measurements, the average SNR in the dorsal and ventral hippocampus was measured to be  $24.2 \pm 3.7$  and  $23.9 \pm 4.7$ , respectively, so the coil was adequately symmetric. Also when the SNR of an MR measurement is  $\gg 3$ , the probability distribution of the measured signal in the presence of noise makes a transition from a Rician distribution to a modified Gaussian distribution (Andersen, 1996; Koay and Basser, 2006). By setting the lower-limit threshold to 6 times the standard deviation of noise above the average signal observed in contralateral structures, the threshold excludes over 99% of voxels that have a

measured signal greater than the baseline value due to solely a fluctuation in noise. A similar method has been employed to establish a lower signal enhancement limit when calculating the concentration profile of a contrast agent infused into an agarose gel (Chen et al., 2008). Since the segmented volume is sensitive to the thresholding criteria, lowering the criteria would result in larger calculated infusion volumes; however, the difference between the dorsal and ventral hippocampus  $V_d$  observed in initial studies would probably not substantially change.

Segmentation of DCE-MR images indicates that the distributed volume of contrast agent ( $V_d$ ) increases linearly with the infused volume of contrast agent ( $V_i$ ). Furthermore, the slope ( $V_d/V_i$ ) of this curve is, on average, equal in the dorsal and ventral hippocampus. This finding meets expectations as the underlying tissue structure within these two regions is the same although the orientation of subregions (e.g. polymorphic layer of the dentate gyrus) may be different. Although  $V_d/V_i$  is similar for each subject, the initial rise of  $V_d$  occurs at variable  $V_i$  due to the delays in infusion discussed in the analysis of inline pressure measurement results. It would be expected that infusion into a homogenous porous media would result in  $V_d$  that increases linearly with  $V_i$  and a slope,  $V_d/V_i$ , that is equal to the inverse of porosity of the infused media. Calculating porosity from the  $V_d/V_i$  measured in the dorsal and ventral hippocampus yields  $0.18 \pm 0.02$  and  $0.19 \pm 0.03$ , respectively, which agree well with reported measures of rat brain porosity (0.2) (Mazel et al., 1998; Sykova and Nicholson, 2008). It should be noted, however, that porosity estimations from  $V_d/V_i$  data in the hippocampus simplify the complex interplay between factors that influence  $V_d$ . For example, the porosity in the hippocampus is heterogeneous with lower porosity in dense cell regions

(e.g. pyramidal cell layers) than in areas constituted primarily of neuronal projections (e.g. CA1 subfield). Additionally, the pressure field originating at the cannula tip can cause a dilation of tissue altering porosity. Mass sinks, such as the hippocampal fissure, and backflow can also result in smaller increases in  $V_d$  for a given increase in  $V_i$ .

Other studies have also noted a linear relationship between  $V_d$  and  $V_i$  (Jagannathan et al., 2008; Lonser et al., 2002). Interestingly, Jagannathan et al. found  $V_d/V_i$  to decrease in the primate brain caudate when the advancing front of the contrast agent reached ependymal surfaces that border the ventricles. Presumably, the contrast agent was able to cross this boundary and result in a decrease in  $V_d$  with increasing  $V_i$ . Although similar mass sinks exist within the hippocampus,  $V_d/V_i$  remained constant for all time points in this study. This indicates that the contrast agent may enter the mass sinks throughout the entire infusion, in contrast to late time points when reaching a pial surface, contributing to an overall lower  $V_d/V_i$  that is constant through the duration of infusion. The hippocampal fissure and other mass sinks within the hippocampus may therefore be a factor influencing contrast agent distribution throughout the entire infusion.

In addition to dynamic  $V_d$  data, final distribution volumes were also calculated. In initial studies, the same volume of contrast agent (5  $\mu$ L) was infused into both the dorsal and ventral hippocampus. Interestingly, the calculated  $V_d$  in the ventral hippocampus was larger than that in the dorsal hippocampus. There may be several factors influencing the difference in final  $V_d$  in the dorsal and ventral hippocampus. One potential factor is the proximity of the dorsal hippocampus infusions to the hippocampal fissure. Because the hippocampal fissure penetrates a larger portion of the dorsal

hippocampus than the ventral hippocampus, a larger region of the dorsal hippocampus is in proximity to this mass sink. Another potential explanation for the observed difference in distribution volumes is the more compact shape of the dorsal hippocampus. In extended studies, a lower infusion volume was used for dorsal hippocampus infusions than in ventral hippocampus infusions. Therefore, a comparison of final  $V_d$  for dorsal and ventral hippocampus infusions cannot be made. Although the infusion volume for ventral hippocampus infusions in extended studies was twice that of initial studies, the increase in  $V_d$  was only ~28% supporting the idea that mass sinks play a role in the final distribution of the contrast agent.

Projected area calculations were performed on the final  $V_d$  to determine preferential planes of transport for dorsal and ventral hippocampus infusion data. Infusion into an isotropic medium would ideally result in a spherical infusion volume with projected areas that are equal in all planes. Indeed, projected areas calculated for a simulated spherical distribution volume of 40  $\mu\text{L}$  (average dorsal hippocampus infusion volume), with the same resolution as the high-resolution MR imaging in this study, were equal in all planes. Therefore, the projected area calculations give some idea of the anisotropic nature of distributions in the hippocampus. For dorsal hippocampus infusions, projected areas in the ML/AP and IS/AP planes were both significantly larger than in the ML/IS plane. The only significant difference in projected areas for ventral hippocampus infusions occurred between the IS/AP and ML/IS with the projected area in the IS/AP plane being greater. This result agrees with the behavior of the contrast agent noted in the qualitative analysis of dynamic distribution profiles. Namely, the contrast agent travels primarily parallel to borders of dense cell regions (ML and AP

directions for dorsal hippocampus infusions, IS and AP directions for ventral hippocampus infusions).

### **3.4.3 Inline Pressure Measurements**

For select subjects, inline pressure was measured throughout infusion. The pressure data provided a quantitative understanding of infusion in tissue while dynamic MR images provided visual insight into the tissue response throughout infusion (Figure 3-5). For example, for a minimal backflow case, inline pressure increased linearly at the start of infusion and reached an approximately steady state value when Gd-albumin was observed to enter the tissue. However, obstruction of the cannula outlet, due potentially to tissue blockage or blood clotting, delayed infusion and resulted in initially higher infusion pressures that subsided after Gd-albumin was observed to infuse into the tissue. Presumably, the initially high infusion pressures, observed in case 2, served to clear the obstruction at the tip of a cannula. After the obstruction is cleared, a bolus of Gd-albumin is briefly delivered to the tissue at high pressure. The pressure then steadily drops to values lower than those observed in the minimal backflow case at steady state. The transient, high-pressure bolus infusion of Gd-albumin, in the severe backflow case, is able to generate forces substantial enough to overcome stresses sealing the surrounding tissue to the surface of the cannula. The result is a separation of surrounding tissue from the surface of the cannula creating a low-resistance channel for fluid flow. This channel allows a significant amount of contrast agent to track back along the cannula and to distribute in undesired regions such as the corpus callosum, cortex and the surface of the brain.

In both the minimal and severe backflow cases, the infusion of Gd-albumin into the tissue is delayed as the pressure in the infusion system rises. In this study, the infusate

was driven by a constant velocity syringe pump. As the syringe pump is running, nearly incompressible fluid will enter the infusion system causing the pressure to rise as a function of the rate at which fluid enters the system and the compliance of the total system. The pressure will rise until the force at the cannula tip becomes large enough to overcome the frictional forces associated with the obstruction ( $P_o$ ). If this pressure reaches a critical point ( $P_{crit}$ ), the forces will be large enough to separate surrounding tissue from the cannula surface and result in severe backflow. Lowering the compliance of the infusion system, by using infusion lines of stiffer materials or with greater wall thickness, will allow the pressure in the system to reach  $P_o$  more quickly and reduce the volume of the initial bolus infusion. Improvements in cannula design that enhance the seal between the surrounding tissue and the cannula (increase  $P_{crit}$ ) or reduce the probability of obstruction (insure  $P_o < P_{crit}$ ) will decrease the likelihood of severe backflow. Coupled dynamic MR imaging and inline pressure measurements, such as those outlined in this study, could be used to assess the efficacy of new cannula designs at reducing backflow.

#### **3.4.4 Advantages and Limitations of MR Imaging**

MR provides a non-invasive tool, with excellent soft tissue contrast, to monitor CED throughout infusion of a contrast agent using dynamic imaging and as well evaluating final distributions using high-resolution imaging. Other imaging modalities, such as autoradiography (Chen et al., 1999) and histology may provide higher resolution than what is available with MR; however, they can only be utilized to evaluate final distribution profiles and cannot be used *in vivo*. As mentioned previously, the limited resolution of dynamic MR images ( $240 \mu\text{m}^2$  in-plane) did not allow for certain substructures in the hippocampus, such as the granule cell layer of the dentate gyrus or

hippocampal fissure, to be identified. Furthermore, resolution of small tissue structures was further reduced due to volume averaging introduced by the 1 mm slice thickness used in DCE-MR images. The DCE-MR imaging parameters used in this study were designed to achieve adequate resolution of the contrast agent distribution at suitable SNR while maintaining a temporal resolution high enough to capture the evolution of the distribution. The use of high-resolution  $T_1$  weighted imaging ( $120 \mu\text{m}^2$  in-plane,  $500 \mu\text{m}$  slice thickness) of final distribution volumes, which is time-insensitive save for slow diffusion of the large contrast agent, supplements the dynamic imaging data by providing greater anatomical detail of the contrast agent distribution.

Another limitation of MR for evaluating CED, specifically when infusing MR contrast agents, is the potentially ambiguous contrast agent distribution in select regions of infused tissue. Previously it was mentioned that, in some instances, light microscopy images seemingly contradict high-resolution  $T_1$ -weighted MR images by indicating presence of contrast agent (by presence of Evans blue dye) in regions that are hypointense with respect to surrounding, infused tissue. This effect can be explained by the fact that, as discussed in Section 2.3.4, MR contrast agents generate image contrast by reducing the longitudinal ( $T_1$ ) and transverse ( $T_2$ ) relaxation times of surrounding water. If the concentration of contrast agent is too low,  $T_1$  will not be significantly reduced and signal enhancement may not be any higher than signal fluctuations due to the contribution of noise. Conversely, if the concentration of contrast agent is too high, the  $T_2$  in the infused region will be reduced enough to generate signal loss. In this study, the contrast agent infusion concentration was optimized based on the contrast agent relaxivity, the native relaxation times of the hippocampus, and the

porosity of brain tissue. The contrast agent may enter large, fluid-filled spaces (e.g. the 3rd ventricle) or fluid-filled spaces that communicate with the ventricles (e.g. the hippocampal fissure) resulting in a significant dilution from the infused concentration. In this case, the concentration of the contrast agent may be too low to generate substantial  $T_1$  shortening and concomitant signal enhancement in  $T_1$ -weighted images. Additionally, the infusion concentration of Gd-albumin was optimized based on average relaxation times within the hippocampus, generating signal enhancement in a majority of this structure. If a select portion of infused regions have significantly shorter  $T_2$  times than found on average within the hippocampus, the addition of contrast agent may cause  $T_2$  shortening that results in hypointense signal. This could be the cause of hypointense regions within the granule cell layer and corpus callosum.

### **3.5 Conclusions**

Initial studies employed *in vivo*, high resolution MR imaging to assess the influence of tissue structure on contrast agent distribution in the hippocampus after administration by CED. These initial studies were useful for determining regions within the hippocampus that were resistant to contrast agent penetration as well as establishing structures that served as boundaries to the distribution. These initial studies also raised questions as to how the contrast agent distributes dynamically in the hippocampus, why there was an apparent dorsal-ventral hippocampus disconnect and what is the cause of backflow during CED. Extended studies of infusions into the dorsal and ventral hippocampus used *in vivo* DCE-MRI to monitor the evolution of contrast agent distribution after delivery by CED. Additionally, *in vivo* high resolution MR imaging was used to evaluate the final distribution of the contrast agent while obtaining finer anatomical detail of structures within the hippocampus. For select subjects, inline

pressure measurements were performed during infusions demonstrating the potential of these measurements for diagnosing the cause of backflow, predicting the severity of backflow and characterizing the performance of new cannula designs. Dynamic images of the contrast agent distribution suggest that the spatial composition of low hydraulic conductivity regions (e.g. pyramidal cell layers) and high hydraulic conductivity regions (e.g. CA1 subregion) within the hippocampus influences convective transport in this structure. MR images also indicate that contrast agent infused into the dorsal and ventral hippocampus has access to fluid-filled structures that may act as mass sinks (Figure 3-8). Segmentation of dynamic distribution images reveals a constant, linear relationship between  $V_d/V_i$  indicating that the mass sinks may impact the distribution of contrast agent throughout the entire duration of infusion for the infusion sites used in this study. In summary, distribution profiles in the dorsal and ventral hippocampus following CED at a particular infusion site are primarily influenced by 1) the spatial arrangement of high and low hydraulic conductivity regions, 2) the presence of mass sinks and 3) backflow along the cannula.

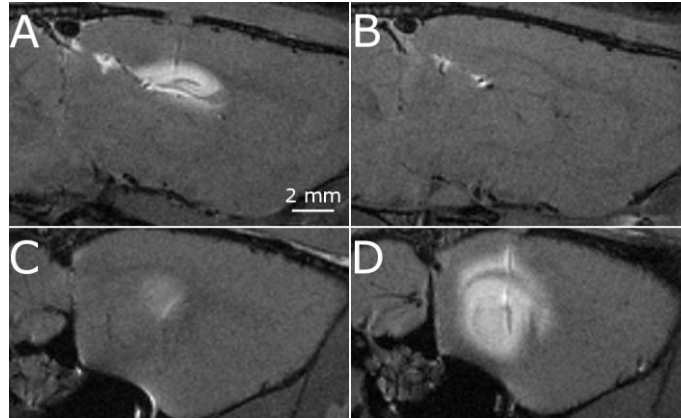


Figure 3-1. Sagittal images of a single rat demonstrating the apparent disconnect between the dorsal hippocampus (top row) and ventral hippocampus (bottom row). The disconnect is seen when the contrast agent is infused into the dorsal hippocampus (A and C) and ventral hippocampus (B and D).

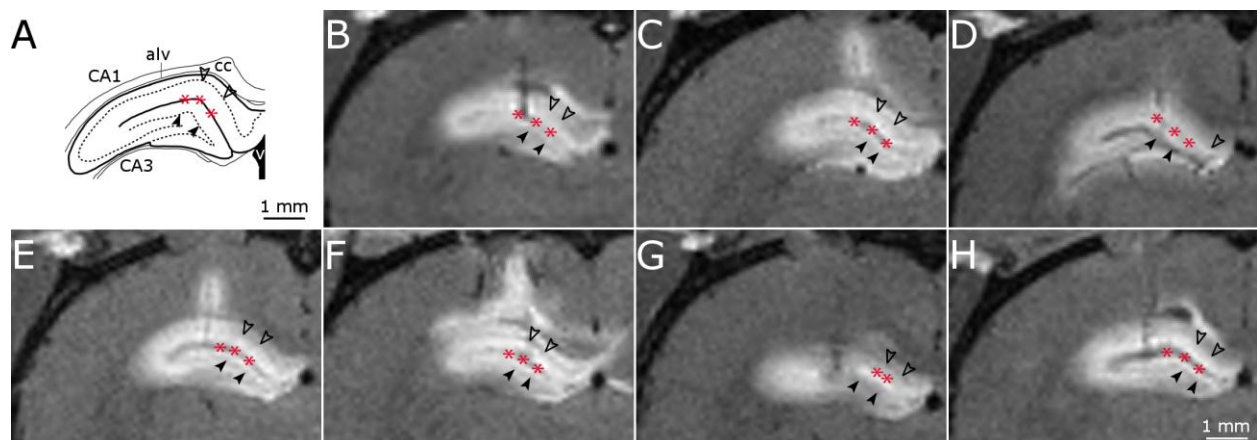


Figure 3-2. High-resolution  $T_1$ -weighted MR images of dorsal hippocampus infusions. A) Schematic of key structures in the dorsal hippocampus adapted from (Paxinos and Watson, 1998). B-H) MR image coronal slice of infusion site for dorsal hippocampus infusions in 7 rats. Filled arrow heads, dentate gyrus granule cell layer; unfilled arrow heads, CA1 pyramidal cell layer; asterisk, hippocampal fissure.

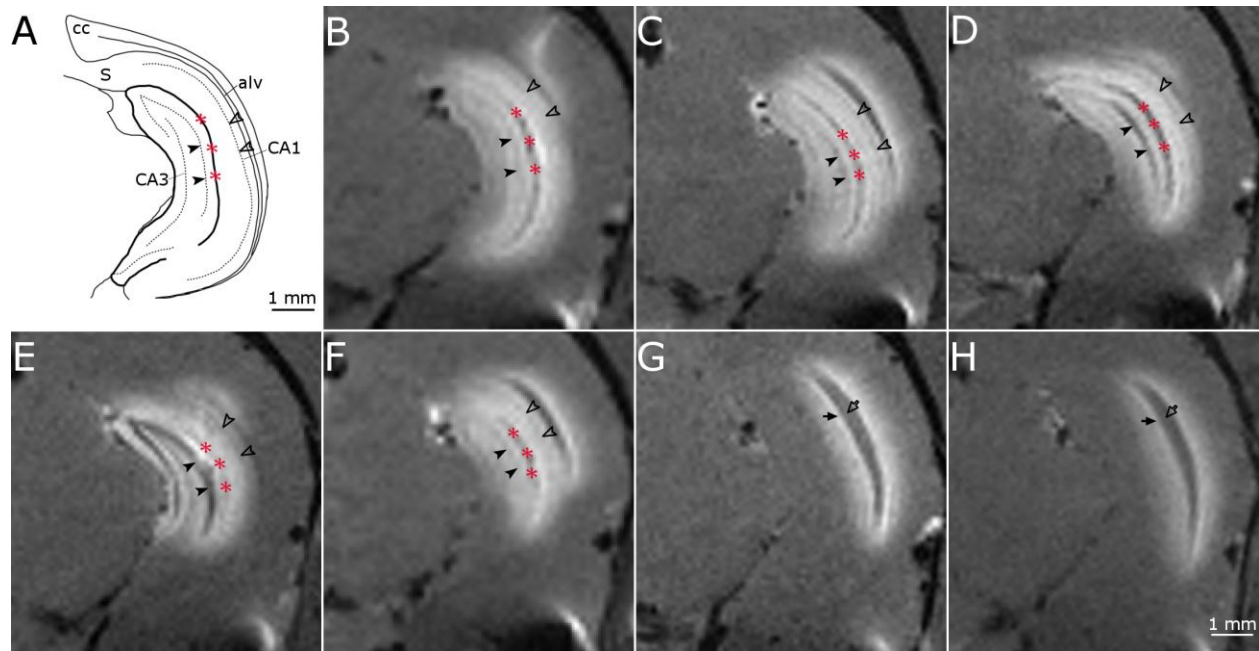


Figure 3-3. High-resolution  $T_1$ -weighted MR images of ventral hippocampus infusions. A) Schematic of key structures in the ventral hippocampus adapted from (Paxinos and Watson, 1998). B-H) MR image coronal slice of ventral hippocampus infusions into 7 rats. Filled arrow heads, dentate gyrus granule cell layer; unfilled arrow heads, CA1 pyramidal cell layer; asterisk, hippocampal fissure, filled arrow, alveus; unfilled arrow, corpus callosum.

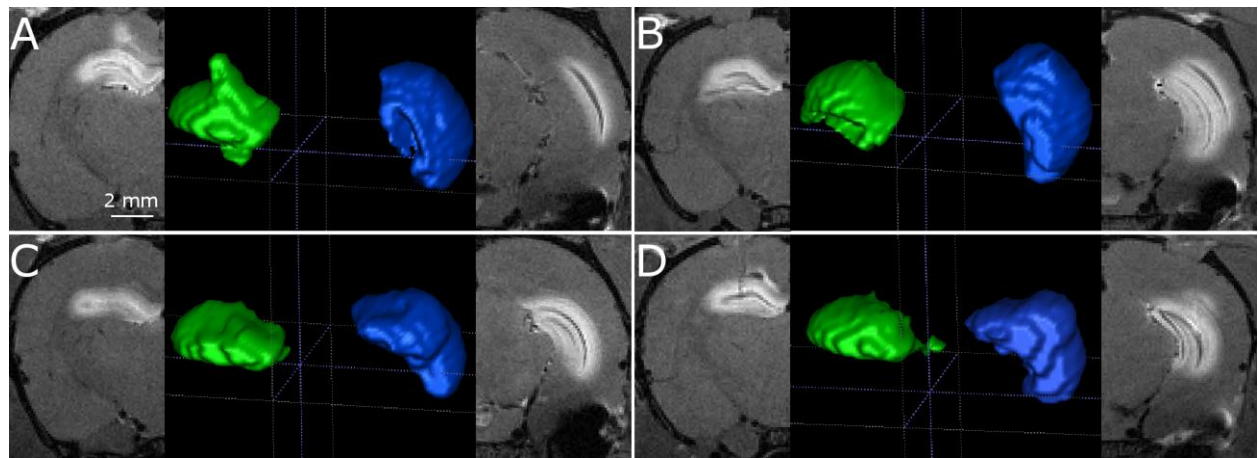


Figure 3-4. High-resolution  $T_1$ -weighted MR image coronal slice of the dorsal hippocampus distribution volume (left image in subfigure) and ventral hippocampus (right image in subfigure) and corresponding segmentation (middle image in subfigure) for 4 rats (A-D).

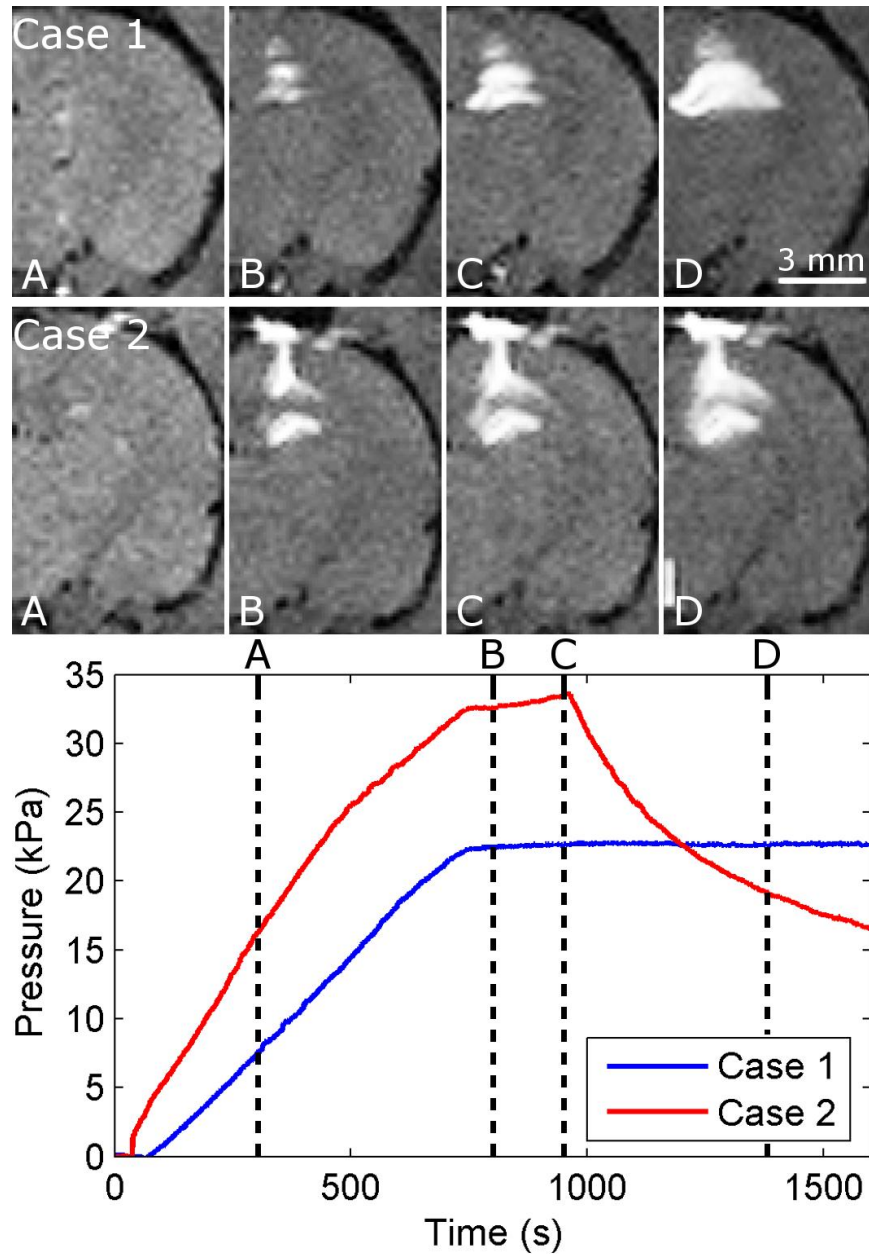


Figure 3-5. Inline pressure measurements and corresponding MR images for mild (Case 1) and severe (Case 2) backflow. The MR images (A-D) show the distribution of the contrast agent at different time points throughout the infusion. The same time points are indicated on the pressure curves by the dashed lines A-D. In case 1, inline pressure steadily increases (A-B) before reaching  $P_{crit}$  where infusate begins to distribute in the dorsal hippocampus and inline pressure reaches a steady-state value (B-D). Conversely, in the severe backflow case, inline pressure increases steadily until infusate enters the hippocampus, corpus callosum, cortex and surface of the brain. The pressure transiently increases (B-C) before decreasing as infusate distributes in the hippocampus, corpus callosum, cortex and surface of the brain (C-D).

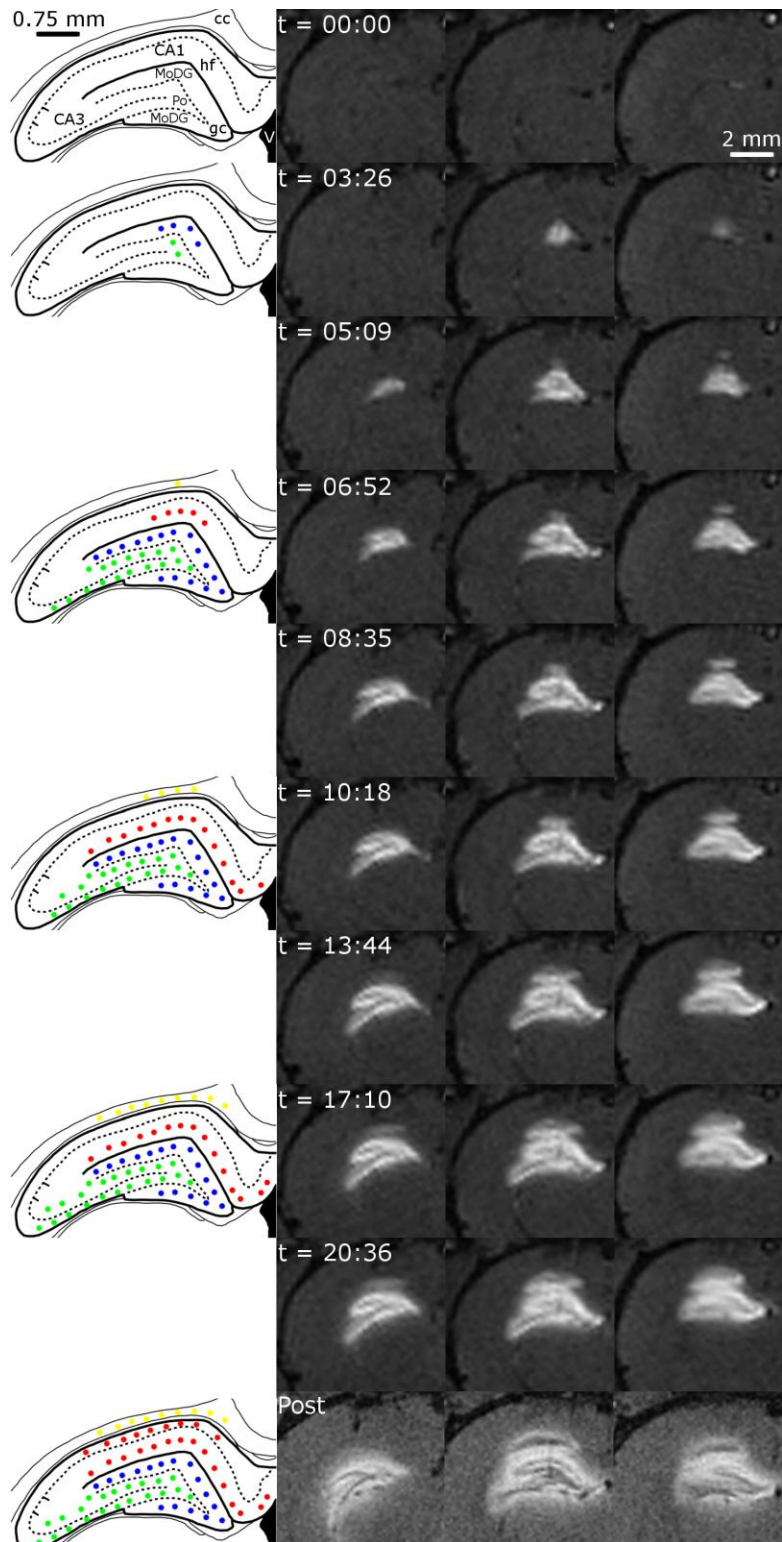


Figure 3-6. DCE-MR images of Gd-albumin infusion into dorsal hippocampus. Dots in schematic (left column) show which structures have been exposed to the contrast agent (blue: molecular layer of dentate gyrus, red: CA1 subfield, green: polymorphic layer of dentate gyrus, yellow: corpus callosum). MR images progress in the posterior to anterior direction (left to right).

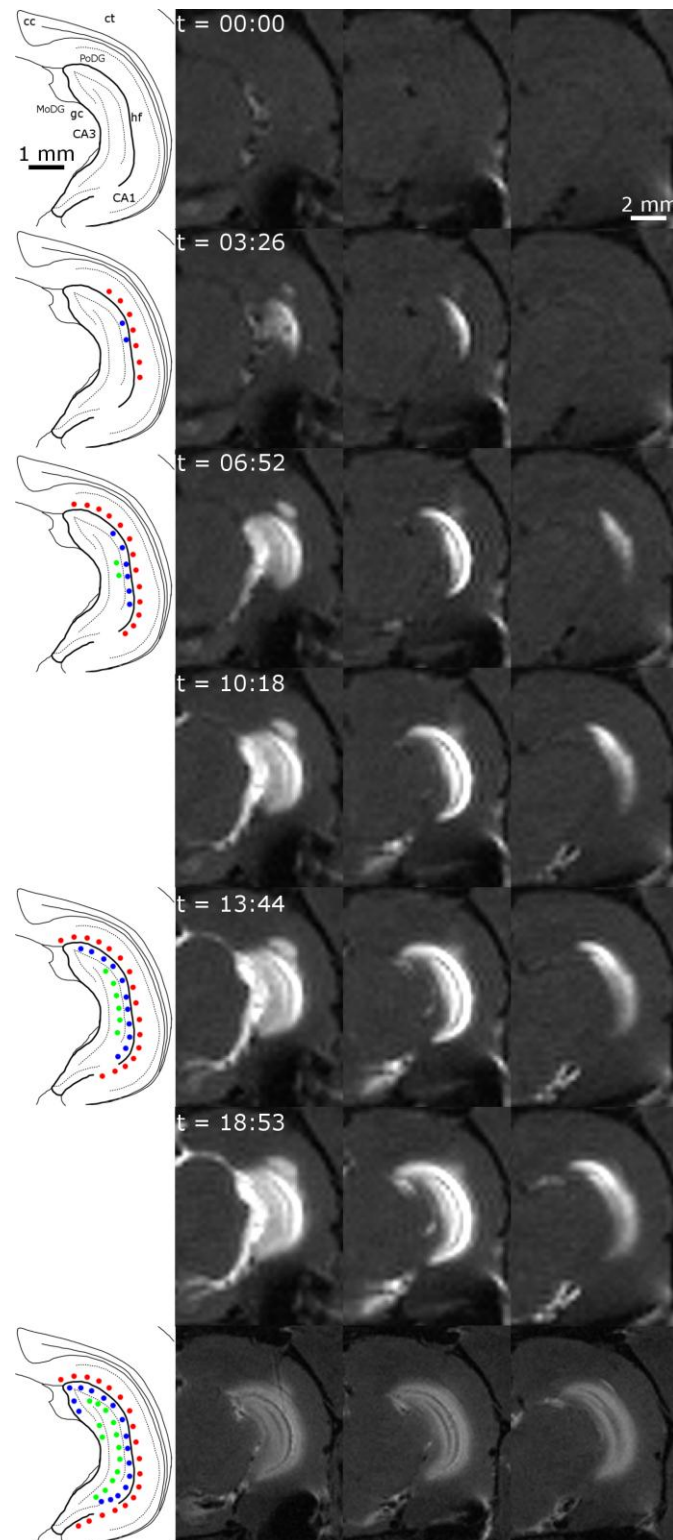


Figure 3-7. DCE-MR images of Gd-albumin infusion into the ventral hippocampus. Dots in schematic (left column) show which structures have been exposed to the contrast agent (blue: molecular layer of dentate gyrus, red: CA1 subfield, green: polymorphic layer of dentate gyrus, yellow: corpus callosum). MR images progress in the posterior to anterior direction (left to right).

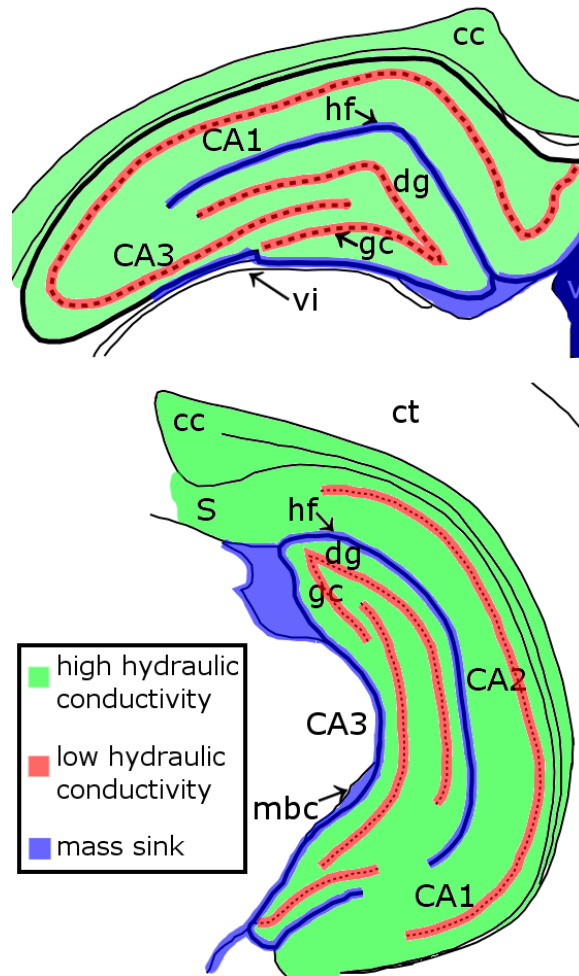


Figure 3-8. Schematic of transport properties in the rat dorsal and ventral hippocampus. Regions determined by experiments to have high hydraulic conductivity (green), low hydraulic conductivity (red), mass sink behavior (blue) are marked within the dorsal (top) and ventral (bottom) hippocampus.

CHAPTER 4  
MEASUREMENT OF GD-ALBUMIN IN VIVO RELAXIVITY IN THE RAT THALAMUS  
AT 11.1 T

**4.1 Introduction**

As reviewed in Section 2.3.4, MR contrast agents generate signal contrast by providing a supplementary avenue of longitudinal ( $T_1$ ) and transverse ( $T_2$ ) relaxation. An important distinction between contrast agents used in MR and other imaging modalities is that signal from MR contrast agents is not measured directly; rather, the effect of the contrast agent on surrounding water protons is observed. The relaxivity of an MR contrast agent parameterizes how efficiently the contrast agent alters neighboring water proton  $T_1$  and  $T_2$  relaxation times. In solution and within a fast exchange regime in compartmentalized media, the relationship observed between relaxation rate and contrast agent concentration is linear and proportional to relaxivity (Caravan et al., 1999; Landis et al., 2000). Therefore, *a priori* knowledge of a contrast agent's relaxivity can be used in conjunction with native relaxation times to determine the concentration of contrast agent in a sample, thus providing a means of quantitatively analyzing CED distributions.

Chapter 3 detailed work in which the macromolecular contrast agent, Gd-albumin, was used as a surrogate for therapeutic agents to evaluate CED in the rat hippocampus (Astary et al., 2010). Gd-albumin was infused into the rat dorsal and ventral hippocampus to determine the influence of tissue architecture on infusate distribution. Since the relaxivity of Gd-albumin in tissue is unknown, only the dynamic and final distribution volumes of the contrast agent could be quantitatively analyzed following CED. Measuring the relaxivity of Gd-albumin would enable the direct measure of

contrast agent concentration profiles, rather than just the spatial distribution, which are more closely related to therapeutic efficacy in a targeted region.

Contrast agent relaxivity in solution can be readily determined by measuring the  $T_1$  and  $T_2$  dependence on contrast agent concentration (Toth et al., 2002); however, the relaxivity of the contrast agent in solution may differ from that in tissue due to compartmentalization of water, binding of the contrast agent to macromolecules, and changes in the microenvironment of the contrast agent (e.g. - pH, temperature, microviscosity) (Laufer, 1987; Stanisiz and Henkelman, 2000; Toth et al., 2002) leading to error in concentration profile measurements. Therefore, the relaxivity of Gd-albumin in brain tissue *in vivo* should be characterized for determining concentration profiles of a contrast agent delivered by CED *in vivo*.

Because of their difficult nature, few studies have investigated the relaxivity of contrast agents *in vivo*. Morkenborg et al. measured the relaxivity of Gd-DTPA in the porcine kidney cortex *in vivo* at 1.5 T and found  $r_1$  and  $r_2$  relaxivity to be reduced by 75% and 60%, respectively, compared to values measured in human plasma solution at 37 °C (Morkenborg et al., 1998). In another study, the relaxivity of Gd-DTPA was measured in the rat kidney cortex at 7 T (Pedersen et al., 2000). The  $r_1$  relaxivity was observed to decrease by 65% while  $r_2$  relaxivity increased by 170% compared to values measured in human plasma at 37 °C. In both studies, the *in vivo* relaxivity of Gd-DTPA in the kidney cortex was substantially different than values measured *in vitro*. Several studies have investigated the relaxivity of MR contrast agents in the rat brain *in vivo*. Pickup et al. (Pickup et al., 2005) investigated the  $r_1$  relaxivity of the low molecular weight tracer, gadodiamide (Gd-DTPA-BMA), in saline and in the injured rat cortex at

4.7 T. It was found that the  $r_1$  relaxivity of gadodiamide was reduced by 17.6% *in vivo* compared to values measured in saline at 37 °C. Additionally, Haar et al. measured the relaxivity of Gd-DTPA at 2.4 T in the rat caudate putamen *in vivo* after delivering the contrast agent using CED (Haar et al., 2010). Interestingly, they found the tissue value of  $r_1$  relaxivity to be similar to values estimated from aqueous solutions of similar macromolecular content at 1.5 T. No studies have addressed the relaxivity of macromolecular agents *in vivo*.

This chapter details work in which the relaxivity of Gd-albumin was first measured at 16.7 °C and 37 °C in a solution of artificial cerebrospinal fluid (aCSF) at 11.1 T with and without the addition of a fluorescent tagging molecule, Evans blue dye. The goal was to determine if tagging the contrast agent altered relaxivity, since Evans blue dye is often used as a fluorescent and optical marker when evaluating CED distributions in animals post mortem for comparison to MR images. Tagging Gd-albumin with Evans blue dye also serves as an indicator of how the relaxivity of the contrast agent may change *in vivo* as biological molecules bind the albumin backbone. Gd-albumin relaxivity was then measured in the rat brain thalamus *in vivo* at 11.1 T. These tissue relaxivity values were compared to relaxivity values in solution to assess the error associated with applying solution-based relaxivity values to *in vivo* tissue contrast agent concentration calculations. Finally, to demonstrate the utility of characterizing contrast agent relaxivity, dynamic concentration profiles of Gd-albumin were calculated after delivering the contrast agent to the rat hippocampus by CED *in vivo*.

The work in this chapter was made possible by the assistance and suggestions of several colleagues. Svetlana Kantorovich (Neuroscience) provided instruction on how to

perform the rodent surgery, assisted with rodent surgeries and helped acquire fresh tissue specimens for analysis. Dr. Jung Hwan Kim (Mechanical and Aerospace Engineering) played a critical role in developing the experimental methods for performing CED during MR imaging. Sung Jin Lee (Mechanical and Aerospace Engineering) assisted with brain tissue porosity measurements by sectioning fresh brain tissue. Dr. Nancy Szabo (Center for Human & Environmental Toxicology) and John Munson (Center for Human & Environmental Toxicology) provided ICP-MS expertise and guidance with regards to sample preparation. John Munson was generous enough to run our samples in addition to the samples he analyzed for his own work.

## **4.2 Methods**

### **4.2.1 MR Phantom Preparation**

Gadolinium-diethylene-triamine pentaacetic acid (Gd-DTPA) labeled human serum albumin (Gd-albumin, MW ~ 86 kDa with ~35 molecules of Gd-DTPA per albumin molecule, R. Brasch Laboratory, University of California, San Francisco, CA) was diluted with artificial cerebrospinal fluid (aCSF) into concentrations of 0.008, 0.0058, 0.0035 and 0.0012 mM. Gd-albumin dilutions were split into two groups (with and without Evans blue dye at 1 mg Evans blue dye/50 mg Gd-albumin) to determine if Evans blue dye affected relaxivity. The Gd-albumin dilutions, including aCSF controls were loaded into NMR capillary tubes (2 mm OD, 1.6 mm ID, Wilmad-LabGlass<sup>®</sup>, Vineland, NJ, USA) and then secured around a 15 mL test tube filled with distilled water for proper RF coil loading (Figure 4-1A and B). A thermocouple was also secured to the test tube to monitor the temperature of the phantom.

#### 4.2.2 Animal Preparation and Surgical Procedures

Experiments were performed on male Sprague-Dawley rats weighing 250-275 g (Relaxivity measurement: n=6, Porosity measurement: n=4, Concentration profile measurement: n=2) using protocols and procedures approved by the University of Florida Institutional Animal Care and Use Committee. Anesthesia was initiated with xylazine (10 mg/kg, SQ) and isoflurane (4% in 0.4 L/min oxygen), then animals were placed in a stereotaxic Kopf<sup>®</sup> apparatus, and inhalation anesthesia (1.5% in 1.5 L/min oxygen) was delivered via a nose mask. The skull was exposed by a mid-sagittal incision that began between the eyes and extended caudally to the level of the ears to expose the bregma and lambdoidal sutures.

For Gd-albumin relaxivity measurements, burr holes were drilled into the skull to allow cannula access to the left and right posterior thalamic nuclei (AP: -3.36, ML:  $\pm$  2.2, DV:-5.5) and mesencephalic reticular formation (AP:-6.12, ML:  $\pm$  1.8, DV:-6.1) as defined by a rat brain atlas (Paxinos and Watson, 1998). In addition to a control solution of aCSF, a stock of Gd-albumin was diluted in aCSF and tagged with Evans blue dye to produce contrast agent infusion solutions with concentrations of 0.117, 0.088, and 0.059 mM. For the infusion of the four solutions, a silica cannula was stereotaxically placed in each region of the rat thalamus and 2.2  $\mu$ L of infusate was delivered at a rate of 18  $\mu$ L/hr. The infusion system consisted of a 100  $\mu$ L gas-tight syringe (Hamilton<sup>®</sup>, Reno, NV) driven by a syringe pump (Cole-Parmer<sup>®</sup>, Vernon Hills, IL) connected to polyaryletheretherketone (PEEK) tubing (ID = 0.381 mm, OD = 0.794 mm, length ~ 0.25 m, Upchurch Scientific<sup>®</sup>, Oak Harbor, WA). The PEEK tubing was coupled to a silica cannula (ID = 50  $\mu$ m, OD = 147  $\mu$ m, Polymicro<sup>®</sup> Technologies, Phoenix, AZ) via a microfluidic connector. Immediately following the infusion surgery (~30 min), animals

were transported to the 11.1 T magnet and then placed in a MR compatible stereotaxic frame to secure the positioning of the head and support the placement of the RF coil. Prior to imaging, saline (2 mL) was administered subcutaneously to animals to avoid dehydration, and anesthesia was maintained (~1.5% isoflurane in 1 L/min oxygen) throughout MR imaging. Respiration rate and core temperature were monitored using a small animal monitoring system (SA Instruments, Model 1025, Stony Brook, NY) and maintained at 25-40 breaths per minute and  $37 \pm 0.12$  °C, respectively.

For concentration profile measurements, the silica cannula was coupled to the 100  $\mu$ L gas-tight syringe via six meters of PEEK tubing (ID = 0.254 mm, OD = 1.588 mm, Valco<sup>®</sup> Instruments, Houston, TX) to insure the syringe pump could operate at a safe distance from the magnet. Three millimeter burr holes were drilled into the skull above infusion sites in the dorsal dentate gyrus of the hippocampus (AP: -3.7, ML: -2.2, DV: -2.75) of one rat and the ventral CA1 subregion of the hippocampus (AP: -5.88, ML: 5.1, DV:-5.5) of another. The cannula was then stereotaxically inserted into the brain 0.25 mm deeper than the targeted region of the hippocampus. After 5-10 minutes, the cannula was retracted 0.25 mm and then secured in place using skull fixture adhesive (Cranioplastic<sup>®</sup>, PlasticsOne<sup>®</sup> Inc., Roanoke, VA, USA). This cannula retraction method was implemented to reduce delayed infusion and administration of a bolus injection due to cannula clogging. Immediately following the infusion surgery (~2 hours), the animals were transported to the 11.1 T magnet for MR imaging. After animals were placed within the magnet bore, 8  $\mu$ L of Gd-albumin was infused into the targeted hippocampus at a rate of 18  $\mu$ L/hr.

### 4.2.3 MR Imaging

MR experiments were performed using a Bruker<sup>®</sup> Avance imaging console (Bruker<sup>®</sup> NMR Instruments, Billerica, MA) connected to a Magnex Scientific<sup>®</sup> 11.1 T horizontal bore magnet system (Varian<sup>®</sup>, Inc., Magnex Scientific<sup>®</sup> Products, Walnut Creek California).

#### 4.2.3.1 Phantom measurements

The MR phantom, comprised of NMR capillary tubes containing dilutions of Gd-albumin in aCSF, was centered in a transmit and receive, quadrature, birdcage volume coil.  $T_1$  measurements were acquired with an inversion-recovery spin echo sequence using axially-oriented slices with a  $2.7 \times 2.7$  cm FOV, matrix size of  $150 \times 150$  with 10, 1 mm thick slices, 2 averages, TR = 3000 ms, TE = 10 ms, and TI = 125, 250, 500, 1000, 2000 and 2500 ms (Figure 4-1C).  $T_2$  data was acquired with a spin echo sequence with  $2.7 \times 2.7$  cm FOV, matrix size of  $150 \times 150$  with 7, 1 mm thick slices, 1 average, TR = 3000 ms, TE = 25, 50, 75, 100, 125 and 150 ms.  $T_2$  data was acquired with a minimally diffusion-weighted spin echo sequence, where the readout dephasing gradient is placed adjacent to the readout gradient after the 180 degree RF pulse. Data was acquired with the phantom at ambient temperature (16.7 °C) and at physiological temperature (36.8 – 37.0 °C). Warm air was blown over the phantom to heat it to physiological temperature and measurements were delayed until this temperature was maintained for 30 minutes.

#### 4.2.3.2 Rat brain *in vivo*

For relaxivity measurements, animals were placed in a custom, MR-compatible, stereotaxic frame designed to fit inside of a transmit-only, actively-decoupled, quadrature birdcage volume coil with an inner diameter of 8.3 cm (Figure 4-2). A custom-made, receive-only, passively-decoupled quadrature surface coil (180 degree

arc, length = 3.7 cm, constructed on half-cylinder with OD = 4.7 cm and ID = 4.1 cm) was then placed on the head of the rat.  $T_1$  and  $T_2$  measurements were acquired with a spin echo sequence using axially-oriented slices with a 2.4 × 2.4 cm FOV, matrix size of 104 × 104 with 10, 1 mm thick slices and 2 averages. Spin echo  $T_1$  progressive saturation data was acquired with TR = 5000, 2000, 1500, 1000, 750, 500 and 250 ms and TE = 15 ms.  $T_2$  data was acquired with a minimally diffusion-weighted spin echo sequence, where the readout dephasing gradient is placed adjacent to the readout gradient after the 180 degree RF pulse, with TE = 15, 20, 25, 30, 45, 60 and 75 ms and TR = 2000 ms.

For concentration profile studies,  $T_1$  measurements were acquired prior to infusion with a spin echo sequence using axially-oriented slices with a 2.4 × 2.4 cm FOV, matrix size of 104 × 104 with 10, 1 mm thick slices and 2 averages. Spin echo  $T_1$  progressive saturation data was acquired with TR = 5000, 2000, 1000, 500 and 250 ms and TE = 15 ms. To determine the pre-contrast enhancement baseline signal in brain tissue, three transverse  $T_1$ -weighted spin echo images were obtained with a TR = 330 ms, TE = 9.4 ms, 2.4 × 2.4 cm FOV, matrix size of 104 × 104 with 10, 1 mm thick slices and 6 averages. During the infusion,  $T_1$ -weighted spin echo image measurements were repeated serially to capture the evolution of the infusate distribution. Each scan was obtained with a total acquisition time of ~ 3.5 min and a total of 12 scans were acquired over a 42 min period of time during infusion.

#### **4.2.4 Measurement of Gd-albumin Concentration in Tissue**

After MR imaging, animals were sacrificed and a vibratome (Leica<sup>®</sup> VT1000 A, Leica<sup>®</sup> Microsystems Inc., Buffalo Grove, IL, USA) was used to section the fresh brains into 300 μm thick slices. The infusion sites were identified by the presence of Evans

blue dye (Figure 4-3C) and sampled by flash-freezing the brain slices in liquid nitrogen for 4 seconds and extracting the infused region with a tissue punching tool (NIH Style Neuro Punch, OD/ID = 1/0.69 mm, Fine Science Tools<sup>®</sup> Inc., Foster City, CA, USA). Samples from each infusion site were harvested separately, weighed, and then digested with 1 mL of 70% (w/w) nitric acid (Nitric Acid ULTREX<sup>®</sup> II Ultrapure reagent, J.T. Baker, Avantor Performance Materials, Phillipsburg, NJ, USA) for 24 to 48 hours at room temperature. In addition to brain tissue samples, 0.2 mL of the 0.117 mM Gd-albumin solution was digested to verify the concentration of gadolinium in solution. After complete digestion, each sample was diluted with 3 mL of pure water and then filtered with a 0.20  $\mu\text{m}$  pore-size syringe filter (Corning<sup>®</sup> 28 mm Syringe Filter, Corning<sup>®</sup> Incorporated, Corning, NY, USA) to remove particulate matter. The concentration of Gd-albumin was then measured in each sample by using ICP-MS to measure the concentration of gadolinium and assuming 35 molecules of gadolinium per molecule of Gd-albumin.

The small sample sizes of the infused regions of tissue yielded inconsistent Gd-albumin concentration measurements; therefore, a separate experiment was performed to measure the porosity ( $\phi$ ) of infused tissue and determine the tissue concentration ( $C_t$ ) of Gd-albumin based on Equation 4-1, where  $C_i$  is the infusate concentration,

$$C_t = \phi C_i . \quad (4-1)$$

In these porosity measurements, burr holes were drilled into the skull to allow cannula access to the left and right posterior thalamic nuclei (AP: -4.36, ML:  $\pm$  2.2, DV: -5.5). A stock of Gd-albumin was diluted in aCSF to a concentration of 0.117 mM and tagged with Evans blue dye. A silica cannula was then stereotaxically placed in a region of the

rat thalamus and 5.0  $\mu\text{L}$  of infusate was delivered at a rate of 18  $\mu\text{L/hr}$ . Finally, animals were sacrificed  $\sim 30$  min after infusion so that brain tissue could be sampled to determine the concentration of Gd-albumin in tissue using the same concentration analysis applied to brains infused for MR imaging. The measured  $C_i$  and  $C_t$  in porosity experiments was used to calculate  $\phi$  according to Equation 4-1. The measured  $\phi$  was then used in relaxivity calculations to determine  $C_t$  from the measured  $C_i$  in relaxivity experiments.

#### 4.2.5 Data Analysis and Statistical Methods

Image processing and curve-fitting was performed using software written in the Interactive Data Language (Exelis Visual Information Solutions<sup>®</sup>, Inc., Boulder, CO). Regions of interest (ROI's) were drawn to encompass the NMR capillary tubes (Phantom measurements, Figure 4-1C) or distributed contrast agent at each infusion site (*in vivo* measurements, Figure 4-3A and B).  $T_1$  was calculated using an inversion-recovery model and saturation-recovery model for phantom and *in vivo* experiments, respectively.  $T_2$  was calculated for phantom and *in vivo* data using a spin echo decay model with a Levenberg-Marquardt least-squares algorithm (Haacke et al., 1999).  $T_1$  and  $T_2$  data was then imported into R (Ihaka and Gentleman, 1996) to determine  $r_1$  and  $r_2$  relaxivity by linear regression according to Equation 4-2 where  $i = 1,2$ ,  $1/T_i$  is the measured relaxation rate,  $1/T_{i0}$  is the native relaxation rate in the absence of contrast agent and  $C_t$  is the concentration of Gd-albumin in solution for phantom measurements and in tissue for *in vivo* measurements,

$$\frac{1}{T_i} = \frac{1}{T_{i0}} + r_i C_t \text{ where } i = 1,2. \quad (4-2)$$

A t-test for comparing the slopes of two regression lines (Armitage and Berry, 1994) was used to compare relaxivity values measured in solution with and without Evans blue dye, and to compare relaxivity values of Gd-albumin tagged with Evans blue dye measured in solution and *in vivo*. The power of the test was determined using the method outlined by Dupont and Plummer (Dupont and Plummer, 1998). A sensitivity analysis was performed to determine the relative importance of the measured  $\phi$  when calculating relaxivity using Equations 4-1 and 4-2. Gd-albumin relaxivities were calculated by repeatedly performing linear regression with the *in vivo*  $T_1$  and  $T_2$  data for many values  $C_t$  for the known  $C_i$  and  $\phi$  ranging from 0.1 to 0.6.

Additionally, concentration profiles were calculated using the measured *in vivo* relaxivities for dynamic infusions into the rat dorsal and ventral hippocampus monitored using dynamic contrast-enhanced MRI (DCE-MRI). The time-dependent concentration profiles were calculated by measuring pre-infusion  $T_1$  maps ( $T_{10}$ ) and taking the ratio of the signal during infusion,  $S(C)$ , to the pre-infusion signal,  $S(0)$ , as shown in Equation 4-3 (Chen et al., 2008),

$$\frac{S(C)}{S(0)} = \frac{\left[1 - e^{-TR(1/T_{10} + r_1 C)}\right] \cdot e^{-TE \cdot r_2 \cdot C}}{1 - e^{-TR/T_{10}}}. \quad (4-3)$$

Under the condition that  $\exp(-TE \cdot r_2 \cdot C) \approx 1$ , concentration can be solved for explicitly as shown in Equation 4-4,

$$C = \frac{1}{r_1} \left[ \frac{1}{TR} \ln \frac{S(0)}{S(0) - S(C) \cdot \left[1 - e^{-TR/T_{10}}\right]} - \frac{1}{T_{10}} \right]. \quad (4-4)$$

## 4.3 Results

### 4.3.1 Relaxivity of Gd-albumin in aCSF

Linear regression was performed on the  $T_1$  and  $T_2$  data as a function of Gd-albumin concentration as described in Equation 4-2 for Gd-albumin in solutions of aCSF at  $16.7 \pm 0.1$  °C and  $37.0 \pm 0.2$  °C. Relaxivity was measured to be  $r_1 = 114 \pm 3$  mM<sup>-1</sup>s<sup>-1</sup> ( $r^2 = 0.98$ ) and  $r_2 = 377 \pm 31$  mM<sup>-1</sup>s<sup>-1</sup> ( $r^2 = 0.882$ ) for Gd-albumin in aCSF at 16.7 °C with values reported as mean  $\pm$  standard deviation (Figure 4-4A and B). Gd-albumin relaxivity was measured to be  $r_1 = 99 \pm 2$  mM<sup>-1</sup>s<sup>-1</sup> ( $r^2 = 0.98$ ) and  $r_2 = 634 \pm 45$  mM<sup>-1</sup>s<sup>-1</sup> ( $r^2 = 0.882$ ) in aCSF at 37 °C. The relaxivities of Gd-albumin with Evans blue dye in aCSF (Figure 4-4C and D) were measured to be  $r_1 = 126 \pm 3$  mM<sup>-1</sup>s<sup>-1</sup> ( $r^2 = 0.98$ ) and  $r_2 = 458 \pm 31$  mM<sup>-1</sup>s<sup>-1</sup> ( $r^2 = 0.89$ ) at 16.7 °C and  $r_1 = 106 \pm 3$  mM<sup>-1</sup>s<sup>-1</sup> ( $r^2 = 0.98$ ) and  $r_2 = 767 \pm 41$  mM<sup>-1</sup>s<sup>-1</sup> ( $r^2 = 0.89$ ) at 37 °C. The 10% reduction in  $r_1$  relaxivity of untagged Gd-albumin compared to tagged Gd-albumin at 16.7 °C was found to be statistically significant ( $p = 0.0013$ , power = 0.973). At 37 °C, the difference between untagged albumin and tagged albumin was still statistically significant ( $p = .0135$ , power = .99) with untagged albumin having an  $r_1$  8% lower than tagged albumin. Untagged Gd-albumin had an  $r_2$  relaxivity that was 17% lower than tagged albumin at 16.7 °C and 37 °C ( $p = .019$ , power  $\sim 1$ ).

### 4.3.2 *In Vivo* Relaxivity of Gd-albumin in the Rat Thalamus

The porosity of the rat thalamus was measured to be  $\phi = 0.24$  ( $n = 4$ , SD = 0.03) by infusing a known concentration of Gd-albumin into the tissue and then measuring the tissue concentration using ICP-MS. This porosity measurement was performed independent of the relaxivity measurement. The infusion of four different concentrations of Gd-albumin into the rat thalamus, for the purpose of measuring relaxivity, resulted in

homogenous distributions of contrast agent with an obvious hyperintensity with respect to regions of tissue not exposed to the contrast agent (Figure 4-3A and B). Dark regions were observed within the medial portions of the mesencephalic reticular formation and trigeminothalamic tract within the infused thalamus (Figure 4-3B). Light microscopy confirmed that these regions, lacking the presence of Evans blue dye, were not exposed to the infused contrast agent (Figure 4-3C). Therefore, ROI's were limited to regions of homogeneously infused tissue within the targeted structures rather than encompassing the entirety of the structure. This also served to avoid voxels whose contrast agent concentration would be affected by the limited diffusion of Gd-albumin throughout MR imaging. A saturation-recovery model allowing for longitudinal relaxation between the  $\pi/2$  and  $\pi$  RF pulses was fit to variable TR data to determine  $T_1$  within ROI drawn at the infusion site of each dilution of Gd-albumin infused into the rat thalamus. The non-linear least squares fit resulted in  $T_1$  with a relative standard error of 7.3%, 12.6%, 6.3%, and 9.9% across subjects for infusate concentrations of 0.117 mM, 0.088 mM, and 0.059 mM Gd-albumin with Evans blue dye and an aCSF control, respectively. A spin echo decay model was fit to variable TE data to calculate  $T_2$  within an ROI drawn at the infusion site of each dilution of Gd-albumin for all subjects and resulted in a relative standard error of 5.7%, 7.3%, 3.0% and 3.2% for infusate concentrations of 0.117 mM, 0.088 mM, and 0.059 mM Gd-albumin with Evans blue dye and an aCSF control, respectively.

Linear regression was performed on the *in vivo*  $T_1$  and  $T_2$  data as a function of Gd-albumin  $C_t$  (Equation 4-2) determined by the known infusate concentration ( $C_i$ ) and measured  $\phi$  (Equation 4-1). The *in vivo* relaxivities of Gd-albumin labeled with Evans

blue dye were measured to be  $r_1 = 25 \pm 1 \text{ mM}^{-1}\text{s}^{-1}$  (Figure 4-5A) and  $r_2 = 432 \pm 38 \text{ mM}^{-1}\text{s}^{-1}$  (Figure 4-5B) where the error is reported as the standard error in the slope of the regressed line. The *in vivo*  $r_1$  and  $r_2$  relaxivities of Gd-albumin were reduced by 76% ( $p \ll 0.05$ , power  $\sim 1$ ) and 44% ( $p = 0.0011$ , power  $\sim 1$ ), respectively, in comparison to relaxivity values measured in solution at 37 °C. Table 4-1 summarizes all Gd-albumin relaxivity values measured in this study. Additionally, Tables 4-2 and 4-3 summarize the calculated p-values after comparing  $r_1$  and  $r_2$  relaxivities, respectively, for the preparations of contrast agent used in this study. Because  $C_t$  was determined by Equation 4-1 rather than a direct measurement, a sensitivity analysis was performed to determine the relative importance of the measured  $\phi$  when calculating relaxivity.  $r_1$  varied between 10.1 and 60.5  $\text{mM}^{-1}\text{s}^{-1}$  and  $r_2$  varied between 173 and 1040  $\text{mM}^{-1}\text{s}^{-1}$  for the range of  $\phi$  evaluated (Figure 4-6A). The percent error in relaxivity was plotted as a function of  $\phi$  to determine the contribution of error in the measurement of  $\phi$  to the calculation of relaxivity when assuming  $\phi = 0.24$ , the value measured in this study (Figure 4-6B). For low error in  $\phi$  ( $|\text{error}| < 10\%$ ), the error of the relaxivity measurement is linearly dependent on error in the porosity measurement with a slope  $\sim 1$ . For instance, an error of 5% in the porosity measurement would result in a measured relaxivity value that is 5% different than the actual value. Overestimating  $\phi$  (actual  $\phi < 0.24$ ) results in an error that increases more rapidly than underestimating  $\phi$  (actual  $\phi > 0.24$ ).

#### 4.3.2 CED Concentration Profiles

Dynamic concentration profiles of Gd-albumin infused into the rat dorsal (Figure 4-7A) and ventral (Figure 4-8A) hippocampus, *in vivo*, were calculated using the relaxivity

values measured in this study. The concentration profiles of Gd-albumin within the dorsal and ventral hippocampus exhibited similar behavior with the highest concentrations of contrast agent located within fluid-filled structures such as the hippocampal fissure (dorsal and ventral hippocampus, Figure 4-9A and B) and midbrain cistern (ventral hippocampus, Figure 4-9B). The computed concentrations in these structures (max  $C_t \sim 0.3$  mM) were higher than the infusate concentration ( $C_i = 0.117$  mM). This error could be contributed to the application of tissue relaxivity values for solving the concentration of Gd-albumin in a fluid-filled space. More reasonable values of  $C_t$  were observed in other structures within the hippocampus ( $C_t < C_i$ ). For dorsal hippocampus infusions, computed concentration values were higher than the infusate concentration in 0.08% of voxels and higher than the infusate concentration multiplied by the porosity in 1.4% of voxels. For ventral hippocampus infusions, computed concentration values were higher than the infusate concentration in 0.56% of voxels and higher than the infusate concentration multiplied by the porosity in 7.7% of voxels. Figures 4-7B and 4-8B demonstrate the Gd-albumin concentration time-dependence for select voxels (along the line segment “a-j” in Figure 4-7A and Figure 4-8A) in the dorsal and ventral hippocampus, respectively. Generally, the concentration of Gd-albumin increases quickly with the onset of infusion and then plateaus throughout the remainder of infusion. This concentration behavior is typical of delivery by CED as the infusate is driven by bulk flow through the extracellular space of the targeted region. The highest Gd-albumin concentrations were observed in voxels adjacent to the hippocampal fissure and infusion site.

## 4.4 Discussion

### 4.4.1 Gd-albumin Relaxivity in aCSF

Measurements of Gd-albumin relaxivity in solution were performed on dilutions of the contrast agent with and without labeling using Evans blue dye to determine if its addition would affect relaxivity. Evans blue dye has a high affinity for albumin with ~14 potential binding sites for Evans blue dye on a single albumin molecule (Freedman and Johnson, 1969). Therefore, Evans blue dye is often added to albumin-based contrast agents to provide a fluorescent or light visible marker for high-resolution microscopy images of rat brain sections. This technique can be useful when studying distributions of contrast agent after CED (Astary et al., 2010; Chen et al., 2011) because it allows comparison of *in vivo* distributions of the contrast agent acquired using MRI to high resolution microscopy images of the infused tissue. In this work, Evans blue dye served as a visual indicator of the location of the infused regions of tissue during sample harvesting for tissue concentration measurements with ICP-MS. It was necessary to determine if the addition of Evans blue dye would affect the relaxivity of the contrast agent. A significant change was observed in  $r_1$  and  $r_2$  relaxivity after tagging the Gd-albumin with Evans blue dye. The  $r_1$  relaxivity increased by 7.5% after the addition of Evans blue dye while the  $r_2$  relaxivity increased by 17% at 37 °C.

The effect of Evans blue dye on Gd-albumin relaxivity in solution is interesting and gives some insight as to what factors may alter the contrast agent relaxivity *in vivo*.  $r_1$  relaxivity relies on interaction between the electrons of the paramagnetic center of a contrast agent and surrounding water in such a way that the water is able to “give up” energy to the surrounding lattice in order to return to equilibrium (Bloembergen, 1957; Bloembergen and Morgan, 1961; Lauffer, 1987; Solomon, 1955). This interaction can

occur between water that is directly coordinated with electrons of the Gd ion (inner-sphere relaxivity) or between bulk water protons that interact with contrast agent through hydrogen bonds or diffusion within close proximity of the paramagnetic center (outer-sphere relaxivity) (Caravan et al., 1999; Lauffer, 1987). As described in Section 2.2.4, inner-sphere and outer sphere relaxivity are dependent on the frequency content of the paramagnetic center and water dipole moment interaction with the frequency content being described with a spectral density function. The spectral density function is modulated by reorientation of the water-paramagnetic ion complex which is dependent on the rotational mobility of the contrast agent. Therefore, the binding of Evans blue dye to the albumin backbone may limit rotation of Gd-DTPA or the albumin backbone altering the efficiency with which the contrast agent interacts with surrounding water. Additionally, portions of the Evans blue dye molecule are hydrophobic (aromatic structures such as biphenyl and naphthalene) (Maruthamuthu and Subramanian, 1985) and may self-assemble into large micellar structures, further preventing rotational motion of the Gd-albumin molecule (Stopa et al., 2006).

Transverse relaxivity relies on mechanisms which reduce the phase coherence of protons resulting in a decay of the net magnetization in the transverse plane. One method of spin dephasing is the mutual exchange of energy between bulk hydrogen protons and the Gd electrons, chelating molecules and albumin backbone of the contrast agent (Solomon, 1955). Similar to  $r_1$  relaxivity mechanisms, this energy exchange occurs through inner-sphere and outer-sphere interactions between the bulk water and contrast agent. However, an additional source of spin dephasing is the diffusion of water through magnetic field gradients (Caravan et al., 2009). The Gd ion is

paramagnetic with a volume susceptibility that is much different than diamagnetic water; therefore, in the presence of an external magnetic field a local magnetic field gradient will occur at the interface between the Gd-albumin molecule and surrounding bulk water. This susceptibility-induced magnetic field gradient will scale linearly with field strength leading to a significant source of spin dephasing at 11.1 T (Schenck, 1996). The local magnetic field changes created by the Gd ions will contribute to  $r_2$  relaxivity as long as water is able to diffuse close enough to the contrast agent molecule to experience the local, susceptibility-induced magnetic field gradient. The binding of Evans blue dye to the albumin backbone of the contrast agent probably has little effect on  $r_2$  relaxivity due to susceptibility gradients generated by the paramagnetic ion and the increase in  $r_2$  relaxivity is most likely due to an increase in inner-sphere relaxivity.

#### **4.4.2 Gd-albumin Relaxivity *In Vivo***

In addition to measurements in aCSF, the relaxivity of Gd-albumin was measured in the rat thalamus *in vivo*. This structure was chosen because it is a large, relatively homogenous gray matter tissue structure with potential infusion sites that are far from pial surfaces that may alter infusion concentrations (Jagannathan et al., 2008). In initial studies, infusions were performed in the rat cortex; however, the close proximity of the infusion sites to the surface of the brain led to inconsistent infusions confounding the relaxivity measurement. Because the thalamus is relatively homogenous it would be expected that the infusion profile would be homogenous for regions proximal to the infusion site. Using this method of measuring relaxivity, it is important that the tissue porosity, and concomitant tissue concentration of Gd-albumin, be consistent within the ROI's from which relaxation data was computed. Previous studies have measured the porosity of rat brain tissue (Sykova and Nicholson, 2008); however, the tissue may

dilate in response to the pressure gradients generated during infusion of the contrast agent into tissue (Chen and Sarntinoranont, 2007). Therefore, the estimate of tissue porosity used in this study was derived from ICP-MS analysis of infused tissue samples after CED.

The  $r_1$  and  $r_2$  relaxivities of Gd-albumin tagged with Evans blue was found to significantly decrease *in vivo* when compared to values measured in solution at 37 °C. Longitudinal relaxivity reduced by ~76% while  $r_2$  relaxivity reduced by ~44%. Several factors could explain the reduction of *in vivo* relaxivity. The binding of biological molecules, in addition to Evans blue dye, to the albumin protein may affect the ability of water to interact with the contrast agent. Serum albumin is a transporter molecule that can bind hydrophobic agents such as fatty acids and hormones as well as smaller molecules such as calcium and other ions. As molecules bind the protein backbone of Gd-albumin, they may restrict access of bulk water to the Gd ion, chelating molecule and albumin protein affecting both inner and outer sphere relaxivity. The additional cargo on the Gd-albumin molecule may also increase the distance at which water can diffuse past the molecule effectively weakening the susceptibility-induced dephasing magnetic field gradient experienced by bulk water protons.

In addition to molecular binding, compartmentalization of the contrast agent may also reduce the observed relaxivity *in vivo*. Gd-albumin is a large molecule (~86 kDa) and is restricted to the extracellular space of the brain parenchyma. Therefore, only water in the extracellular space may interact with the contrast agent. The probability that water interacts with the contrast agent will depend not only on the contrast agent concentration but also on the exchange rates between the extracellular compartment,

intracellular compartment and vascular compartments of the brain tissue (Li et al., 2005). If this exchange rate is fast (exchange rate  $\gg$  time-scale of experiment), the relaxation time in a voxel becomes a weighted average of the relaxation times in the three compartments with the contrast agent shortening only the relaxation rate in the extracellular compartment (Zimmerman and Brittin, 1957). On the contrary, if the exchange rate is slow the relaxation times in a voxel must be expressed as a modified Bloch equation that allows for chemical exchange between water in different environments (McConnell, 1958) and the relationship between contrast agent concentration and observed relaxation rate is no longer linear (Landis et al., 2000). In this study, the relationship between observed relaxation rate and contrast agent concentration was found to be linear (Figure 4-5A and B) indicating a fast exchange regime between intra and extracellular water. This result is supported by the observation of monoexponential  $T_1$  and  $T_2$  relaxation in the rat gray matter *in vivo* at 4.7 T (Does and Gore, 2002). However, the same study observed three relaxation components in the trigeminal nerve indicating that water may be in an intermediate or slow exchange regime between the extracellular, myelin and intraaxonal compartments. As with the binding of biological molecules, compartmentalization of Gd-albumin may not reduce  $r_2$  as much as  $r_1$  if the susceptibility induced gradients can affect water in all compartments. This may explain the large reduction in  $r_1$  relative to  $r_2$ .

Previous studies have measured the  $r_1$  relaxivity of the low molecular weight tracer, gadodiamide (Gd-DTPA-BMA), in saline and in the injured rat cortex at 4.7 T (Pickup et al., 2005). It was found that the  $r_1$  relaxivity of gadodiamide was reduced by 17.6%, *in vivo*, compared to values measured in saline at 37 °C. In order to account for

the macromolecular content of tissue, they also measured the relaxivity of Gd-DTPA-BMA in saline solutions containing albumin at 37 °C and found the *in vivo* values of relaxivity to be 22% lower than values measured in saline at comparable macromolecular content. It was concluded that although the macromolecular content of tissue would serve to increase  $r_1$  relaxivity (Stanisz and Henkelman, 2000), compartmentalization of the contrast agent, even in edematous tissue, would limit the interaction of tissue water with the contrast agent and reduce the observed relaxivity. Haar et al. have also measured the relaxivity of Gd-DTPA at 2.4 T in the rat caudate putamen *in vivo* after delivering the contrast agent using CED (Haar et al., 2010). Interestingly, they found the tissue value of  $r_1$  relaxivity to be similar to values estimated from aqueous solutions of similar macromolecular content at 1.5 T. The results of these studies indicate that the relaxivity of low molecular weight Gd-based contrast agents may be reduced by up to 22% in the rat brain *in vivo* or remain unchanged when compared to values measured in saline. Simulations of Gd-DTPA inner-sphere relaxivity as a function of field strength and contrast agent mobility (i.e. – rotational correlation time) indicate that lengthening the correlation time, due to binding, yields lower increases in relaxivity with increasing field strength (Caravan et al., 2009). The discrepancy between the results of Haar et al. at 2.4 T and Pickup et al. at 4.7 T could be attributed to compartmental effects outweighing binding effects at higher field strengths. The findings of Haar et al. apparently contradict the outcome of this study where the  $r_1$  relaxivity was reduced by 76%; however, in the case of Gd-albumin the Gd-DTPA molecules are bound to a protein backbone in solution and *in vivo*. Additionally, Evans blue dye molecules are also bound to the contrast agent backbone

further reducing rotational mobility. Therefore, the effect of reducing correlation times, with a concomitant increase in observed relaxivity, due to macromolecular binding *in vivo* is not realized.

#### 4.4.3 CED Concentration Profiles

*In vivo* relaxivity values measured in the rat thalamus were used to calculate dynamic concentration profiles of Gd-albumin delivered to the rat hippocampus by CED. As shown in Equation 4-4, under the assumption that  $\exp(-TE \cdot r_2 \cdot C) \approx 1$  the concentration of contrast agent is linearly dependent on  $r_1$ . Use of saline values of relaxivity would result in a 76% underestimation of Gd-albumin concentration profiles in the rat brain *in vivo*. Therefore, although our measurements were performed in the thalamus, it may be more appropriate to apply these *in vivo* Gd-albumin relaxivities as an approximation of Gd-albumin relaxivity in other portions of the rat brain for the purposes of contrast agent concentration determination. As a demonstration, dynamic concentration profiles were calculated for infusions by CED into the rat hippocampus (Figures 4-7 and 4-8). The computed profiles resulted in reasonable values of Gd-albumin concentration with only a few voxels having a concentration greater than the infusate concentration. These voxels appear bright red in Figures 4-7A and 4-8A and correspond to the location of the hippocampal fissure in Figure 4-9. The hippocampal fissure is a fluid-filled region that is accessible to the contrast agent during CED (Astary et al., 2010); therefore, it may be more appropriate to apply solution values of Gd-albumin relaxivity to compartment-free voxels in infused regions of tissue. The concentration profiles in Figures 4-7B and 4-8B demonstrate that voxel concentrations of Gd-albumin increase at the onset of infusion and then generally plateau to a steady-state value. This steady-state value should depend on the tissue porosity in the voxel

and the infusate concentration. The tissue porosity near the infusion site should be spatially dependent as the pressure gradient generated at the cannula tip causes spatially-varying dilatation of the surrounding tissue (Chen and Sarntinoranont, 2007). Therefore, the apparent divergence of concentrations at early time points is most likely due to spatially varying porosity as well as partial volume effects where voxels near the infusion site are completely infused while voxels further away are partially infused. The divergence at later time points is due to spatially varying porosity, outlying voxels being partially infused (lower concentrations) while voxels bordering the hippocampal fissure result in concentrations that are an average of infused tissue and the hippocampal fissure (overestimation of concentration). When calculating concentration profiles during CED, it may be worthwhile to segment voxels located in fluid-filled regions of tissue and then apply solution values of Gd-albumin relaxivity to these regions of tissue and tissue values of Gd-albumin relaxivity to compartmentalized tissue. A weighting function could be applied to approximate relaxivity in voxels that contain fractions of compartment-free and compartmentalized tissue.

When calculating Gd-albumin concentrations in the hippocampus using relaxivity values measured in the thalamus, an assumption is made that the relaxivity of the contrast agent would be the same in these two structures. Many of the same biological molecules present in the thalamus, such as those comprising the ECM, would also be expected to be present in the hippocampus. Therefore, changes to relaxivity due to binding should be minimal. However, the hippocampal tissue structure is complex and contains dense, gray matter-like structures in the pyramidal cell layers of the CA1, CA3 and granule cell layer sub regions of the hippocampus with projections from these

structures constituting regions similar to white matter. Additionally, the hippocampal fissure is a fluid-filled region that penetrates the dorsal and ventral hippocampus. Water compartmentalization effects on contrast agent relaxivity could be different in these various regions of the hippocampus as exchange rates of extracellular and intracellular/intraaxonal water change introducing some error in the concentration estimate. Additional error is introduced by the assumption that  $T_2$  effects of the contrast agent are negligible ( $\exp(-TE \cdot r_2 \cdot C) \approx 1$ ). Under the parameters used in this study, the  $T_2$  effects term is  $\sim 0.9$ ; therefore, the concentration profiles calculated in Figures 4-7 and 4-8 are slightly underestimated. Other methods of quantifying concentration, such as using rapid  $T_1$ -mapping methods to measure  $T_1$  at each time point, avoid the need for this assumption but may have limited temporal resolution or be prone to other sources of error. Additionally, while concentration cannot be solved for explicitly in Equation 4-3, numerical methods can be used to solve for concentration. However; use of Newton's method proved to be problematic when calculating concentrations in Figures 4-7 and 4-8 for voxels with a component of signal originating from the hippocampal fissure. These voxels expressed signals that were greater than the theoretically achievable signals according to Equation 4-3 when using the tissue relaxivity values measured in this study. Applying solution-based values of relaxivity to fluid-filled regions and approximated values of relaxivity to voxels containing compartmentalized and compartment-free tissue may be one method of ameliorating this issue. Finally, the infusate concentration can also be limited such that the assumption of negligible  $T_2$  effects holds for all voxels of interest in an infused volume.

## 4.5 Conclusions

In this study, the relaxivity of the macromolecular contrast agent, Gd-albumin, was measured in an aCSF solution before and after labeling with Evans blue dye. The binding of Evans blue dye to the albumin backbone of the contrast agent resulted in a statistically significant increase in  $r_1$  relaxivity (7%) and  $r_2$  relaxivity (17%). Dilutions of Gd-albumin labeled with Evans blue dye were delivered by CED to nuclei within the thalamus and  $T_1$  and  $T_2$  were measured. In order to measure tissue porosity, additional large volume infusions of Gd-albumin were conducted in the rat thalamus and infusate and tissue concentrations of the contrast agent were measured by ICP-MS. Gd-albumin relaxivities were measured by performing linear regression on  $T_1$  and  $T_2$  data as a function of tissue concentration of contrast agent determined by multiplying the measured tissue porosity by the infusate concentration. The  $r_1$  and  $r_2$  relaxivities of Gd-albumin were found to be reduced by 76% and 44%, respectively, *in vivo* in comparison to values measured in solution at 37 °C. As a demonstration of the utility of relaxivity measurements, concentration profiles of Gd-albumin infused into the rat hippocampus, *in vivo*, were measured dynamically. The concentration profiles resulted in reasonable values throughout the hippocampus with an overestimation of concentration in voxels encompassing or bordering the compartment-free hippocampal fissure.

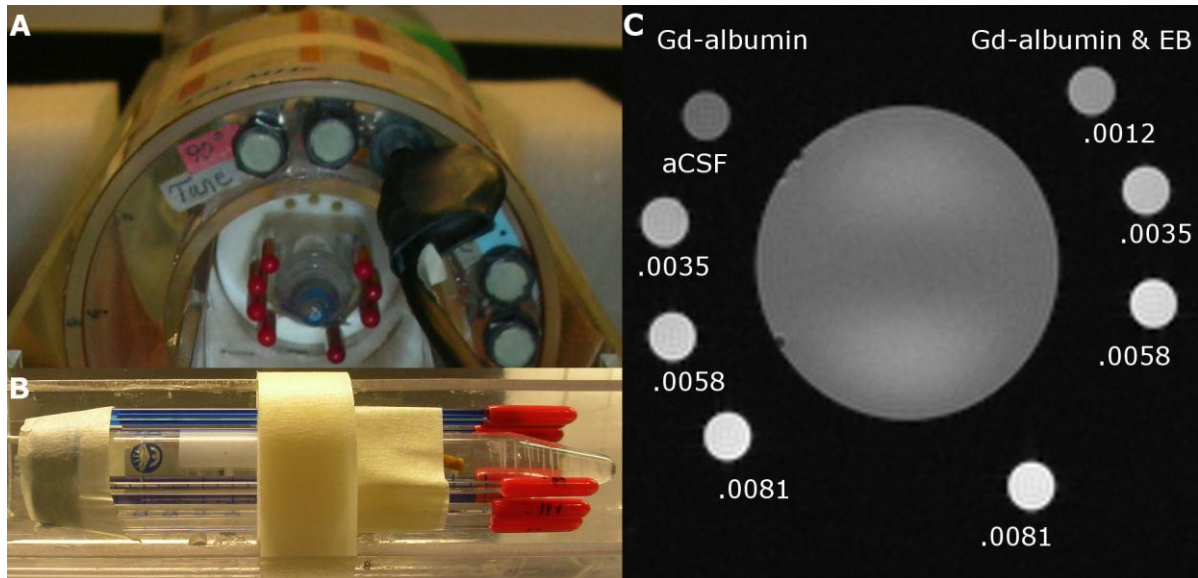


Figure 4-1. The experimental setup used for measurements of Gd-albumin relaxivity in solution. A) A transmit and receive, birdcage volume coil was used for MR imaging. B) NMR capillary tubes were loaded with dilutions of Gd-albumin in aCSF with and without Evans blue dye. The capillary tubes were placed in a holder surrounding a 15 mL test tube for proper RF coil loading. C) T<sub>1</sub>-weighted axial image of phantom setup.

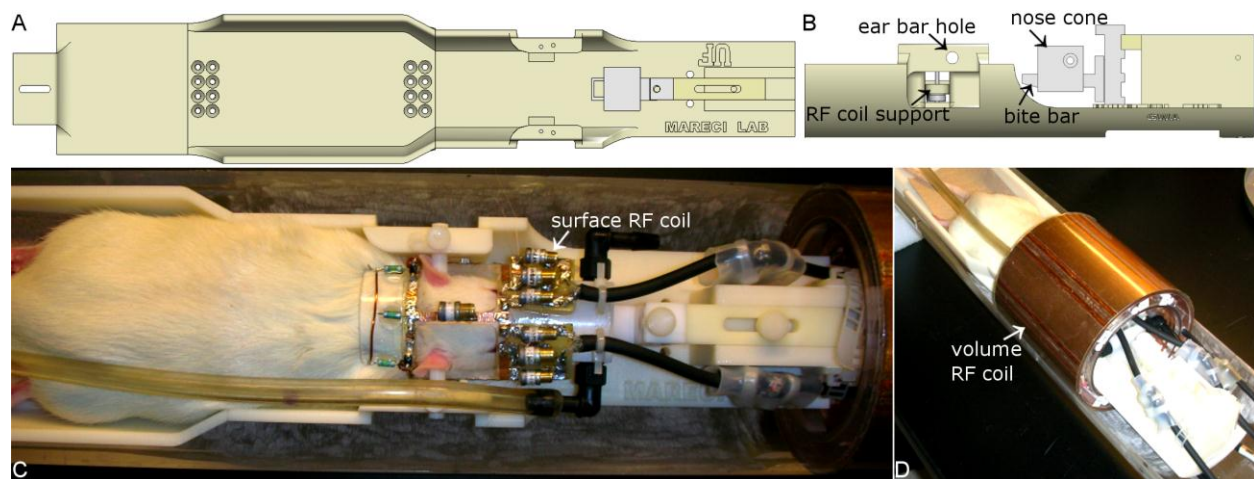


Figure 4-2. The experimental setup used for measurements of Gd-albumin relaxivity in vivo. A) Top view of a custom, MR-compatible stereotaxic frame that was designed in SolidWorks<sup>®</sup> and printed in ABS plastic on a Dimension<sup>®</sup> 3D printer. The frame was designed to support the rat and receive-only RF surface coil while fitting inside a transmit-only volume coil. B) Side view of stereotaxic frame. The arrows indicate (from left to right): the RF surface coil supports, ear bar holders, bite bar, and nose cone. C) Image of rat secured in the stereotaxic frame with a custom-built, quadrature, receive-only surface coil in place. D) After placement of the surface coil, the head of the rat is centered in the volume coil.

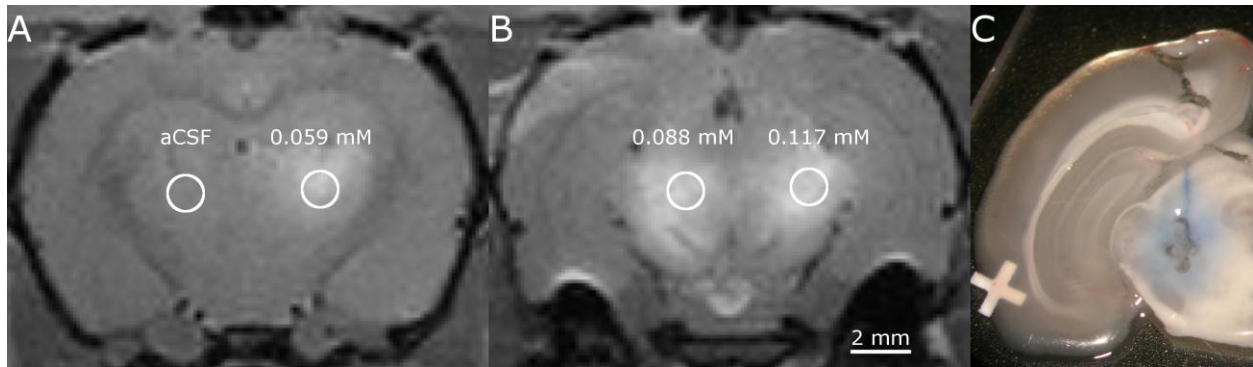


Figure 4-3.  $T_1$ -weighted MR images of the four infusion sites in the rat thalamus (A and B). The white circles indicate ROI's drawn to encompass homogeneous regions of infused tissue. Data from the ROI's were used to calculate  $T_1$  and  $T_2$  as a function of infusate concentration. C) Light microscopy image, corresponding to the 0.088 mM infusion in the middle MR image, of the Evans blue dye distribution in the rat thalamus. This image was taken after samples of tissue were collected from the thalamus.

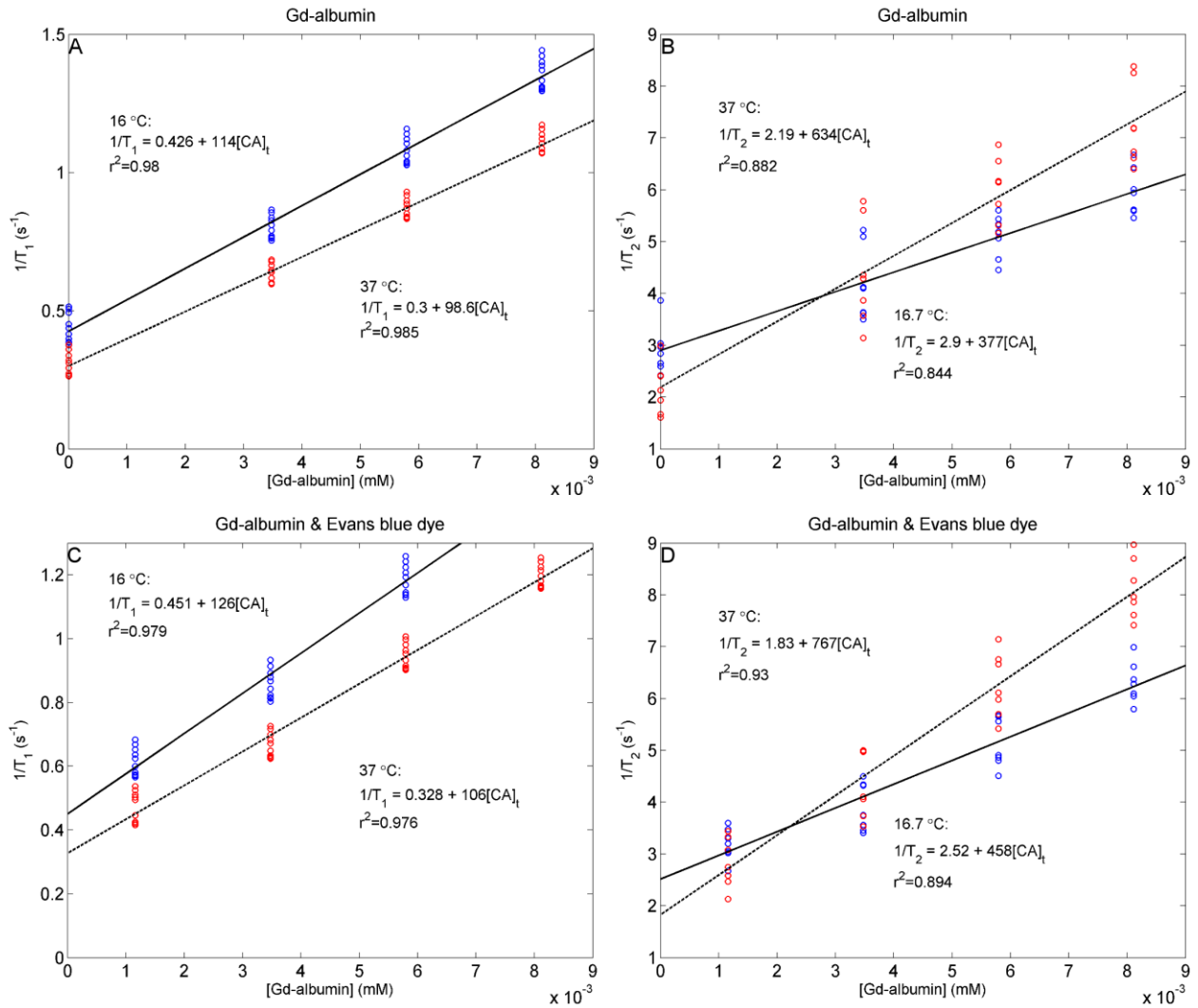


Figure 4-4. Relaxivity of Gd-albumin in aCSF. Linear regression was performed on relaxation time versus concentration data to determine the relaxivity of Gd-albumin without Evans blue dye (A and B) and with Evans blue dye (C and D) in aCSF at 16 °C (blue markers) and 37 °C (red markers).

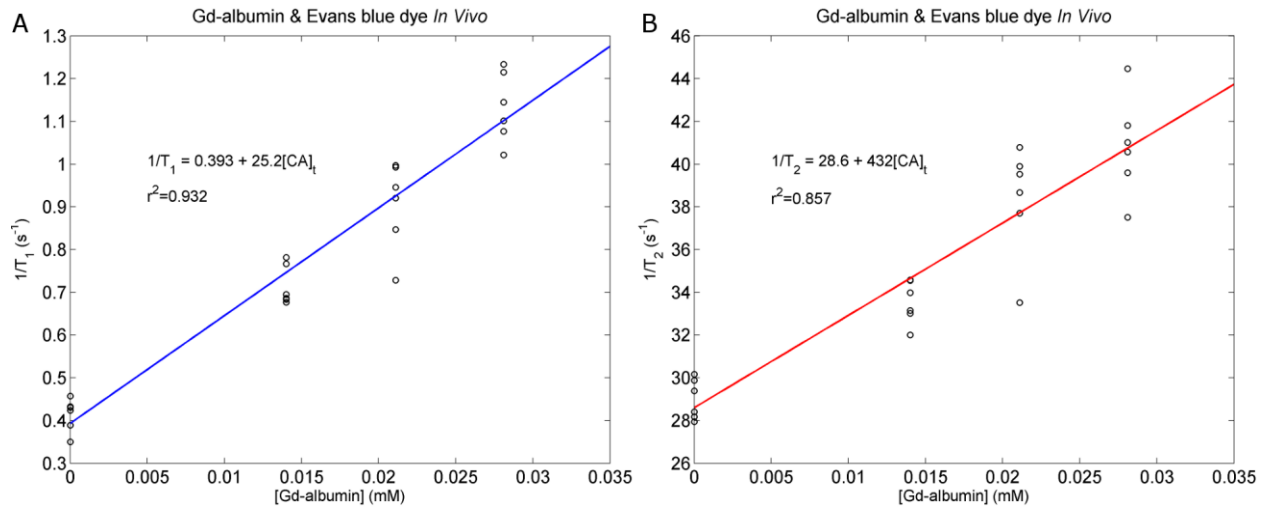


Figure 4-5. Linear regression was performed on relaxation time versus concentration data to determine the  $r_1$  (A) and  $r_2$  (B) relaxivity of Gd-albumin with Evans blue dye in the rat thalamus *in vivo*.

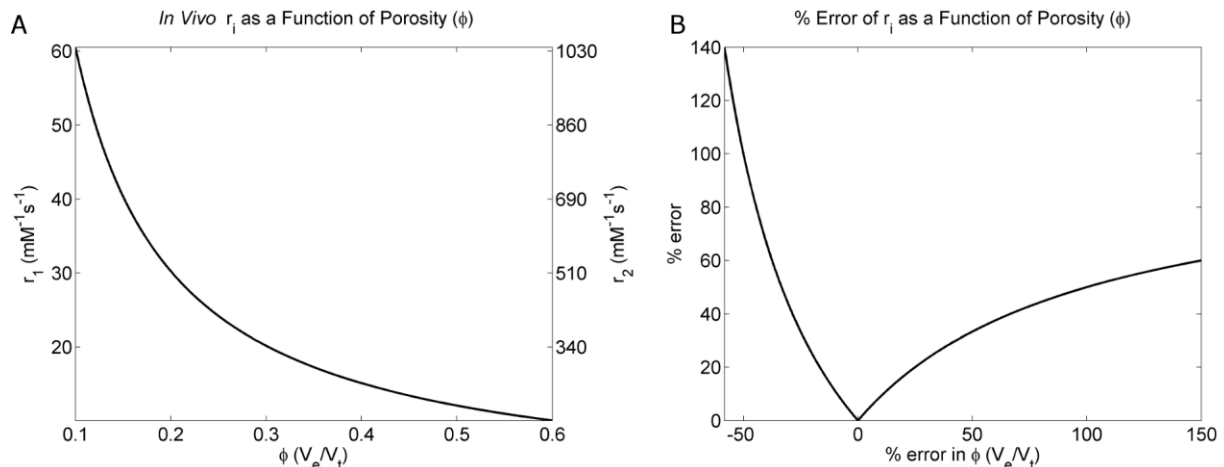


Figure 4-6. Sensitivity of relaxivity curve fit to measured porosity. A) The measured relaxation times and known infusate concentrations were used to calculate the  $r_1$  and  $r_2$  relaxivity of Gd-albumin in the rat thalamus *in vivo* for porosity ranging from 0.1 to 0.6. B) The percent error in the relaxivity measurement was plotted as a function of percent error in the porosity measurement when assuming the actual porosity is 0.24.

Table 4-1. Summary of measured Gd-albumin relaxivity values

Preparation	$r_1$ (mM <sup>-1</sup> s <sup>-1</sup> )	$r^2$	$r_2$ (mM <sup>-1</sup> s <sup>-1</sup> )	$r^2$
aCSF (16.7 °C)	114 ± 3	0.98	377 ± 31	0.84
aCSF with EB (16.7 °C)	126 ± 3	0.98	458 ± 31	0.89
aCSF (37 °C)	99 ± 2	0.99	634 ± 45	0.88
aCSF with EB (37 °C)	106 ± 3	0.98	767 ± 41	0.93
<i>In vivo</i>	25 ± 1	0.93	432 ± 38	0.86

Table 4-2. P-values of statistical comparisons between Gd-albumin  $r_1$  relaxivity measured for various sample preparations.

Preparation	aCSF (16.7 °C)	aCSF with EB (16.7 °C)	aCSF (37 °C)	aCSF with EB (37 °C)	<i>In vivo</i>
aCSF (16.7 °C)	---	0.0013	<< 0.001	0.0269	<< 0.001
aCSF with EB (16.7 °C)	---	---	<< 0.001	<< 0.001	<< 0.001
aCSF (37 °C)	---	---	---	0.0135	<< 0.001
aCSF with EB (37 °C)	---	---	---	---	<< 0.001
<i>In vivo</i>	---	---	---	---	---

Table 4-3. P-values of statistical comparisons between Gd-albumin  $r_2$  relaxivity measured for various sample preparations.

Preparation	aCSF (16.7 °C)	aCSF with EB (16.7 °C)	aCSF (37 °C)	aCSF with EB (37 °C)	<i>In vivo</i>
aCSF (16.7 °C)	---	0.0393	<< 0.001	<< 0.001	0.0774
aCSF with EB (16.7 °C)	---	---	0.0016	<< 0.001	0.0606
aCSF (37 °C)	---	---	---	0.0191	0.0068
aCSF with EB (37 °C)	---	---	---	---	0.0041
<i>In vivo</i>	---	---	---	---	---

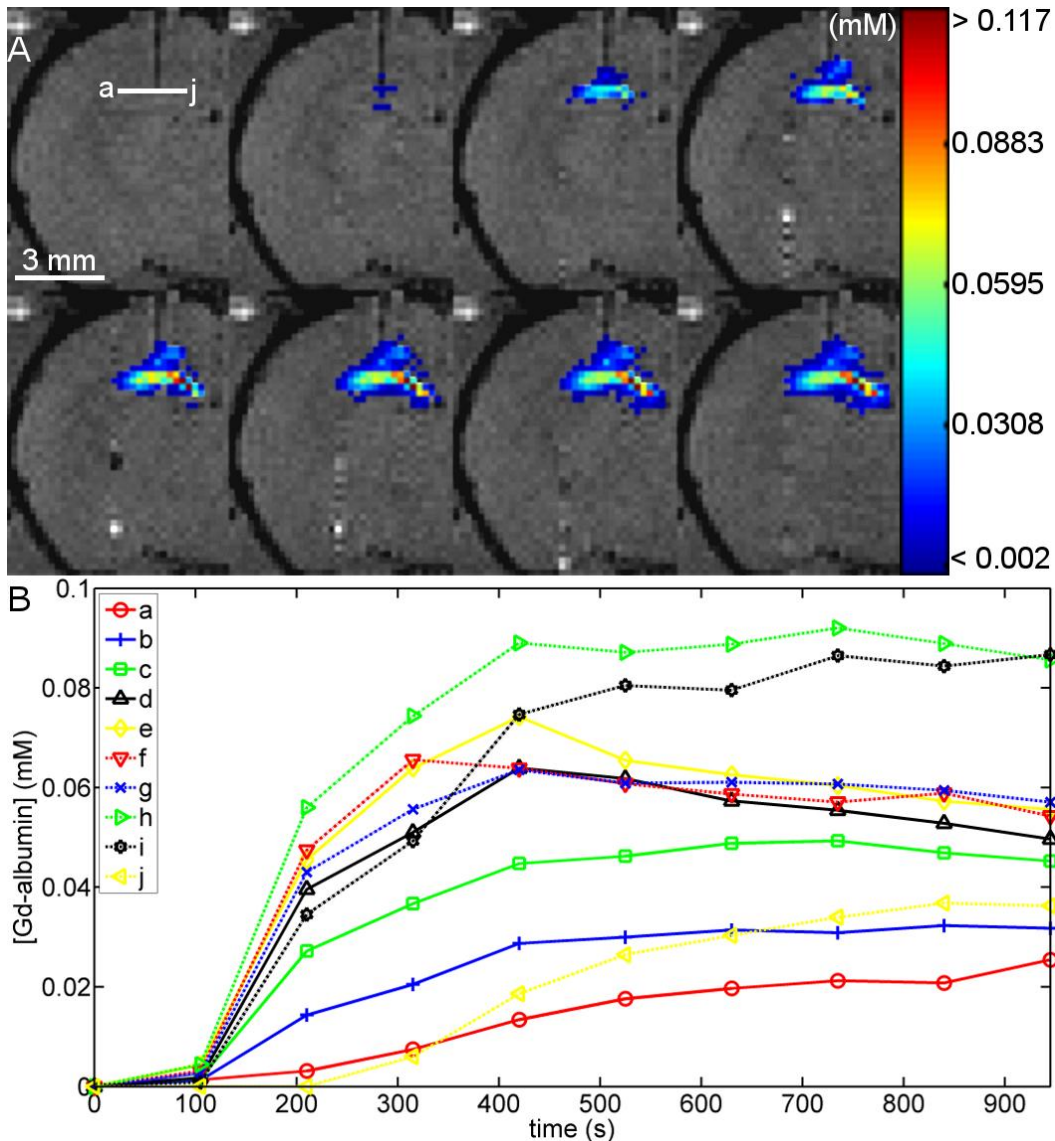


Figure 4-7. The relaxivity of Gd-albumin measured in the rat thalamus *in vivo* was used to calculate concentration profiles of Gd-albumin infused into the rat dorsal hippocampus during CED. A) MR images of the rat brain during infusion with the slice located at the site of infusion. The first image was taken prior to infusion while all other images were acquired serially throughout infusion at a rate of 3.5 min per scan. The measured concentrations are depicted as an overlay on the MR image. B) Concentration of Gd-albumin in voxels from the line segment “a-j” in the top row of images as a function of time.

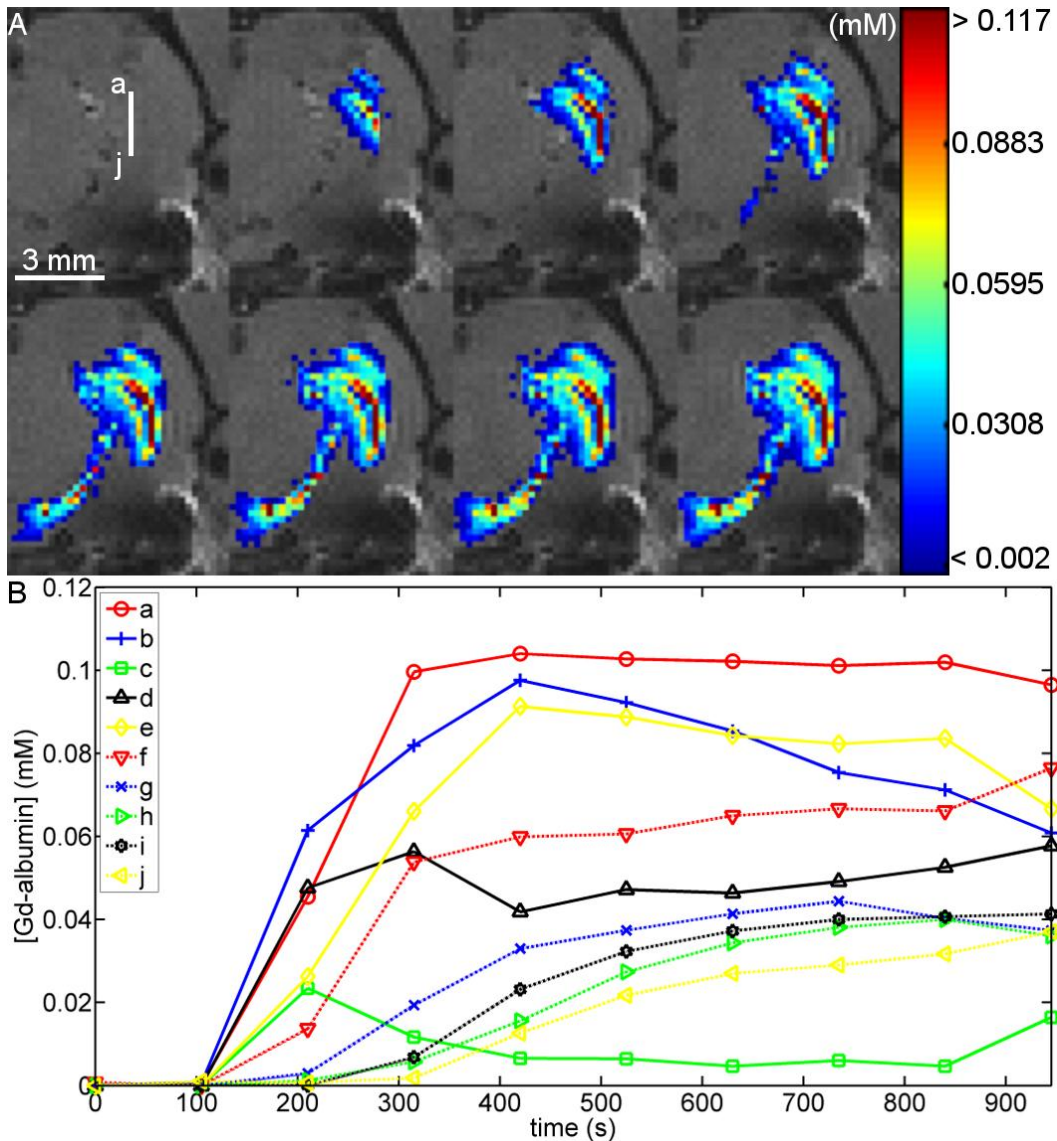


Figure 4-8. The relaxivity of Gd-albumin measured in the rat thalamus *in vivo* was used to calculate concentration profiles of Gd-albumin infused into the rat ventral hippocampus during CED. A) MR images of the rat brain during infusion with the slice located 1 mm posterior to the site of infusion. The first image was taken prior to infusion while all other images were acquired serially throughout infusion at a rate of 3.5 min per scan. The measured concentrations are depicted as an overlay on the MR image. B) Concentration of Gd-albumin in voxels from the line segment “a-j” in the top row of images as a function of time.

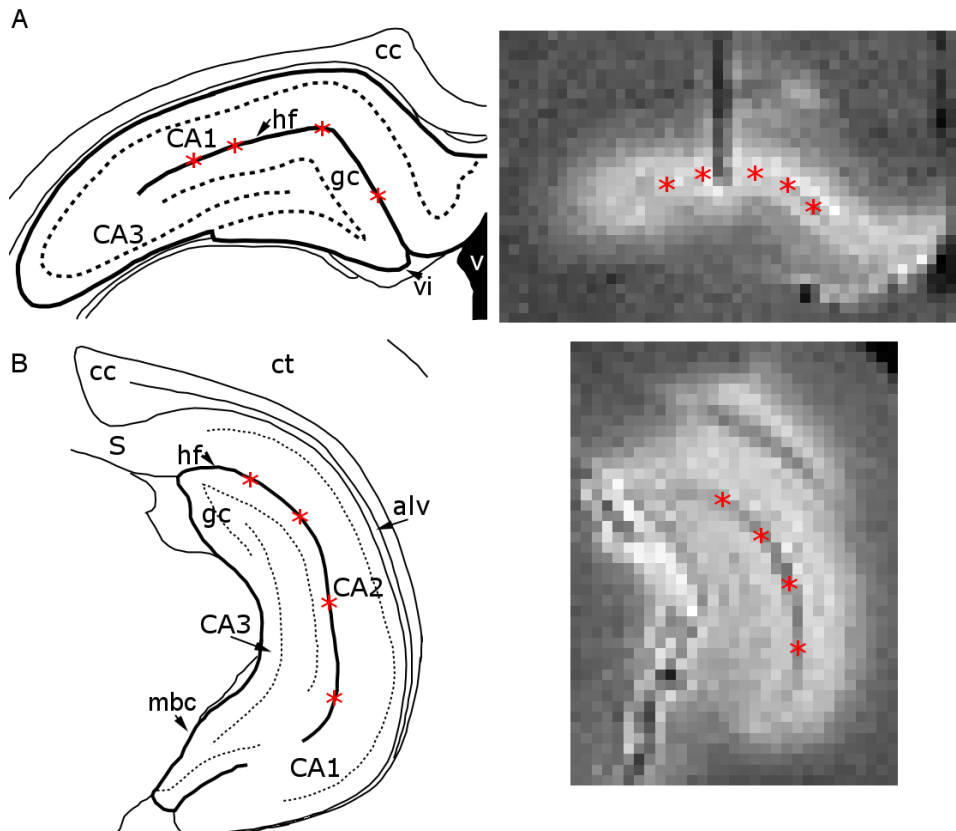


Figure 4-9. Schematic of the rat dorsal (A) and ventral (B) hippocampus adapted from the Paxinos rat atlas (Paxinos and Watson, 1998) with high-resolution MR images of the final contrast agent distribution. The final MR distribution corresponds to the data sets collected for Figures 4-7 and 4-8. List of abbreviations: CA – cornu ammonis area, cc – corpus callosum, ct – cortex, gc – granule cell layer, hf – hippocampal fissure, mbc – midbrain cistern

## CHAPTER 5 DESIGN AND TEST A SUSCEPTIBILITY-MATCHED METAL ALLOY

### 5.1 Introduction

As reviewed in Section 2.3.2, if an object consisting of a spatially varying magnetic susceptibility is immersed in an external magnetic field, local variations in the magnetic induction will arise at the interface between regions of different magnetic susceptibilities. These susceptibility-induced magnetic field perturbations result in magnetic field gradients that may have a complex spatial dependence and can be troublesome for magnetic resonance imaging (MRI) as they are superimposed upon the magnetic field gradients applied to spatially encode the image (Bakker et al., 1993). Consequently, inhomogeneities in the induced magnetic field can contribute to spatial and phase dispersion that can cause signal loss and, if the perturbations are severe enough, lead to geometric distortions from improper spatial encoding. Because the magnetic field perturbations scale linearly with the strength of the applied magnetic field, susceptibility artifacts become more prominent with field strength increases. Therefore, as investigators move to higher magnetic field strengths for gains in signal-to-noise ratio, the issue of magnetic susceptibility becomes one of heightened concern.

In principle, a metal cannula could be used in CED to provide electrophysiological information, as a supplement to coordinates based on a rat atlas or pre-surgical MR imaging, to improve targeting of particular structures. This technique is used to accurately implant deep brain stimulating electrodes for alleviating symptoms due to Parkinson's disease, dystonia and essential tremor (Pollak et al., 2002). However; the large susceptibility mismatch between commonly used metal electrode materials and brain tissue would lead to significant distortions of the MR image (see Figure 2-5 as an

example of MR distortions created by a tungsten wire in water at multiple field strengths). These distortions would obfuscate distributions near the cannula giving an incomplete picture of CED into the infused region. Chapter 3 detailed how the MR contrast agent Gd-albumin was delivered to the rat hippocampus *in vivo* to evaluate how neuroanatomical features of this structure influence CED distributions. These experiments involved examining dynamic and static distributions of the contrast agent in the dorsal and ventral hippocampus to determine what features were influencing transport in these structures. As mentioned in Chapter 3, inconsistent targeting within the dorsal and ventral hippocampus was one source of variability in these studies. Therefore, a metal cannula with EEG functionality could improve similar future studies. Additionally, recent work has been proposed to study functional connectivity in the hippocampus through the amalgamation of optogenetics and functional magnetic resonance imaging (ofMRI). These experiments require the surgical placement of a fiber optic cannula to illuminate light activated ion channels within the hippocampus that are present after transfection with a viral vector containing the genetic code for channelrhodopsin. Such work would benefit from a fiber optic cannula that could double as a recording electrode (“optrode”). A metal alloy that is susceptibility-matched to brain tissue could be used to fabricate cannulae with improved targeting capability for CED and optrodes for simultaneous EEG and ofMRI for studying functional connectivity in the hippocampus.

This chapter details an MRI method of measuring the relative magnetic susceptibility of objects with a fixed cross-sectional profile that can be used to characterize an unknown material. Previous methods have compared simulated and

experimentally acquired image distortions to estimate the susceptibility of cylindrical objects using MRI (Beuf et al., 1996; Carlsson et al., 2006). While these methods were successful in measuring the relative susceptibility of the objects being investigated, they are limited by the computational time required to simulate the MR signal as this analysis is most accurately performed in the time domain (Bakker et al., 1994). The magnetic susceptibility of cylindrical objects has also been estimated by measuring the phase around the object and determining an analytical expression for the complex sum of the MR signal within a pseudo-cylinder which is coaxial to and encompasses the object (Cheng et al., 2007; Cheng et al., 2009b). This method proved highly accurate for estimating the susceptibility of a cylindrical air phantom; however, it is limited to object geometries for which the analytical solution to the magnetic field perturbation is known. The method outlined in this chapter is similar to that of (Cheng et al., 2009a) which employs a Fourier-based method of rapidly simulating external field perturbations for objects with an arbitrary geometry and susceptibility distribution (Marques and Bowtell, 2005). The object's magnetic susceptibility can then be estimated by comparing simulated and measured external field perturbations.

The MR method outlined in this chapter is applied to measure the magnetic susceptibility of four solid-solution alloys of various percent compositions of copper (Cu) and tin (Sn) to explore the potential of modulating the magnetic susceptibility of alloys by altering the ratio of constituent metals. An advantage of creating a solid solution alloy of Cu and Sn is that the magnetic properties of the material should not change with scale (e.g. – 5 mm cylinder should exhibit the same properties as a 50  $\mu\text{m}$  cylinder) or shape. The accuracy of the presented method is determined by comparing magnetic

susceptibilities measured by MR to those measured by super conducting quantum interference device (SQUID) magnetometry. Finally, we evaluate the sensitivity of this method to external field strength, imaging resolution, and factors influencing the simulated object geometry.

This work in this chapter was completed with the assistance of several colleagues. Marcus Peprah (Physics) measured the magnetic susceptibility of the Cu-Sn alloys and distilled and deionized water using a SQUID Magnetometer. Charles Fisher (Materials Science and Engineering) cast the Cu-Sn alloys and characterized their fractional composition using ICP-AES. Hector Sepulveda (Biomedical Engineering, currently Federal Bureau of Investigation) developed the Susceptibility Analysis Software System (SASS) in IDL for simulating the magnetic field perturbations generated by user-defined susceptibility distributions. This code was modified and incorporated into the Magnetic Resonance Imaging Analysis Software (MAS), written in IDL and used by our lab for analyzing MR data, to estimate the susceptibility of objects as per the method outlined in this chapter.

## 5.2 Theory

For linear materials, the magnetic susceptibility ( $\chi_v$ ) describes how the magnetization ( $\mathbf{M}$ ) in a material is related to applied magnetic field intensity,  $\mathbf{H}$  [9], such that

$$\mathbf{M} = \chi_v \mathbf{H}. \quad (5-1)$$

Therefore the induced magnetic field,  $\mathbf{B}$ , in a material is proportional to the sum of the magnetic field and the magnetization induced in the material with the constant of proportionality equal to the permeability of free space,  $\mu_0$ , so

$$\mathbf{B} = \mu_0(\mathbf{M} + \mathbf{H}). \quad (5-2)$$

For a material with a spatially varying magnetic susceptibility,  $\chi_v(\mathbf{r})$ , in an applied magnetic field,  $B_0$ , in the z-direction, the z-component of the magnetization will also have a spatial dependence as shown in the following equation,

$$M_z(\mathbf{r}) = \chi_v(\mathbf{r}) \frac{B_0}{\mu_0(1 + \chi_v(\mathbf{r}))}. \quad (5-3)$$

Therefore, as the applied magnetic field permeates through a sample with spatially varying magnetic susceptibility, local variations in the magnetization will occur at the interface between regions with different magnetic susceptibilities. Additionally, the dipolar fields associated with this magnetization distribution give rise to a spatially dependent induced magnetic field leading to local perturbations of the applied magnetic field (Cheng et al., 2009a; Marques and Bowtell, 2005). Specifically, the dipolar magnetic induction at a position  $\mathbf{r}$ ,  $B_d(\mathbf{r})$ , can be written as

$$B_d(\mathbf{r}) = \frac{\mu_0}{4\pi} \int_V \frac{1}{|\mathbf{r} - \mathbf{r}'|^3} \left( 3 \frac{\mathbf{M}(\mathbf{r}') \cdot (\mathbf{r} - \mathbf{r}')}{|\mathbf{r} - \mathbf{r}'|^2} (\mathbf{r} - \mathbf{r}') - \mathbf{M}(\mathbf{r}') \right) d^3\mathbf{r}'. \quad (5-4)$$

### 5.2.1 Simulation of Magnetic Field Perturbations

Analytical solutions for magnetic field perturbations generated by objects with spherical or cylindrical geometries have been derived (Haacke et al., 1999; Schenck, 1996); however, determining the  $\Delta B(\mathbf{r})$  around arbitrarily shaped geometries with a given  $\chi_v(\mathbf{r})$  requires iteratively solving Equation 5-4. Marques and Bowtell (Marques and Bowtell, 2005) demonstrated that a solution to Equation 5-4 can be determined rapidly in the k-space domain for the z-component of the dipole field by using

$$\mathbf{B}_{d,z}(\mathbf{k}) = \mathbf{B}_d(\mathbf{k}) \cdot \hat{\mathbf{z}} = -\frac{\mu_0 M_z(\mathbf{k})}{3} \left( \frac{k_z^2}{k_x^2 + k_y^2 + k_z^2} - \frac{1}{3} \right), \quad (5-5)$$

where the magnetization distribution in k-space,  $M_z(\mathbf{k})$ , is the Fourier transform of Equation 5-3. Finally, the z-component of the dipole magnetic field can be determined in the spatial domain through an inverse Fourier transformation of  $\mathbf{B}_{d,z}(\mathbf{k})$ , i.e.

$$\mathbf{B}_{d,z}(\mathbf{r}) = \mathcal{F}^{-1}\{\mathbf{B}_{d,z}(\mathbf{k})\}. \quad (5-6)$$

This Fourier method of simulating magnetic field perturbations is summarized pictorially in Figure 5-1.

### 5.2.2 MR Measurement of Magnetic Field Perturbations

The spatially varying induced magnetic field introduces a static background magnetic field gradient with a spatial dependence that can be complex and non-linear. The background magnetic field gradient induces a phase evolution of the excited spin population in addition to the evolution due to the applied linear magnetic field gradients (frequency and phase encoding) for the purposes of spatially encoding the image. The inverse Fourier transform of the time-dependent MR signal, acquired in the presence of a static background magnetic field, results in a complex spin density in the spatial domain that incorporates the frequency encoding and phase dispersion of the background gradient as a geometric distortion and image phase term, respectively. The spatially-dependent image phase of a gradient echo image can be described by Equation 5-7,

$$\varphi_{\text{GE}}(x, y) = -\gamma \Delta B(x, y) \text{TE} + \varphi_0(x, y), \quad (5-7)$$

where  $\varphi_0$  is a phase offset term due to instrumental factors (e.g. – spatial dependence of the RF excitation field). Therefore, the background magnetic field can be quantified

using gradient echo images by dividing the complex form of the spin density (i.e. – subtracting the phase terms) of two gradient echo images acquired with different TE with all other imaging parameters held constant, followed by calculating the image phase. However, as demonstrated in Figure 5-2, gradient echo images suffer from signal intensity distortions, in addition to geometric distortions in the frequency encoding direction, leading to unreliable phase data, and concomitantly unreliable  $\Delta B(x,y)$ , near the surface of the object.

A better approach would be to employ a spin echo imaging sequence with the addition of a delay inserted between the  $\pi/2$  and  $\pi$  RF pulses while keeping all other pulse sequence timings constant (Koch et al., 2006). The asymmetry of the  $\pi/2$  and  $\pi$  RF pulses leads to a phase dispersion term that affects the image phase similarly to gradient echo imaging. However, the signal intensity distortions in an asymmetric spin echo image can be minimized by using a short free-precession delay ( $T_{fp}$ ). The spatially-dependent phase of an MR image acquired with an asymmetric spin echo sequence can be described as

$$\varphi(x, y) = -2\gamma\Delta B(x, y)T_{fp} + \varphi_0(x, y), \quad (5-8)$$

where  $\varphi$  is the spatially-dependent phase,  $\gamma$  is the gyromagnetic ratio,  $\Delta B$  is the spatially-dependent perturbation of the external magnetic field,  $T_{fp}$  is the free-precession delay and  $\varphi_0$  is a spatially-dependent phase offset term. The phase offset term in Equation 5-8 can be eliminated by dividing the complex form of the Fourier transform-derived image spin density of two asymmetric spin echo data sets with different  $T_{fp}$ , such that

$$\varphi_{CD}(x, y, \Delta T_{fp}) = -2\gamma\Delta B(x, y)(T_{fp,i} - T_{fp,0}) = -2\gamma\Delta B(x, y)\Delta T_{fp} \quad (5-9)$$

The resulting phase of the complex-divided image,  $\varphi_{CD}$ , is a function of the difference in  $T_{fp}$  of the two data sets and linearly dependent on the magnetic field perturbation.

## 5.3 Methods

### 5.3.1 Preparation of Cu-Sn Alloys

Copper (Cu) and tin (Sn) form a binary alloy with several peritectic reactions and intermediate phases, in which Cu forms a solid solution up with up to 9 atomic percent (at.%) (15.8 wt%) Sn at 520 °C (Saunders and Miodownik, 1990). Pure Cu (99.9% minimum purity shot, 1-10 mm diameter, Alfa Aesar<sup>®</sup>, Ward Hill, MA, USA) and Sn (99.8% minimum purity shot, 8-20 mesh, Alfa Aesar<sup>®</sup>, Ward Hill, MA, USA) were mixed to create four samples consisting of 1.5%, 3.0%, 5.1% and 7.0% Sn in atomic percent.

Each of the four samples was melted in a graphite crucible coated with boron nitride in open air at 1175 °C until a liquid solution was formed. The molten solutions were poured into sand molds in the shape of a 5 mm diameter cylinder and allowed to air-cool. Each sample was homogenized for 24 hours at 500 °C, air-cooled, solutionized at 800 °C for 24 hours, and subsequently water quenched to maintain the solid solution microstructure. After quenching, the Cu-Sn binary 5 mm cylindrical alloy samples were sanded with 150-grit, 200-grit, then 300-grit sandpaper to remove surface oxides and residue deposited during the casting process. The cylindrical samples (~4 mm diameter) were then cut to a length of approximately 2 cm for subsequent testing.

The composition of the Cu-Sn alloys was tested in a Perkin-Elmer Optima<sup>®</sup> 3200 RL inductively coupled plasma atomic emission spectrometer (ICP-AES) configured for aqueous analysis. Elemental standards for both Cu and Sn were prepared at

concentrations of 100 ppm, 10 ppm, and 1 ppm by diluting a stock standard solution (1000 ppm of solute in nitric acid, Ricca Chemical Company<sup>®</sup>, Arlington, TX, USA) with purified water. An aqueous sample of each Cu-Sn alloy was prepared dissolving a piece in a 1:1:4 solution of nitric acid, hydrochloric acid, and purified water, and then diluting the sample to between 10-40 ppm by weight.

### **5.3.2 SQUID Magnetometry**

Prior to measurement of the Cu-Sn alloy samples, the SQUID magnetometer was calibrated with a palladium (Pd) reference standard supplied by the manufacturer and results were compared to literature values of Pd susceptibility. Additionally, the Cu-Sn alloy samples were formed with a standard length and diameter to avoid the need to apply geometric corrections to the magnetization measurements. Cylindrical samples, 3 mm in length, were cut from each of the four Cu-Sn alloys described in the preceding subsection and cleaned with isopropyl alcohol. The samples were then individually loaded into the SQUID magnetometer (Magnet Property Measurement System XL<sup>®</sup>, Quantum Design<sup>®</sup>, Inc., San Diego, CA, USA) with a temperature range of 2-310 K and magnetic fields reaching 7 T. The samples were mounted in plastic straws using a piece of tape to immobilize them during measurement. The small background magnetic moment of the tape was measured and subtracted to obtain the magnetic moment for the samples only. The magnetization of each sample was studied at 300 K in a varying field ranging from 0 T to 7 T. A hysteresis plot of magnetization,  $M$ , versus applied field,  $H$ , was made for each sample and linear regression was used to extract the mass susceptibility from the plots. The analysis only included the response at high fields,  $5 \text{ T} \leq H \leq 7 \text{ T}$  because diamagnetic and/or paramagnetic responses are dominant and any trace ferromagnetic contributions are negligible within this range.

The dimensionless volume susceptibility of each sample was obtained by multiplying the measured mass susceptibility by the density of the sample. Irregularity in the geometry of the samples made accurate volumetric measurement difficult. Consequently, the density of each sample was estimated from the atomic percentage of tin determined from ICP-AES measurements. The density of each sample was estimated using a weighted average of the density of Cu and Sn where the weight is equal to the atomic fraction of each component in the alloy.

In addition to measurements of Cu-Sn alloy susceptibility, the susceptibility of distilled and deionized water used for MR measurements was measured. The distilled water was obtained from the McKnight Brain Institute and deionized using a PURELAB Ultra<sup>®</sup> water purification system (PURELAB Ultra<sup>®</sup>, Elga LLC, Woodridge, Illinois, USA). The water purification system produces type 1+ (trace metal detection grade) and type 1 (HPLC grade) water. A plastic can was weighed, loaded with distilled and deionized water and weighed again and then loaded into the SQUID magnetometer by mounting it in a plastic straw in a similar manner to that used for the Cu-Sn alloy susceptibility measurements. The magnetization of the sample was studied at 300 K in a varying field ranging from 5 T to 7 T. A hysteresis plot of magnetization,  $M$ , versus applied field,  $H$ , was made for each sample and linear regression was used to extract the mass susceptibility from the plots. To account for evaporation during the measurement, the average weight of the sample before and after the measurement was used to calculate the mass susceptibility. The volume susceptibility was calculated by multiplying the mass susceptibility by the density of pure water at room temperature.

### 5.3.3 MR Imaging

MR images were used to map the perturbations in the external magnetic field around the sample metals. A sample holder was fabricated using a 50 mL test tube and nylon collar with a threaded hole (Figure 5-3) to secure the Cu-Sn alloy samples during MR imaging. Prior to imaging, the sample was secured in the nylon collar using a nylon screw and the 50 mL test tube was filled with distilled and deionized water. The cap of the test tube was wrapped with thread seal tape to ensure an air tight seal. The sample was then centered in a birdcage transmit and receive volume coil, and centered in the bore of the 4.7 or 11.1 T magnet.

MR imaging was performed using Agilent<sup>®</sup> imaging consoles (Agilent<sup>®</sup> Technologies, Inc., Santa Clara, CA, USA) connected to a 4.7 T horizontal bore magnet and Magnex Scientific<sup>®</sup> 11.1 T horizontal bore magnet (Agilent<sup>®</sup> Technologies, Inc., Santa Clara, CA, USA). Field perturbation measurements were conducted on all four Cu-Sn alloy samples at 4.7 T and two of the samples (3.0% and 5.1% Sn) at 11.1 T. The purpose of measurements at 11.1 T was to evaluate the consistency of the proposed method at more than one field strength. In an effort to minimize the contribution of magnetic field perturbations due to sources other than the sample metals, manual global shimming using first and second order shims was conducted on the sample holder containing only distilled and deionized water. Shim settings from the manual shimming resulted in linewidths of approximately 10 Hz at 4.7 T and 14 Hz at 11.1 T and were applied during field mapping measurements. A spin echo sequence with an echo-offset free precession delay was utilized for mapping the field perturbations around sample metals (Koch et al., 2006). This asymmetric spin echo sequence consists of a standard spin echo sequence with the addition of a variable

delay inserted between the 90° and 180° RF pulses while keeping all other pulse sequence timings constant. Free precession delays ( $T_{fp}$ ) ranged from 0 ms to 1 ms for measurements performed at 4.7 T and from 0 ms to 0.75 ms at 11.1 T with at least 6  $T_{fp}$ 's collected for each Cu-Sn alloy sample. Other imaging parameters include: TR = 3000 ms, TE = 30 ms, NA = 1, bandwidth = 55 kHz, FOV = 3 × 3 cm<sup>2</sup>, 128 × 128 matrix with 5 slices of 1 mm thickness with a 1 mm gap.

### 5.3.4 Mapping B Field Perturbations

The magnetic field perturbation maps around each metal were determined first by complex dividing each non-zero  $T_{fp}$  data set by the 0 ms delay data set and calculating the phase angle by evaluating the four-quadrant inverse tangent function for the ratio of the imaginary to the real part of the resultant complex divided images as shown in Equation 5-9. For the four-quadrant inverse tangent operation, all values of phase are mapped within the range of  $(-\pi, \pi]$ . Consequently, values of  $|\varphi_{CD}| > \pi$  will be mapped within  $(-\pi, \pi]$  and result in phase-aliasing as well as inaccurate calculation of  $\Delta B$ . Phase aliasing can occur when  $\Delta T_{fp}$  is too large for a given  $\Delta B$ , as shown in Figure 5-4. Although phase aliasing can be removed using several phase-unwrapping methods (Bagher-Ebadian et al., 2008; Bakker et al., 2008); here data sets exhibiting phase aliasing were removed from the analysis to avoid possible error introduced by phase unwrapping algorithms. MR-derived field perturbation maps,  $\Delta B_{MR}$ , were calculated by using linear regression on the  $\varphi_{CD}$  vs.  $\Delta T_{fp}$  data (Equation 5-9) on a voxel-by-voxel basis. Residual background inhomogeneities, which were minimized by shimming, are spatially slowly varying and were assumed to be linear within the imaging FOV. Therefore, a correction for these linearly varying background fields was applied in the read and phase encoding directions.

### 5.3.5 Estimating Magnetic Susceptibility

Figure 5-5 summarizes the method of estimating the volume susceptibility of the Cu-Sn alloy using  $\Delta B_{MR}$ . External field perturbations around the Cu-Sn alloys were simulated using a Fourier-based method proposed by Marques and Bowtell (Marques and Bowtell, 2005). For simulation of the field perturbation maps around the Cu-Sn alloys, a micrometer was used to measure the outer diameter of each cylindrical sample. Next, a circular region of interest (ROI) was drawn centered about the origin of the metal cylinder in the MR images. The origin of the metal cylinder was determined by the symmetry in  $\Delta B_{MR}$  (Cheng et al., 2007). The volume susceptibility of the surrounding media (i.e. – distilled and deionized water) measured in this study,  $\chi_{v,media} = -8.90$  ppm, was then assigned to voxels outside of the circular ROI. The measured value of water susceptibility differs by 1.7% from previously reported values ( $\chi_{v,media} = -9.05$  ppm) (Schenck, 1996). The object susceptibility,  $\chi_{v,obj}$ , was given an initial range and step size and assigned to voxels inside of the circular ROI to generate field perturbation maps as a function of object susceptibility.  $\Delta B_{MR}$  were compared to simulated field perturbation maps,  $\Delta B_{Sim}$ , by computing an  $r^2$  value for either; 1) a line profile in the phase encoding direction bisecting the metal or 2) a 64 x 64 window of the 2D field map centered on the metal. The magnetic susceptibility of each Cu-Sn alloy was estimated by maximizing the  $r^2$  value between  $\Delta B_{MR}$  and  $\Delta B_{Sim}$ .

### 5.3.6 Data Analysis

The volume susceptibility,  $\chi_{v,obj}$ , of each Cu-Sn alloy was estimated using  $\Delta B_{MR}$  from four imaging slices at 4.7 T. The estimation was repeated at 11.1 T for samples containing 5.1% and 7.0% Sn. The influence of image resolution relative to object size on accurately estimating  $\chi_{v,obj}$  was investigated by downsampling  $\Delta B_{MR}$  to matrix sizes

of 64 x 64, 32 x 32, and 16 x 16 and repeating the  $\chi_{v,obj}$  estimation for all Cu-Sn alloy samples at 4.7 T. Sensitivity of the proposed method of estimating  $\chi_{v,obj}$  to geometric positioning and size was evaluated using data collected for the 5.1% Sn sample at 11.1 T. The importance of accurate geometry positioning for calculation of  $\Delta B_{Sim}$  was investigated by shifting the circular ROI a) up b) down c) left and d) right 32, 16 and 8 pixels relative to the center of the metal and estimating  $\chi_{v,obj}$ . Additionally, the importance of accurately representing the object size when calculating  $\Delta B_{Sim}$  was assessed by estimating  $\chi_{v,obj}$  when the circular ROI were drawn 30, 20, 15, 10 and 5% smaller and larger than the actual object OD.

## 5.4 Results

### 5.4.1 Cu-Sn Alloys

The Cu-Sn alloy casting process resulted in four cylindrical samples nominally consisting of 1.5%, 3.0%, 5.1% and 7.0% Sn (at. %) with measured outer diameters of 4.1 mm, 3.8 mm, 4.6 mm and 4.5 mm, respectively. The sanding process, applied to remove deposits and imperfections from alloy casting, caused the variation of the outer diameters. ICP-AES was used to determine the actual atomic percent composition of each alloy and percentages of 1.36%, 2.57%, 4.98% and 6.93% Sn were measured for alloys with a nominal atomic percentage of 1.5%, 3.0%, 5.1% and 7.0% Sn. The ICP-AES results indicate that the actual alloy at. % compositions varied by no more than 15% of the desired composition.

### 5.4.2 Mapping B Field Perturbations

Magnetic field perturbation maps,  $\Delta B_{MR}$ , were calculated for all alloys at 4.7 T (Figure 5-6, top row) and for 3.0% and 5.1% (at. %) Sn alloys at 11.1 T (Figure 5-7, top row). The top row of Figure 5-6 shows  $\Delta B_{MR}$  measured at 4.7 T for all four alloys with

unreliable phase regions (i.e. – noise within the position of the alloy) masked for clarity. The bottom row of Figure 5-6 indicates the coefficient of determination,  $r^2$ , of the linear regression performed on  $\phi_{CD}(\Delta T_{fp})$  data (Equation 5-9) on a voxel-by-voxel basis to determine  $\Delta B_{MR}$ . As expected,  $|\Delta B_{MR}|$  is highest near the surface of the metal and then diminishes as the distance from the metal increases. Similarly,  $r^2$  values are greater than 0.9 for distances less than 4 mm from the surface of the alloys. As  $|\Delta B_{MR}|$  decreases towards the background noise value, the relative contribution of noise to  $\phi_{CD}(\Delta T_{fp})$  increases leading to smaller  $r^2$  values. Because the uncertainty in calculating  $\Delta B_{MR}$  from  $\phi_{CD}(\Delta T_{fp})$  increases with distance from the surface of the metal, a 64 x 64 sub-window of  $\Delta B_{MR}$  (dashed box in Figure 5-6) was used for  $\chi_{v,obj}$  estimations. The range of  $\Delta B_{MR}$  for each Cu-Sn alloy sample was -3.0  $\mu T$  to 4.1  $\mu T$  (1.5 % Sn), -4.4  $\mu T$  to 4.8  $\mu T$  (3.0% Sn), -7.5  $\mu T$  to 8.6  $\mu T$  (5.1% Sn) and -8.9  $\mu T$  to 10.3  $\mu T$  (7.0% Sn). Therefore, the magnitude of  $\Delta B_{MR}$  was observed to increase with increasing Sn content.

Magnetic field perturbation maps collected at 4.7 T and 11.1 T, for 3.0% and 5.1% Sn samples, were compared to evaluate the utility of this field mapping method at high field. To compare the results at two field strengths,  $\Delta B_{MR}$  was normalized by the field strength at which the data was acquired (Figure 5-7, top row). It would be expected that normalized magnetic field perturbation maps ( $\Delta B_{MR}/B_0$ ) acquired at 4.7 T or 11.1 T would be equivalent because the magnetic field perturbations scale linearly with external field strength. For the 3.0% Sn alloy,  $\Delta B_{MR}/B_0$  collected at 4.7 T and 11.1 T have an  $r^2$  value of 0.83 for a 64 x 64 window centered about the metal. An  $r^2$  value of 0.93 was calculated when comparing  $\Delta B_{MR}/B_0$  for the 5.1% Sn alloy. In both cases, the  $r^2$  value was calculated by neglecting masked voxels. Qualitatively,  $\Delta B_{MR}/B_0$  of the

same alloy (3.0% Sn: Figure 5-7, top left; 5.1% Sn: Figure 5-6, top right) appear similar with the most obvious difference being the increased geometric distortion in the readout direction (left to right) at 11.1 T. Additionally, the magnitude of  $\Delta B_{MR}/B_0$  is greater for the 5.1% Sn alloy. Line profiles of  $\Delta B_{MR}/B_0$  are compared in the bottom row of Figure 5-7 along the phase encoding direction (to avoid mismatch due to increased geometric distortion at 11.1 T), centered on the metal (dashed lines in the top row of Figure 5-7). An  $r^2$  value of 0.90 was calculated when comparing line profiles of 3.0% Sn  $\Delta B_{MR}/B_0$  data while 5.1% Sn line profiles exhibited an  $r^2$  value of 0.97. Overall, good agreement was observed when comparing  $\Delta B_{MR}/B_0$  collected at 4.7 and 11.1 T.

#### 5.4.3 Estimating Magnetic Susceptibility

As summarized in Figure 5-5, magnetic field perturbation maps collected at 4.7 T and 11.1 T were used to estimate  $\chi_{V,obj}$  of the metal alloys relative to  $\chi_{V,media} = -8.90$  ppm, the volume susceptibility of distilled and deionized water determined from SQUID magnetometry. Estimations of  $\chi_{V,obj}$  were produced by maximizing agreement ( $r^2$  value) between  $\Delta B_{z,MR}$  and  $\Delta B_{z,Sim}$ , where  $\Delta B_{z,Sim}$  was generated by iterating through values of  $\chi_{V,obj}$ . Two methods were used to compute  $r^2$ : 1) values of  $\Delta B_{z,MR}$  and  $\Delta B_{z,Sim}$  were compared from a  $64 \times 64$  window centered about the cylinder (image fit). 2) Taking advantage of the rotational symmetry of the object, values were compared from a line profile bisecting the cylinder in the phase encoding direction (line fit). Tables 5-1 and 5-2 summarize the  $\chi_{V,obj}$  measured by SQUID magnetometry and estimated by the method outlined in this study for each of the Cu-Sn alloys. Values of  $\chi_{V,obj} = -10.4, -11.04, -12.7$  and  $-13.97$  ppm were measured using SQUID magnetometry for the 1.5%, 3.0%, 5.1% and 7.0% (at. %) Sn samples, respectively. Using  $\Delta B_{z,MR}$  acquired at 4.7 T, the image fit method of estimating  $\chi_{V,obj}$  resulted in values of (mean  $\pm$  standard deviation):  $-10.28 \pm$

0.03 ppm (1.5% Sn),  $-10.99 \pm 0.14$  ppm (3.0% Sn),  $-12.47 \pm 0.03$  ppm (5.1% Sn) and  $-14.03 \pm 0.09$  ppm (7.0% Sn). The largest deviation between  $\chi_{V,obj}$  measured by SQUID magnetometry and estimated by MR was 1.8% (5.1% Sn sample). Estimations  $\chi_{V,obj}$  of derived from a line fit resulted in values of (mean  $\pm$  standard deviation):  $-10.21 \pm 0.06$  ppm (1.5% Sn),  $-10.84 \pm 0.15$  ppm (3.0% Sn),  $-12.44 \pm 0.12$  ppm (5.1% Sn) and  $-13.88 \pm 0.22$  ppm (7.0% Sn) with the largest deviation between measured and estimated  $\chi_{V,obj}$  being 2.2% (5.1% Sn sample). Image and Line fits were also performed to estimate  $\chi_{V,obj}$  using  $\Delta B_{z,MR}$  data acquired at 11.1 T for 3.0% and 5.1% Sn samples. Image fits resulted in  $\chi_{V,obj}$  estimates of  $-10.90 \pm 0.18$  ppm and  $-12.31 \pm 0.03$  ppm for 3.0% and 5.1% Sn samples, respectively, with a maximum deviation of 0.6% from the SQUID magnetometry measured value of  $\chi_{V,obj}$  (5.1% Sn sample). Values of  $-11.08 \pm 0.12$  ppm (3.0% Sn) and  $-12.31 \pm 0.03$  ppm (5.1% Sn) were estimated for  $\chi_{V,obj}$  using the line fit method. The volume susceptibility of the Cu-Sn alloys, measured using SQUID magnetometry and the MR method outlined in this chapter, were plotted as a function of atomic percent Sn (Figure 5-8). Linear regression was performed to determine the relationship between Sn content and volume susceptibility resulting in a slope of  $-0.68 \pm 0.04$  ppm and y-intercept of  $-9.2 \pm 0.19$  ppm for SQUID measurements and slope of  $-0.66 \pm 0.03$  ppm and y-intercept of  $-9.1 \pm 0.11$  ppm for MR measurements. The y-intercept determined by both measurements indicates a pure Cu susceptibility of  $-0.1$  to  $-9.2$  ppm which is similar to the reported value of  $-9.32$  ppm for 99.999% pure Cu (Bowers, 1956).

Figure 5-9 demonstrates the similarity between  $\Delta B_{z,MR}$  (top row) and  $\Delta B_{z,Sim}$  (second row), where  $\Delta B_{z,Sim}$  was derived using estimates of  $\chi_{V,obj}$  obtained from the

image fit method at 4.7 T. Difference maps ( $\Delta B_{z,MR} - \Delta B_{z,Sim}$ ) show that the largest disagreement between the model and measurement occurs near the surface of the cylinders (Figure 5-8, third row). Differences between the measurement and simulation range from -1.3  $\mu$ T to 1.6  $\mu$ T for the 1.5% Sn sample, -1.0  $\mu$ T to 2.3  $\mu$ T for the 3.0% Sn sample, -2.4  $\mu$ T to 2.9  $\mu$ T for the 5.1% Sn sample and -2.0  $\mu$ T to 3.0  $\mu$ T for the 7.0% Sn sample. Line profiles of  $\Delta B_{z,Sim}$ , derived using estimates of  $\chi_{v,obj}$  obtained from the line fit method at 4.7 T, showed good agreement with line profiles plotted of  $\Delta B_{z,MR}$  for the 3.0% and 7.0% Sn samples (Figure 5-9, bottom row). Comparison of  $\Delta B_{z,MR}$  and  $\Delta B_{z,Sim}$  was also performed for  $\Delta B_{z,Sim}$  derived using estimates of  $\chi_{v,obj}$  obtained from the image fit method at 11.1 T (Figure 5-9, top row). The issue of geometric distortion is more evident at 11.1 T as the MR-derived mask does not conceal the model geometry in  $\Delta B_{z,Sim}$  (Figure 5-10, top right). Field perturbations of  $\sim 10$  ppm were observed for the 3.0% Sn sample whereas perturbations of  $\sim 16$  ppm were observed for the 5.1% Sn sample. Under the imaging protocol employed in this study (readout gradient strength =  $3.9 \times 10^{-4}$  T/cm), shifts of 1 and 2 voxels could be expected near the surface of the 5.1% and 7.0% Sn metals, respectively. Line profiles of  $\Delta B_{z,Sim}$ , derived using estimates of  $\chi_{v,obj}$  obtained from the line fit method at 11.1 T, showed good agreement with line profiles plotted of  $\Delta B_{z,MR}$  for the 3.0% and 5.1% Sn samples (Figure 5-10, bottom row).

Image fit and line fit estimations of  $\chi_{v,obj}$  were performed for data collected at an in-plane resolution of  $234 \times 234 \mu\text{m}^2$ . Estimations of  $\chi_{v,obj}$  were also performed after downsampling the k-space data to result in imaging resolutions of  $468 \times 468 \mu\text{m}^2$ ,  $936 \times 936 \mu\text{m}^2$  and  $1872 \times 1872 \mu\text{m}^2$  and executing the image fit and line fit procedure on a single slice. Downsampling the k-space data allows for analysis of resolution effects on

$\chi_{v,obj}$  estimation while keeping SNR constant and the results of this analysis are summarized in Figure 5-11 and in Tables 5-3 and 5-4. Estimations of  $\chi_{v,obj}$  for the 1.5% and 3.0% samples were least affected by the decreased resolution with  $\chi_{v,obj}$  equal to -10.05 ppm (line fit) and -10.13 ppm (image fit) for the 1.5% Sn sample and -11.147 ppm (line fit) and -10.691 ppm (image fit) for the 3.0% Sn sample at a resolution of  $1.88 \times 1.88 \text{ mm}^2$ . The difference between measured  $\chi_{v,obj}$  and estimated  $\chi_{v,obj}$  (percent error) grew to more than 20% for the 5.1% Sn sample at the same resolution. The percent error of the 7.0% Sn  $\chi_{v,obj}$  estimation grew from 0.4% (image fit) and 0.7% (line fit) at native resolution to 10% (image fit) and 15% (line fit) at a resolution of  $936 \times 936 \text{ }\mu\text{m}^2$ . In addition to analysis on image resolution, the impact of model geometry (cylinder diameter and position) on  $\chi_{v,obj}$  estimation was also evaluated (Figure 5-12) for a single Cu-Sn alloy (3.0% Sn). A difference in cylinder diameter of  $\pm 5\%$  did not significantly affect the estimation of  $\chi_{v,obj}$  with the percent error only increasing by 1-2%. With the cylinder size increasing to 130% of the actual value, the percent error rose to 10%. Conversely, a percent error of 16% was found for a cylinder diameter of 70% of the actual value. Incorrect positioning of the cylinder by 2 voxels resulted in little change in the estimation of  $\chi_{v,obj}$ . However, displacing the cylinder by 8 voxels ( $\sim 50\%$  of the alloy diameter) resulted in up to 11% error using the image fit method and 26% error using the line fit method.

## 5.5 Discussion

An alternative method of estimating the relative magnetic susceptibility of objects with constant cross-sectional profiles has been presented. This method is not restricted to geometries for which an analytical solution to the susceptibility-induced magnetic field perturbations is known. This restriction is lifted because measured magnetic field

perturbation maps are compared to those simulated using a rapid, Fourier-based, method of modeling the approximated dipole field for arbitrary geometries. The method was evaluated by measuring the magnetic susceptibility of four Cu-Sn alloys relative to distilled and deionized water and then comparing these values to those determined using SQUID magnetometry. Furthermore, this method was tested at two field strengths, 4.7 T and 11.1 T, and a sensitivity analysis was performed to determine the impact of image resolution and model geometry on relative susceptibility estimations.

With this method, accurate measurement of  $\Delta B_{z,MR}$  is critical for estimating  $\chi_{v,obj}$  as a direct comparison between  $\Delta B_{z,MR}$  and  $\Delta B_{z,Sim}$  is used to calculate  $\chi_{v,obj}$ . Therefore, we employed an asymmetric spin echo sequence, as opposed to a gradient echo sequence, for measurement of  $\Delta B_{z,MR}$ . Recall from Section 2.3.2 that gradient echo images are susceptible to signal intensity distortions, in addition to geometric distortions, that are caused by intravoxel dephasing occurring during the time to echo. The signal intensity distortions are correlated with the intensity of magnetic field gradients and are therefore most severe at susceptibility boundaries. Due to hardware and imaging protocol limitations, gradient echo sequences will have a fixed minimum TE (~ 5 to 10 ms using the imaging parameters in this study). Although  $\Delta TE$  can be kept small to alleviate the issue of phase aliasing, gradient echo images will typically contain a greater amount of signal intensity distortion than asymmetric spin echo sequences due to the fact that intravoxel dephasing is limited to  $T_{fp}$  in asymmetric spin echo sequences (values used in this study: 0.0 to 1.0 ms at 4.7 T, 0.0 to 0.75 ms at 11.1 T). Signal intensity distortions can confound  $\chi_{v,obj}$  estimations because they result in unreliable phase data near the surface of the metal. The metal/water interface

constitutes the region of greatest magnetic field perturbations which then fall off rapidly with distance from the interface. The difference in  $\Delta B_{z,MR}$  between different Cu-Sn compositions is greatest near the metal, therefore, voxels containing field perturbation information near the surface of the metal are important for resolving  $\chi_{v,obj}$  differences between similar materials.

As is evident in Figures 5-6 (top row) and Figure 5-7 (top row), signal intensity distortions did not impact  $\Delta B_{z,MR}$  when employing an asymmetric spin echo sequence at 4.7 T or 11.1 T. Geometric distortions were observed for the 5.1% and 7.0% Sn samples at 4.7 T and both samples studied at 11.1 T (3.0% and 5.1% Sn). Because the susceptibility mismatch increased with Sn content, the 5.1% Sn sampled measured at 11.1 T exhibited the largest geometric distortion. The normalized field maps agreed well (Figure 5-7) indicated the proposed method of measuring  $\Delta B_{z,MR}$  was suitable for both field strengths. Voxel-by-voxel linear regression was used to calculate  $\Delta B_{z,MR}$  from phase data collected at multiple  $T_{fp}$  and resulted in  $r^2$  values  $> 0.9$  near the surface of the metal. The  $r^2$  values then decreased with distance from the metal surface as  $\Delta B_{z,MR}$  decreased. High  $r^2$  values can also be seen far from the surface of the 1.5% and 3.0% Sn metals measured at 4.7 T due to the presence of background gradients caused by objects other than the Cu-Sn alloy. Larger  $T_{fp}$  were used for the 1.5% and 3.0% Sn samples making  $\Delta B_{z,MR}$  more sensitive to the low amplitude background gradients which are above the level of noise but not significant enough to affect  $\Delta B_{z,MR}$  (Figure 5-6 and 5-7, top rows). Image fitting for  $\chi_{v,obj}$  was performed on a  $64 \times 64$  sub-window of the data centered about the metal cylinder. The sub-window was chosen to limit the fit to  $\Delta B_{z,MR}$  measured with a high  $r^2$  value.

Measurements of  $\chi_{v,obj}$  at 4.7 T and 11.1 T agreed well with SQUID magnetometry measurements of the Cu-Sn alloy samples when using either line fitting (Table 5-1) or image fitting (Table 5-2) methods. MR-derived values of  $\chi_{v,obj}$  deviated from SQUID magnetometry measurements by 0.36% to 3.08% using the image fitting method and 0.38% to 3.10% using the line fitting method. The agreement between SQUID magnetometry and MR-derived values of  $\chi_{v,obj}$  is encouraging. SQUID magnetometer  $\chi_{v,obj}$  measurements had a standard deviation ranging from 0.02 to 0.04 ppm after propagating error from each step in the measurement including the Cu-Sn alloy density estimation. MR-derived values of  $\chi_{v,obj}$  had a standard deviation ranging from 0.06 ppm to 0.22 ppm and 0.03 to 0.14 ppm for line fit and image fit estimations, respectively, at 4.7 T. At 11.1 T, the standard deviation of the line fit result ranged from 0.03 ppm to 0.14 ppm and the standard deviation of the image fit result ranged from 0.03 ppm to 0.18 ppm.

The analysis of image resolution effects on  $\chi_{v,obj}$  estimation using the MR method indicate that at low resolution, the percent difference between MR derived values of  $\chi_{v,obj}$  and SQUID magnetometry values increased with Sn content (Figure 5-11, Tables 5-3 and 5-4). As the difference between alloy susceptibility and water susceptibility increased, the resolution of  $\Delta B_{z,MR}$  had a larger impact on  $\chi_{v,obj}$  estimations. Presumably, this behavior is due to the magnetic field gradient created at the alloy-water boundary as this gradient will increase as the susceptibility mismatch between the alloy and surrounding media increases (Figure 5-13). The lower resolution of  $\Delta B_{z,MR}$  is unable to capture the abrupt changes in the magnetic field gradient and the apparent gradient is reduced. This results in an underestimation of  $\chi_{v,obj}$  as shown in Figure 5-10. Therefore,

the appropriate imaging resolution for estimating  $\chi_{v,obj}$  using this MR method will depend on the susceptibility mismatch between the metal and surrounding media.

Sources of error in the MR derivation of  $\chi_{v,obj}$  include noise in the phase measurements, variability in  $\Delta B_{z,MR}$  from the linear regression, incorrect placement of the object geometry for simulations and limitations of the discrete Fourier transform method of modeling the magnetic field perturbations. Under our proposed method,  $\chi_{v,obj}$  is derived from comparison of  $\Delta B_{z,MR}$  and  $\Delta B_{z,Sim}(\chi_{v,obj})$  with the relationship between  $\Delta B_{z,Sim}$  and  $\chi_{v,obj}$  being inexplicit, or the result of a simulation. Therefore, an analytical expression cannot be derived for the effect of error propagation on  $\chi_{v,obj}$  estimations. In order to gauge the contribution of uncertainty in  $\Delta B_{z,MR}$  on susceptibility estimations,  $\chi_{v,obj}$  was estimated from a set of 100  $\Delta B_{z,MR}$  where each voxel was a random sample from a normal distribution with a mean equal to the  $\Delta B_{z,MR}$  (linear regression slope estimator) and standard deviation equal to the standard deviation of  $\Delta B_{z,MR}$ . The standard deviations of these estimations of  $\chi_{v,obj}$  were on the order of 0.01 ppm suggesting that error in the simulation geometry may be a significant source of the uncertainty in  $\chi_{v,obj}$ . Sensitivity of  $\chi_{v,obj}$  to improper simulation of the object geometry was evaluated by estimating  $\chi_{v,obj}$  as a function of object position (Figure 5-12A) and object size (Figure 5-12B) for the 3.0% Sn sample. The line fit method of estimating  $\chi_{v,obj}$  was most sensitive to improper positioning of the object in the read encoding direction due to the fact that the apparent diameter of the cylinder is reduced in the phase encoding direction leading to an overestimation of  $\chi_{v,obj}$  by up to 26%. Although the image fit method was less sensitive to improper positioning, displacing the object by nearly 50% of the object's diameter resulted in a 11% difference (1.25 ppm) between MR-derived

$\chi_{v,obj}$  and SQUID magnetometry measurements. Correct placement of the model geometry with an improper diameter resulted in error that affected both the image fit and line fit methods of estimations in the same manner (Figure 5-12B). Using an object diameter that was smaller than the actual diameter resulted in an overestimation of  $\chi_{v,obj}$  whereas a larger object diameter resulted in an underestimation of  $\chi_{v,obj}$ . Modeling the object with a diameter within  $\pm 5\%$  of the actual diameter resulted in a shift in the estimated  $\chi_{v,obj}$  by 0.2 ppm. The Fourier-based method of calculating  $\Delta B_{z,Sim}$  has been shown to be highly accurate with an average deviation of 0.5 % from analytical solutions to  $\Delta B_z$  (Marques and Bowtell, 2005). The highest deviations occur at susceptibility boundaries and can be attributed to artifacts of the Fourier transform (Koch et al., 2006). Fourier transform artifacts in  $\Delta B_{z,Sim}$  are minimized by including adequate spatial padding between the object of interest and the edge of the model as well as using a sufficient model resolution (Koch et al., 2006).

## 5.6 Conclusions

An MR method for measuring the magnetic susceptibility of objects with a constant cross-sectional profile is presented in this study. This method was applied to solid solution alloys of Cu and Sn demonstrating that the magnetic susceptibility of an alloy can be modulated by altering the volume fraction of component metals. Measured values of magnetic susceptibility for Cu-Sn alloys of four different atomic percent compositions of Sn deviated by less than 3% from SQUID magnetometry measurements. This method could be utilized in the future development of alloys that are susceptibility-matched to host materials to reduce or eliminate susceptibility artifact in MR images.

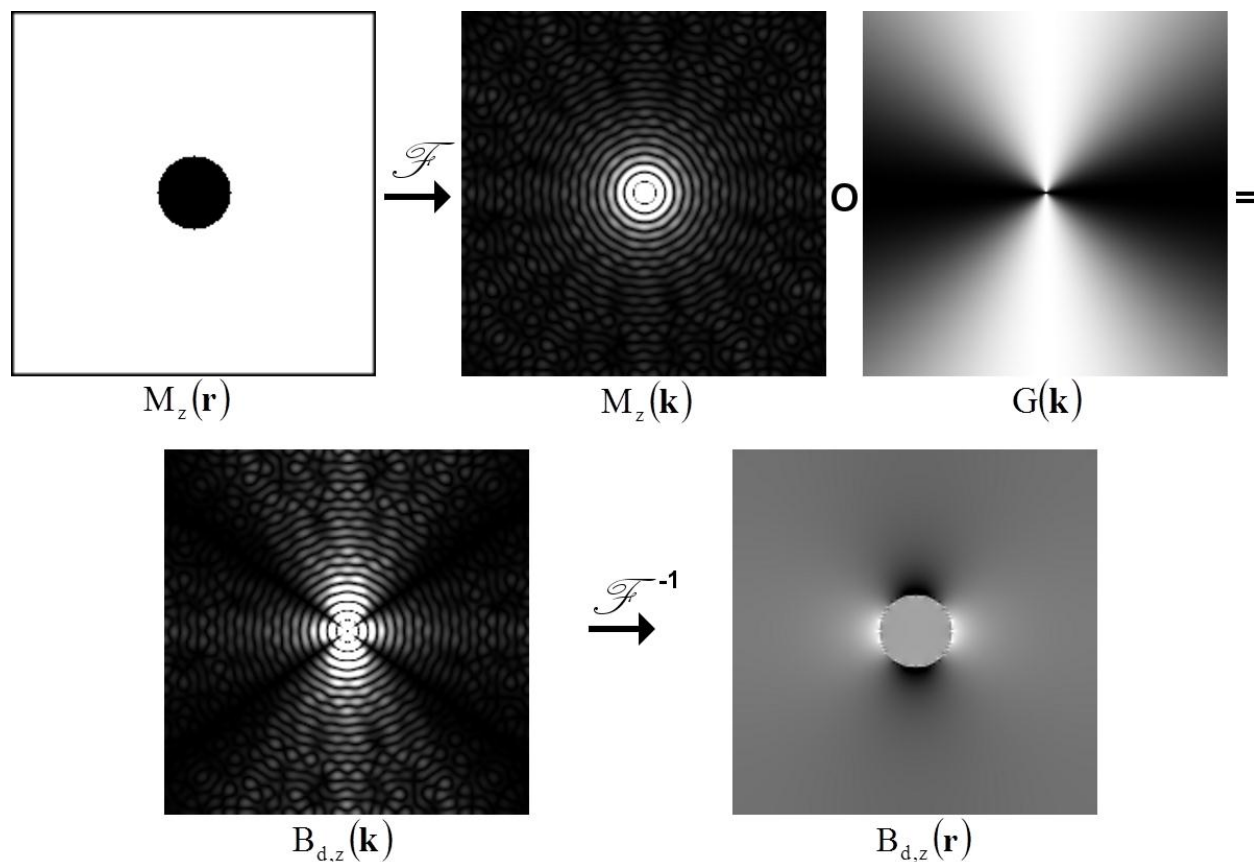


Figure 5-1. Pictorial summary of Equations 5-5 and 5-6 which are used to simulate magnetic field perturbations based on an arbitrary susceptibility distribution. The magnetization distribution in real space (Equation 5-3),  $M_z(\mathbf{r})$ , is Fourier transformed into k-space. The dipole-approximated magnetic field perturbations in k-space,  $B_{d,z}(\mathbf{k})$ , is the product of the entrywise multiplication (indicated by  $\circ$ ) between  $M_z(\mathbf{k})$  and  $G(\mathbf{k})$ , the parenthetical term in Equation 5-5. The magnetic field perturbations in real space,  $B_{d,z}(\mathbf{r})$ , are calculated by performing an inverse Fourier transform on  $B_{d,z}(\mathbf{k})$ .

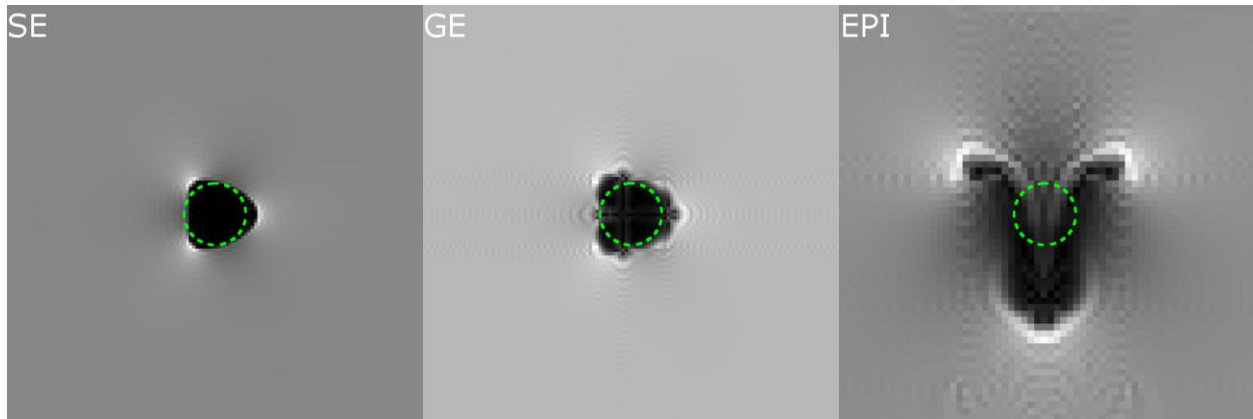


Figure 5-2. Simulated magnitude images of a cylindrical object ( $\chi_{v,obj} = -14$  ppm) immersed in water ( $\chi_{v,media} = -9.05$  ppm) acquired with a spin echo (SE), gradient echo (GE), and echo planar (EPI) imaging sequence at 11.1 T. The dashed line indicates the actual outer diameter of the cylindrical object. SE and GE images were simulated with a 3 × 3 cm FOV, 128 × 128 matrix, 50 kHz bandwidth, phase encoding gradient duration of 544  $\mu$ s and TE = 5 ms (an echo time typically used for GE field mapping sequences). EPI images were simulated with a 3 × 3 cm FOV, 64 × 64 matrix, 250 kHz bandwidth, phase encoding gradient duration of 120  $\mu$ s and TE = 20 ms.

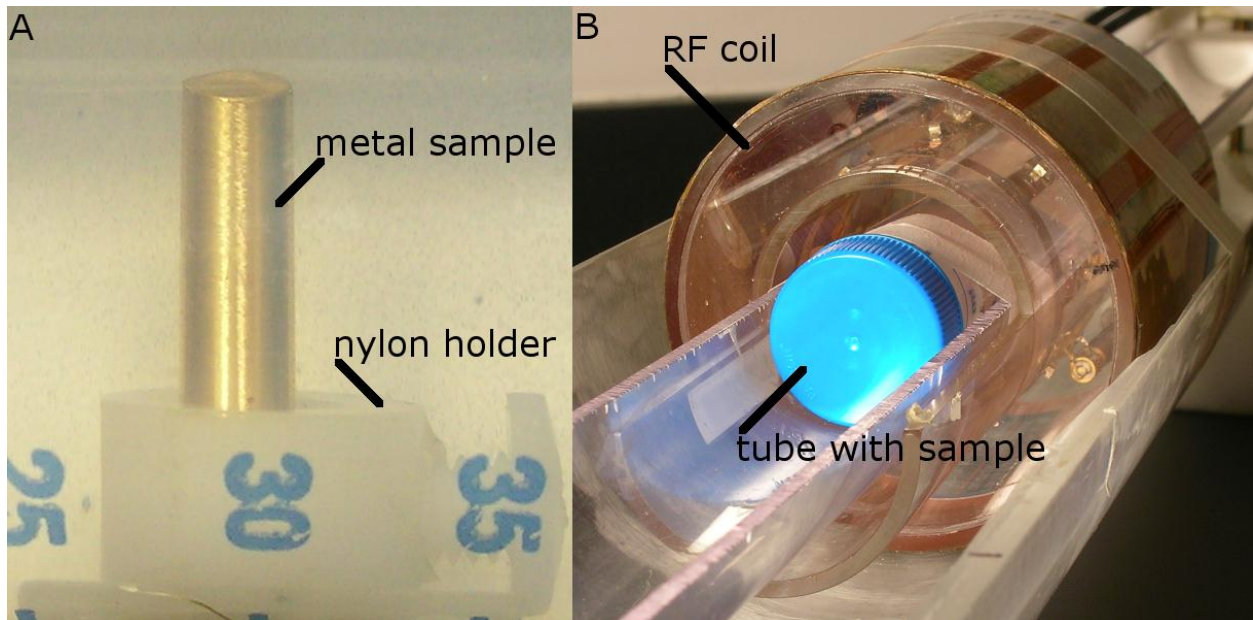


Figure 5-3. A) The Cu-Sn alloy samples were secured in a 50 mL test tube by placing them in a nylon collar and tightening a nylon screw. The 50 mL test tube was then filled with deionized water, bubbles were eliminated from the phantom, and the test tube was capped while submerged in deionized water. B) The test tube was then centered in a volume, transmit and receive, birdcage volume coil that was placed in a cradle for positioning in the magnet bore.

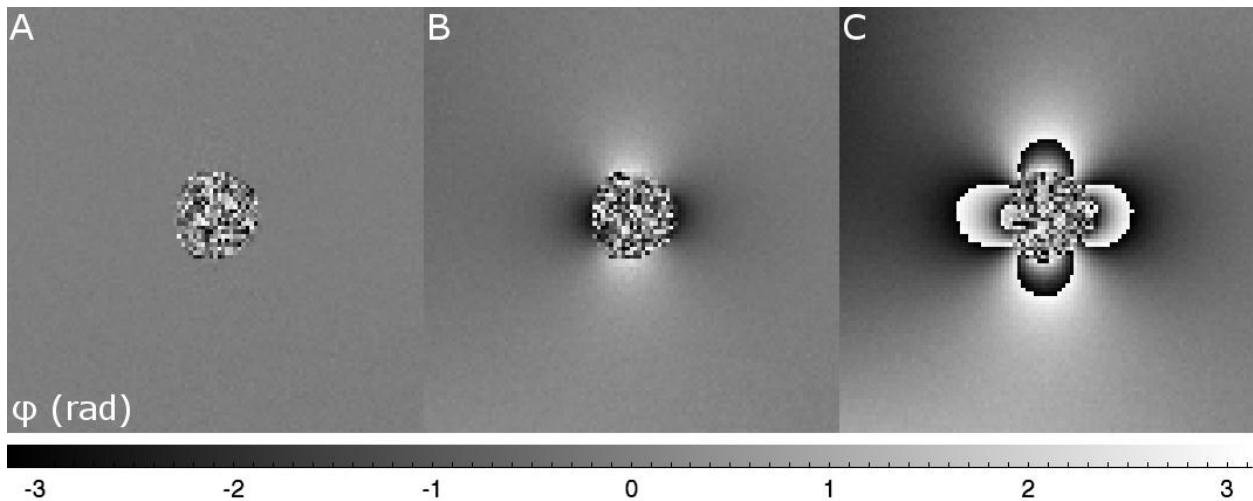


Figure 5-4. Phase maps of complex-divided asymmetric spin echo images with a difference in free precession delay times ( $\Delta T_{fp}$ ) of (A) 0 ms, (B) 0.375 ms and (C) 2.0 ms. A)  $\varphi_{CD} \sim 0$  when  $\Delta T_{fp} = 0$  except at the location of the metal sample due to unreliable phase data from lack of signal. B) The absolute value of the phase is greatest near the surface of the metal and decreases smoothly, with no discontinuities in the phase, towards the edges. C) Sharp transitions in phase ( $-\pi$  to  $\pi$  or  $\pi$  to  $-\pi$ ) indicate phase aliasing due to the periodicity of the inverse tangent function.

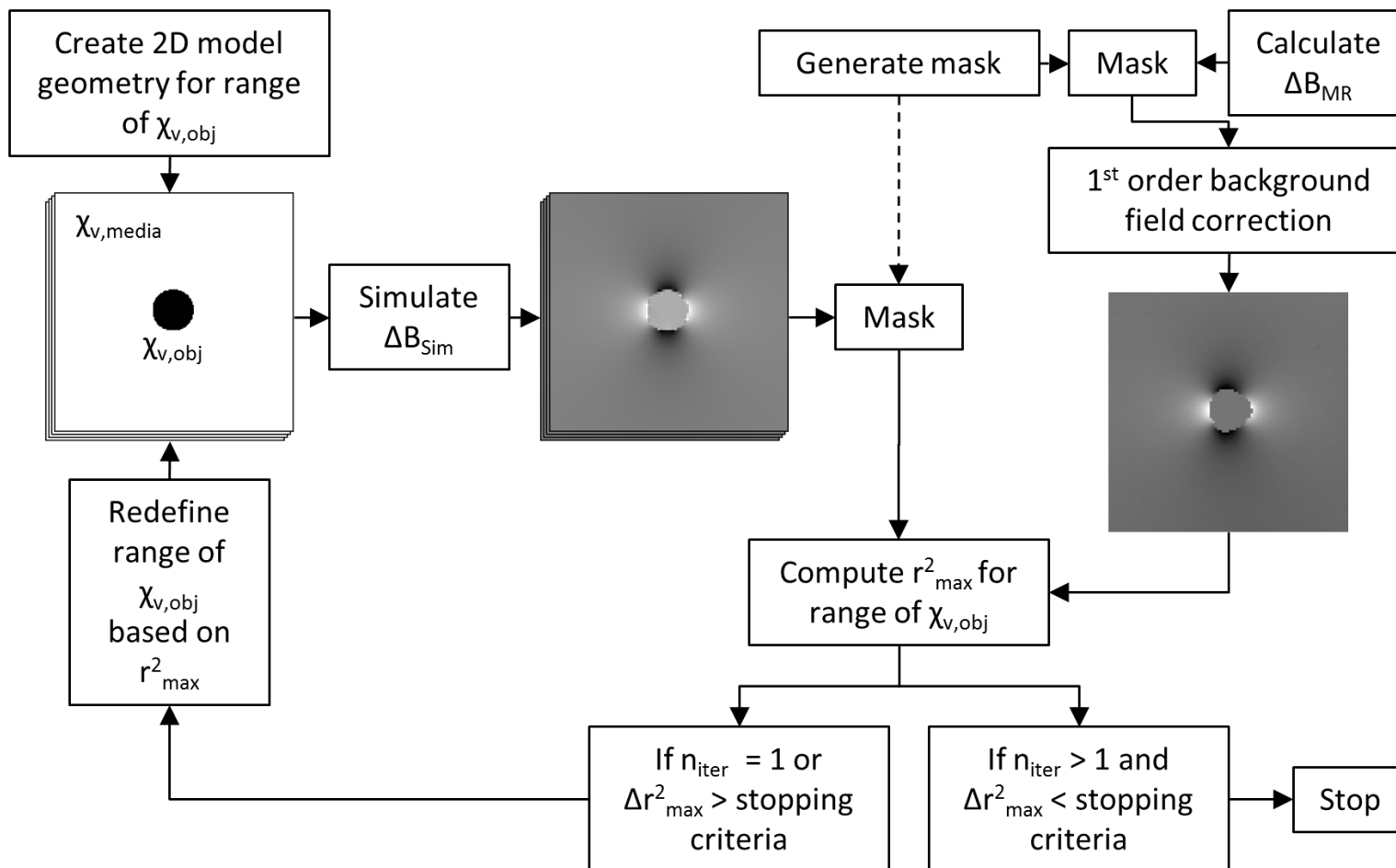


Figure 5-5. Flow-chart summarizing the process of estimating  $\chi_{v,obj}$  from  $\Delta B_{z,MR}$ .

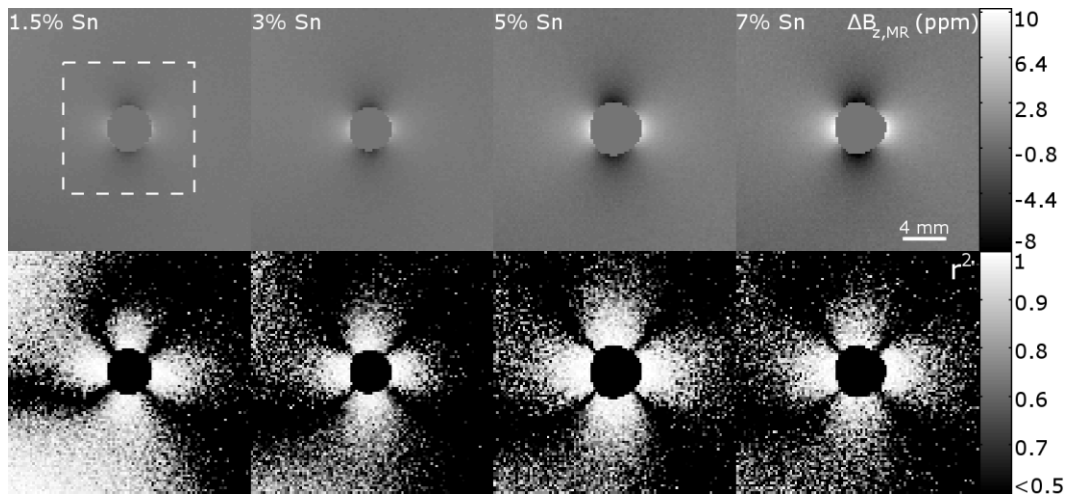


Figure 5-6. (Top row)  $\Delta B_{z,MR}$  maps acquired at 4.7 T for cylindrical Cu-Sn alloy samples composed of 1.5%, 3%, 5% and 7% Sn. The dashed box indicates the  $64 \times 64$  window used when comparing  $\Delta B_{z,MR}$  to  $\Delta B_{z,Sim}$  for the purpose of estimating the susceptibility of the material. (Bottom row) Map of  $r^2$  values generated by performing linear regression on Equation 5-9 on a voxel-by-voxel basis.

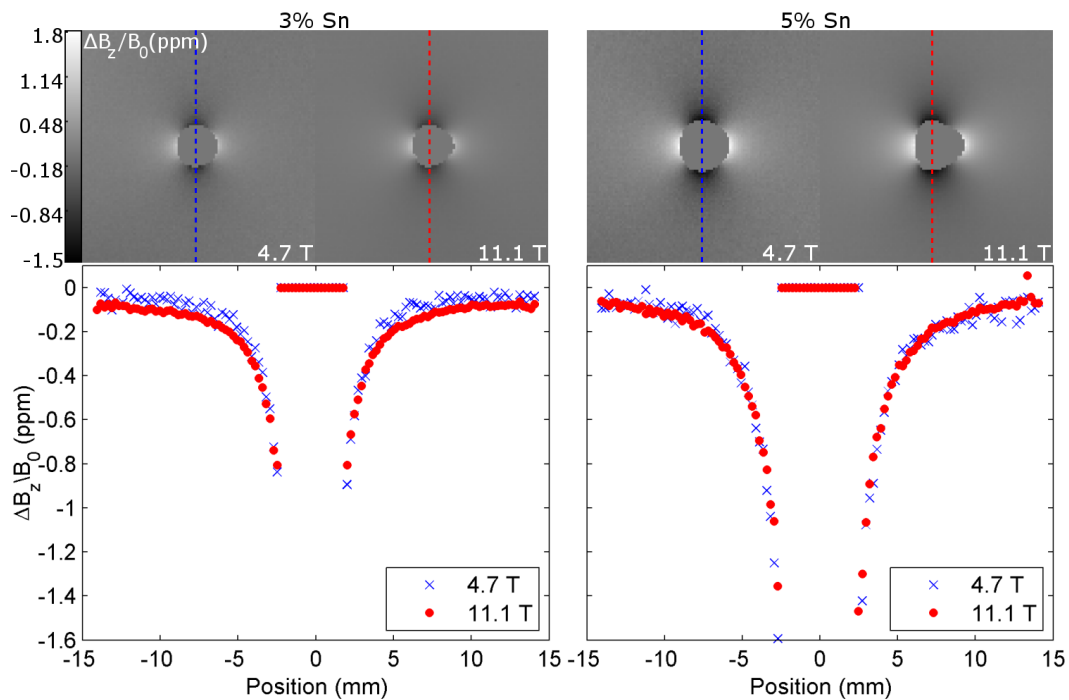


Figure 5-7. (Top row) Comparison of  $\Delta B_{z,MR}$  maps, normalized by acquisition field strength ( $B_0 = 4.7$  T or 11.1 T), for alloys composed of 3% Sn (left) and 5% Sn (right). (Bottom row) Line profile (indicated by dashed lines in top row) of  $\Delta B_{z,MR}/B_0$  in the phase encoding direction. Because  $\Delta B_{z,MR}$  is linearly dependent on  $B_0$ , the normalized line profiles are nearly identical for data acquired at 4.7 and 11.1 T

Table 5-1. Comparison of  $\chi_{v,obj}$  estimations performed at 4.7 T using line fit and image fit methods to SQUID magnetometry measurements. The  $r^2$  value denotes the agreement between  $\Delta B_{z,Sim}$  and  $\Delta B_{z,MR}$  when the simulation was performed with the estimated  $\chi_{v,obj}$ . The standard deviation (SD) was calculated from the variability in  $\chi_{v,obj}$  estimations from four imaging slices and % Diff is the percent difference between estimated values of  $\chi_{v,obj}$  and values measured using SQUID magnetometry.

Sample	SQUID		Line fit				Image fit			
	$\chi_{v,obj}$ (ppm)	SD (ppm)	$\chi_{v,obj}$ (ppm)	$r^2$	SD (ppm)	% diff	$\chi_{v,obj}$ (ppm)	$r^2$	SD (ppm)	% diff
1.5% Sn	-10.36	0.033	-10.2	0.98	0.06	1.4	-10.3	0.95	0.03	0.7
3.0% Sn	-11.05	0.042	-10.8	0.97	0.15	1.9	-11.0	0.98	0.14	0.5
5.1% Sn	-12.69	0.019	-12.4	0.95	0.12	2.0	-12.5	0.90	0.03	1.8
7.0% Sn	-13.98	0.021	-13.9	0.98	0.22	0.7	-14.0	0.93	0.09	0.4

Table 5-2. Comparison of  $\chi_{v,obj}$  estimations performed at 11.1 T using line fit and image fit methods to SQUID magnetometry measurements. The  $r^2$  value denotes the agreement between  $\Delta B_{z,Sim}$  and  $\Delta B_{z,MR}$  when the simulation was performed with the estimated  $\chi_{v,obj}$ . The standard deviation (SD) was calculated from the variability in  $\chi_{v,obj}$  estimations from four imaging slices and % Diff is the percent difference between estimated values of  $\chi_{v,obj}$  and values measured using SQUID magnetometry.

Sample	SQUID		Line fit				Image fit			
	$\chi_{v,obj}$ (ppm)	SD (ppm)	$\chi_{v,obj}$ (ppm)	$r^2$	SD (ppm)	% diff	$\chi_{v,obj}$ (ppm)	$r^2$	SD (ppm)	% diff
3.0% Sn	-11.05	0.042	-11.1	0.98	0.14	0.3	-10.9	0.94	0.18	1.3
5.1% Sn	-12.69	0.019	-12.3	0.99	0.03	3.1	-12.3	0.94	0.03	3.1

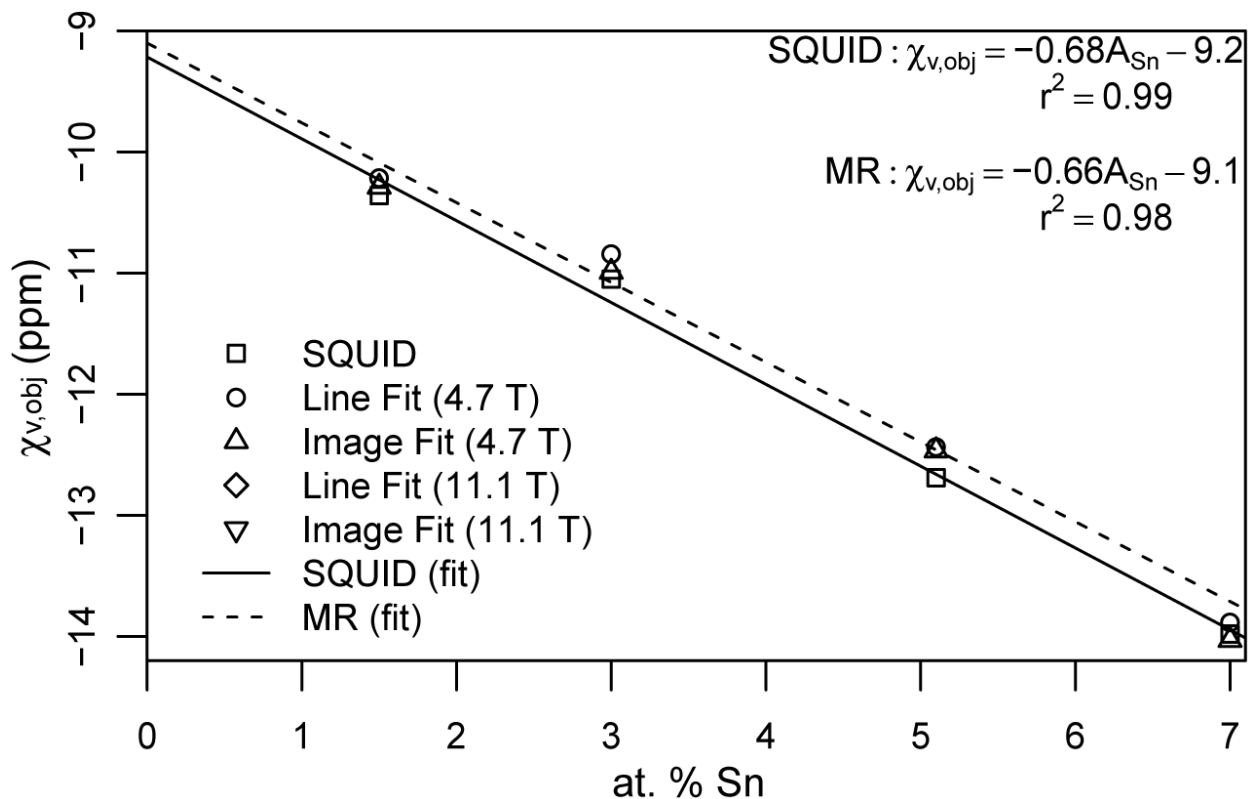


Figure 5-8. Summary of  $\chi_{v,obj}$  for each of the Cu-Sn alloys measured using SQUID magnetometry and estimated using the method outlined in this study at 4.7 T and 11.1 T. The image fit series denotes  $\chi_{v,obj}$  estimated by comparing  $\Delta B_{z,MR}$  and  $\Delta B_{z,Sim}$  using a  $64 \times 64$  window (Figure 5, dashed box) centered about the metal. The line data series corresponds to estimates of  $\chi_{v,obj}$  using a line profile of  $\Delta B_{z,MR}$  and  $\Delta B_{z,Sim}$  in the phase encoding direction which bisects the metal. The equations (top right) indicate the linear relationship between MR-derived values (MR) and SQUID magnetometry values (SQUID) of  $\chi_{v,obj}$  on atomic percentage of Sn ( $A_{Sn}$ ).

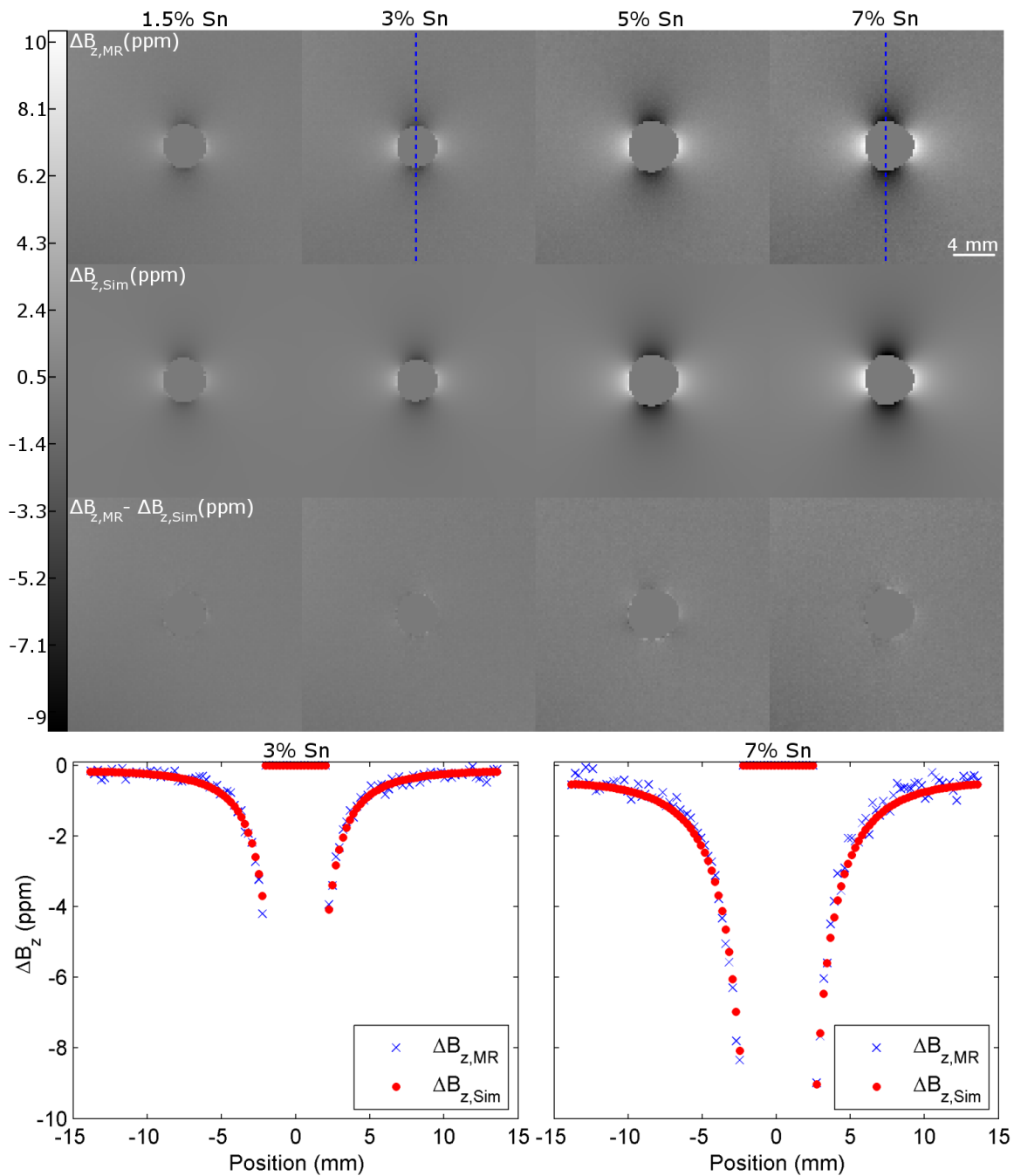


Figure 5-9. Comparison of  $\Delta B_{z,MR}$  (top row) and  $\Delta B_{z,Sim}$  (second row) simulated using MR-derived measurements of  $\chi_{v,obj}$  using the image fit method at 4.7 T. Difference maps (third row) show good agreement between  $\Delta B_{z,MR}$  and  $\Delta B_{z,Sim}$  with the largest deviations occurring at the edge of the Cu-Sn alloy. The line plots (fourth row) indicate the agreement between  $\Delta B_{z,MR}$  and  $\Delta B_{z,Sim}$  simulated using MR-derived measurements of  $\chi_{v,obj}$  using the line fit method. The plots consist of data from the dashed lines indicated in the top row of images.

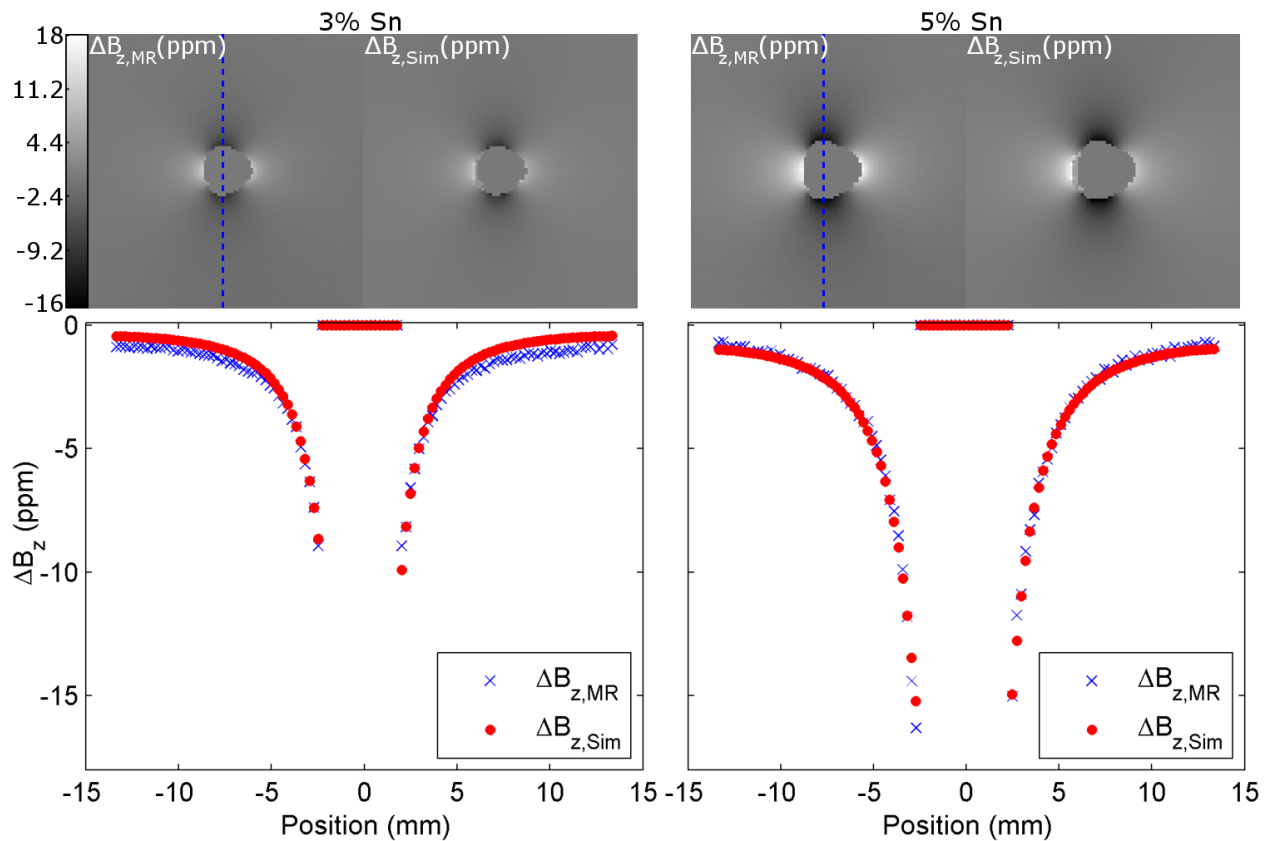


Figure 5-10. Comparison of  $\Delta B_{z,MR}$  (left image) and  $\Delta B_{z,Sim}$  (right image) simulated using MR-derived measurements of  $\chi_{v,obj}$  using the image fit method at 11.1 T. The increased geometric distortion in the frequency encoding direction (left to right) at higher field causes the MR-derived mask of the metal to be shifted relative to the location of the metal in  $\Delta B_{z,Sim}$ . The line plots (fourth row) indicate the agreement between  $\Delta B_{z,MR}$  and  $\Delta B_{z,Sim}$  simulated using MR-derived measurements of  $\chi_{v,obj}$  using the line fit method. The plots consist of data from the dashed lines indicated in the top row of images.

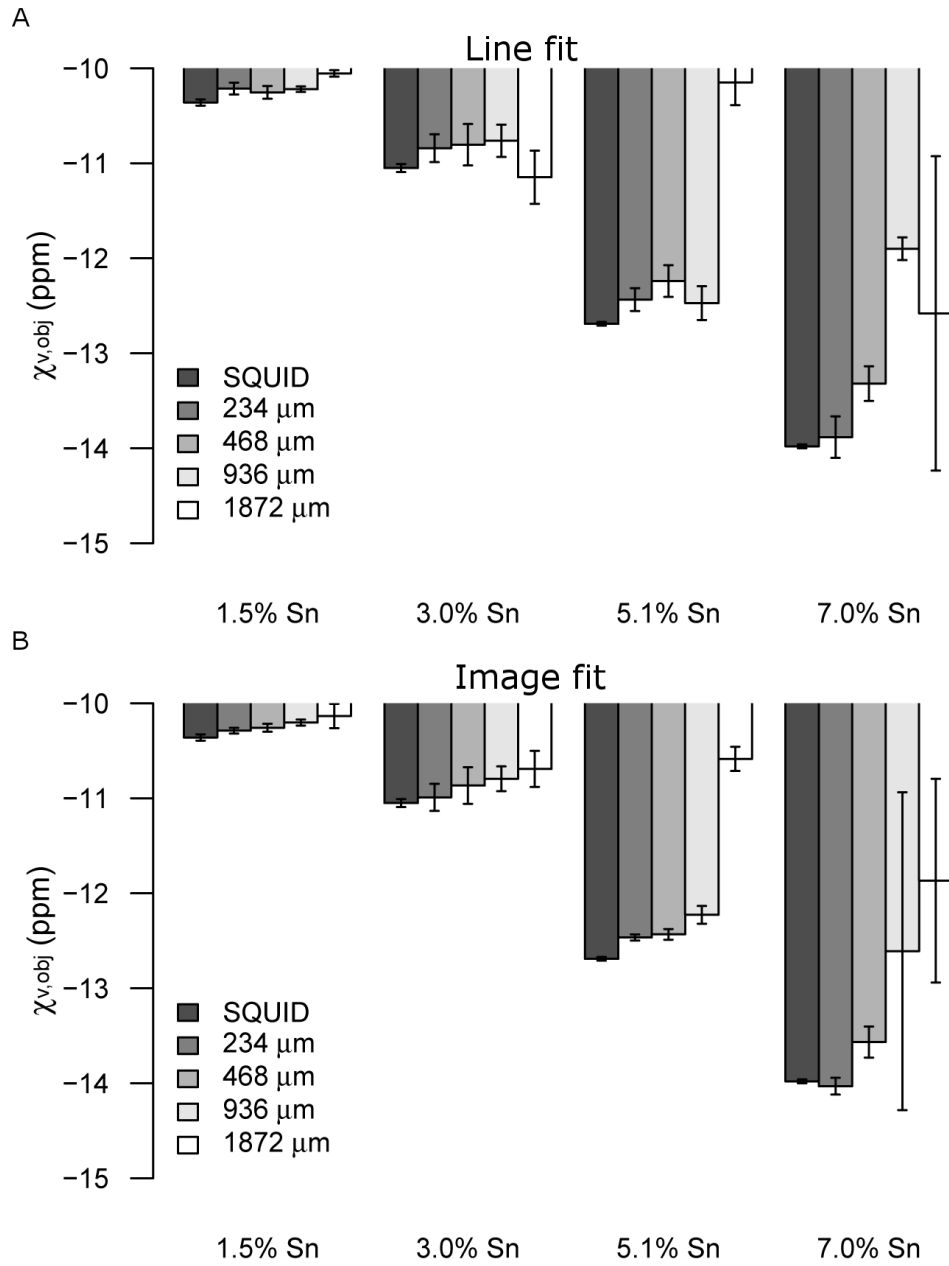


Figure 5-11. The effect of in-plane resolution on MR-derived measurements of  $\chi_{v,obj}$  for the line fit (A) and image fit methods (B).

Table 5-3. Influence of image resolution on  $\chi_{v,obj}$  estimations using the line fit method at 4.7 T. The standard deviation (SD) was calculated from the variability in  $\chi_{v,obj}$  estimations from four imaging slices and % diff is the percent difference between estimated values of  $\chi_{v,obj}$  and values measured using SQUID magnetometry.

Sample	SQUID		234 × 234 $\mu\text{m}^2$			468 × 468 $\mu\text{m}^2$			936 × 936 $\mu\text{m}^2$			1872 × 1872 $\mu\text{m}^2$		
	$\chi_{v,obj}$ (ppm)	SD (ppm)	$\chi_{v,obj}$ (ppm)	SD (ppm)	% diff	$\chi_{v,obj}$ (ppm)	SD (ppm)	% diff	$\chi_{v,obj}$ (ppm)	SD (ppm)	% diff	$\chi_{v,obj}$ (ppm)	SD (ppm)	% diff
1.5% Sn	-10.36	0.033	-10.21	0.06	1.4	-10.25	0.06	1.0	-10.22	0.03	1.4	-10.05	0.03	3.0
3.0% Sn	-11.05	0.042	-10.84	0.15	1.9	-10.80	0.22	2.2	-10.76	0.17	2.6	-11.15	0.28	0.8
5.1% Sn	-12.69	0.019	-12.44	0.12	2.0	-12.24	0.17	3.6	-12.47	0.18	1.7	-10.15	0.24	20.0
7.0% Sn	-13.98	0.021	-13.88	0.22	0.7	-13.32	0.18	4.7	-11.9	0.12	14.9	-12.58	1.65	10.0

Table 5-4. Influence of image resolution on  $\chi_{v,obj}$  estimations using the image fit method at 4.7 T. The standard deviation (SD) was calculated from the variability in  $\chi_{v,obj}$  estimations from four imaging slices and % diff is the percent difference between estimated values of  $\chi_{v,obj}$  and values measured using SQUID magnetometry.

Sample	SQUID		234 × 234 $\mu\text{m}^2$			468 × 468 $\mu\text{m}^2$			936 × 936 $\mu\text{m}^2$			1872 × 1872 $\mu\text{m}^2$		
	$\chi_{v,obj}$ (ppm)	SD (ppm)	$\chi_{v,obj}$ (ppm)	SD (ppm)	% diff	$\chi_{v,obj}$ (ppm)	SD (ppm)	% diff	$\chi_{v,obj}$ (ppm)	SD (ppm)	% diff	$\chi_{v,obj}$ (ppm)	SD (ppm)	% diff
1.5% Sn	-10.36	0.033	-10.29	0.03	0.7	-10.26	0.04	1.0	-10.20	0.03	1.5	-10.13	0.13	2.2
3.0% Sn	-11.05	0.042	-10.99	0.14	0.5	-10.87	0.19	1.7	-10.79	0.13	2.3	-10.69	0.19	3.2
5.1% Sn	-12.69	0.019	-12.47	0.03	1.8	-12.43	0.06	2.0	-12.23	0.09	3.6	-10.59	0.13	16.6
7.0% Sn	-13.98	0.021	-14.03	0.09	0.4	-13.57	0.16	3.0	-12.61	1.7	9.8	-11.87	1.1	15.1

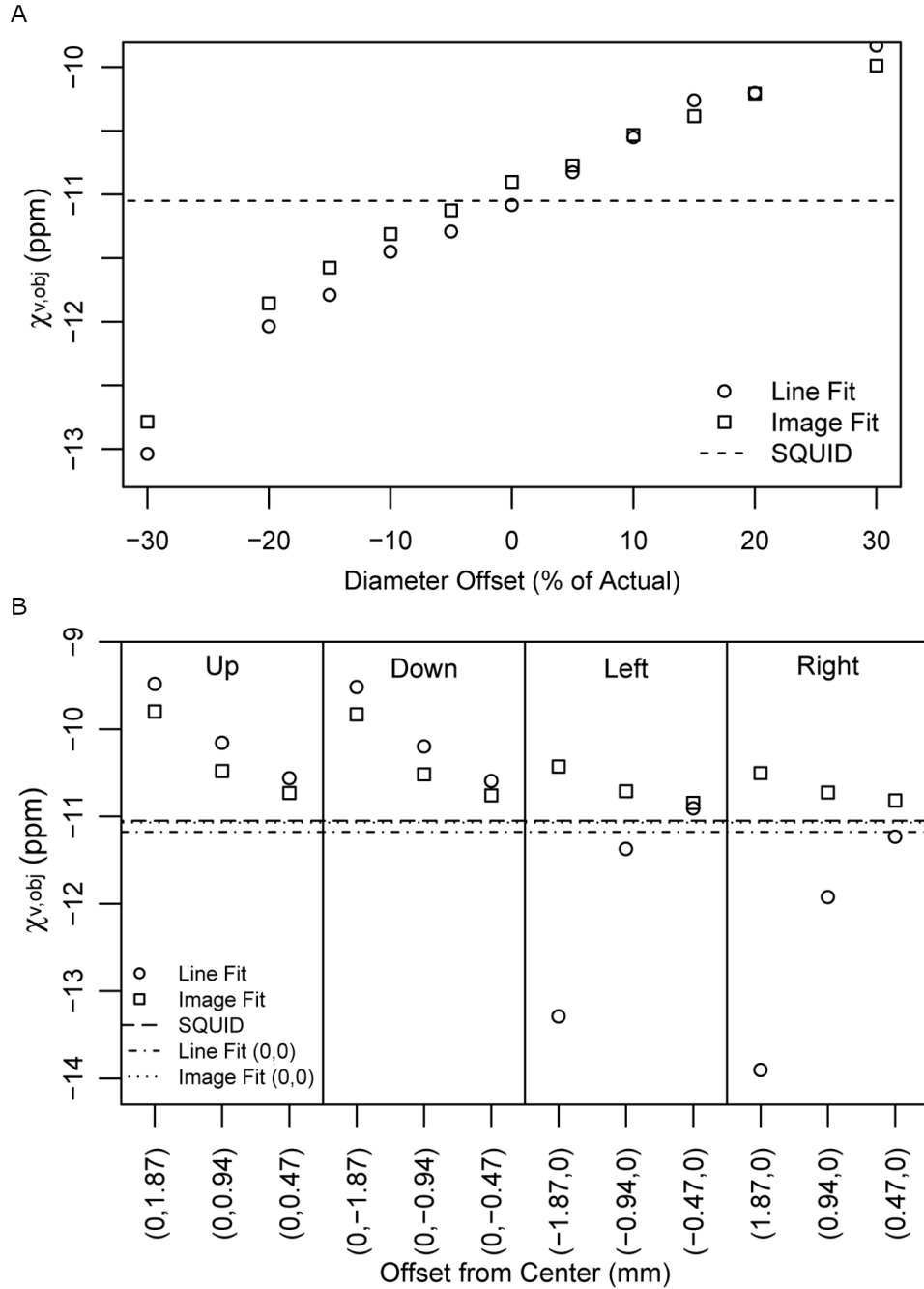


Figure 5-12. MR-derived measurements of  $\chi_{v,obj}$  were performed on the 3.0% sample measured at 11.1 T after modulating the simulation model geometry. Measurements were performed for correct placement of the object while varying the object outer diameter (A) and for the correct object diameter while varying model placement (B).

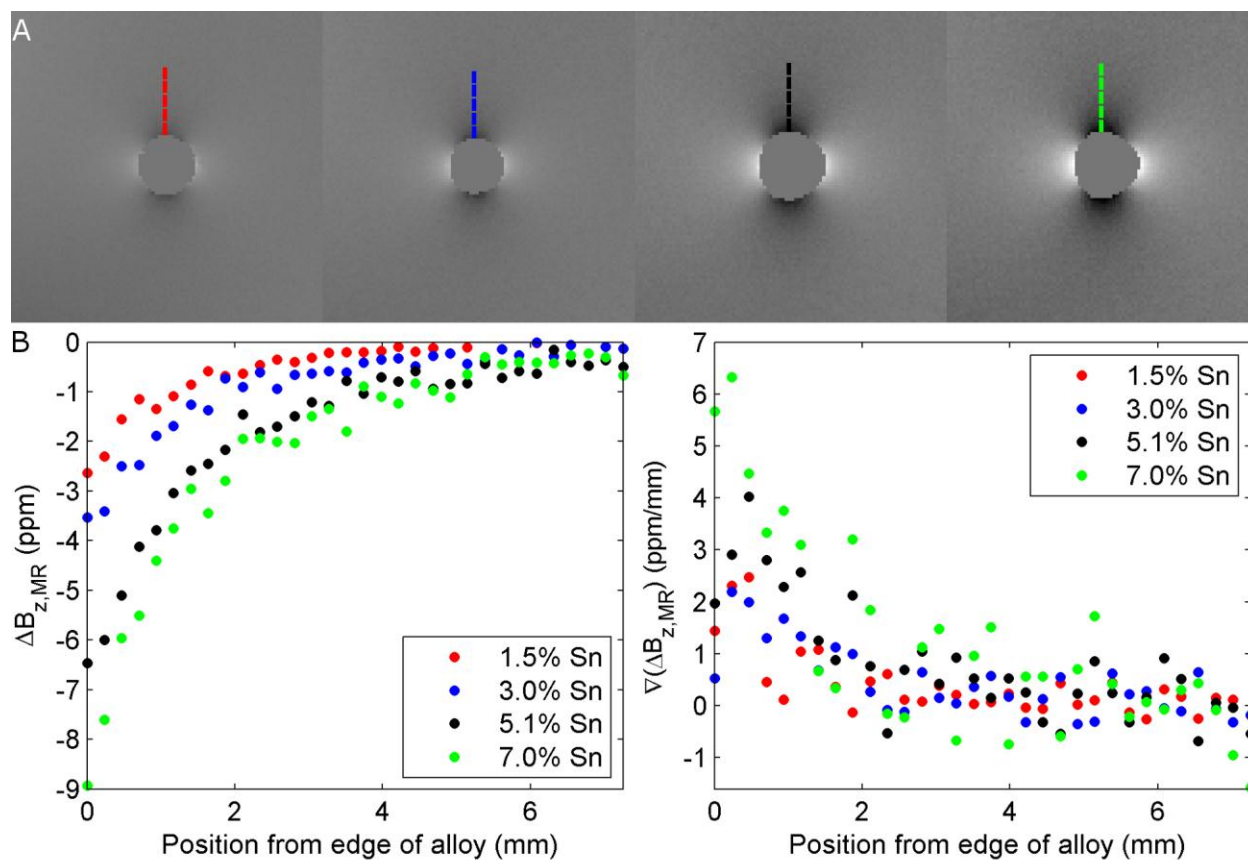


Figure 5-13. Comparison of  $\Delta B_{z,MR}$  collected at 4.7 T along a line profile in the phase encoding direction for the four Cu-Sn alloys. A)  $\Delta B_{z,MR}$  maps of the four Cu-Sn alloys progressing in Sn content from left to right. The dashed line segments indicate the portion of  $\Delta B_{z,MR}$  used for the plots in part B. B) Plot of  $\Delta B_{z,MR}$  as a function of distance from the edge of the cylinder (left). The gradient of  $\Delta B_{z,MR}$  (right) is also plotted as a function of distance from the edge of the cylinder.

## CHAPTER 6 CONCLUSIONS AND FUTURE WORK

### 6.1 Summary

The work presented in this dissertation was focused on improving the utility of MRI for studying CED. Specifically, an experimental framework was developed for studying CED of an MR contrast agent, Gd-albumin, into the rat hippocampus *in vivo* using MRI. This work was completed to study convective transport in a complex tissue structure and to support development of computational models that predict transport of agents delivered to the rat hippocampus by CED. Additionally, the *in vivo* relaxivity of Gd-albumin was characterized in the rat thalamus enabling calculation of contrast agent concentration profiles after delivery to the rat brain using CED. The concentration profiles provide another means, in addition to distribution volumes, of quantitatively comparing experimental CED distributions to those predicted by computational models. Finally, a method for measuring the volume magnetic susceptibility of metal alloys using MRI was developed and tested at 4.7 and 11.1 T. MR measurements of magnetic susceptibility could be used to aid in the development of a metal alloy that is susceptibility-matched to brain tissue, reducing image distortions, and could be fabricated into a cannula that acts as a recording electrode for improved targeting during CED.

In Chapter 3, an MRI methodology was developed for studying CED of Gd-albumin into the rat hippocampus and was applied to determine key tissue structures that influenced transport dynamics. Through dynamic and static MR imaging it was determined that fluid spaces, such as the hippocampal fissure, velum interpositum, and midbrain cistern, influenced the final distribution of the contrast agent. Analysis of

dynamic distribution volume data indicated that these mass sinks affected the distribution of the contrast agent throughout the duration of infusion as the ratio of distribution volume to infusion volume was constant. Therefore, the fluid filled spaces surrounding and penetrating the hippocampus are important features that should be incorporated into computational models for accurate prediction of CED in the rat hippocampus. Additionally, the dense pyramidal cell layers of the hippocampus were found to be resistant to contrast agent penetration while other regions, composed of neuronal projections from the pyramidal cell layers, were less resistant to flow. These qualities led to tracer transport that was primarily parallel to dense cell regions. In addition to studying transport dynamics within the hippocampus, a semi-automatic image segmentation method was developed for determining contrast agent distribution volumes. Distribution volume calculations provided a means of quantitatively comparing experimental and simulated CED distributions in the hippocampus. The use of a semi-automatic routine reduced the analysis time and user bias of distribution volume calculations. To supplement distribution volume data, a projected areas calculation was also developed to characterize the anisotropy of contrast agent distributions.

In Chapter 4, the relaxivity of Gd-albumin was measured in the rat thalamus *in vivo* at 11.1 T to provide another means of quantitatively analyzing CED distributions in the rat brain. This is the first study of macromolecular contrast agent relaxivity *in vivo* and enables concentration profiles of Gd-albumin to be calculated in the rat brain. *In vivo* concentration profiles of the contrast agent could be compared to concentration profiles predicted by computational model to further assess their accuracy. Though the relaxivity measurements performed in this chapter are only applicable to Gd-albumin in the rat

brain at 11.1 T, the presented method could be used to characterize the relaxivity of contrast agents at other field strengths and within additional physiological structures. Additionally, through the work in this chapter a quadrature, receive-only rat brain surface coil and stereotaxic frame were designed and constructed. This hardware could be used in future studies of CED at 11.1 T.

In Chapter 5, a sample holder, imaging protocol and analysis software tool was developed to measure the magnetic susceptibility of metals with a fixed cross-sectional profile using MRI. The presented method could be used by investigators that have access to MRI but do not have access to SQUID magnetometry. Additionally, the MR method of measuring magnetic susceptibility removes certain geometric restrictions associated with SQUID magnetometer measurements. Therefore, magnetic susceptibility measurements can be made on objects without altering their size or shape. The MR method can also be used to measure the volume magnetic susceptibility of unknown materials. Because SQUID magnetometry measures the mass susceptibility of objects, the density must be known in order to calculate the volume susceptibility. Magnetic susceptibility measurements of several different Cu-Sn alloys indicated that the magnetic susceptibility of an alloy can be adjusted by altering the volume fraction of component metals. This approach could be used to tune an alloy to the magnetic susceptibility of brain tissue to eliminate susceptibility mismatch and concomitant image distortions.

## **6.2 Future Work**

Several aspects of *in vivo* CED MRI experiments can be changed to improve these studies. Infusion site coordinates determined from a rat brain atlas were used to target specific structures within the rat brain for all CED experiments described in this

dissertation. As new hardware is developed, such as a brain susceptibility-matched cannula, future studies may employ a combination of pre-surgical imaging and electrophysiological information for more precise targeting within the rat hippocampus. More accurate targeting would improve the comparison between experimental CED distributions and modeling predictions by reducing variability in experimental infusion sites. Additionally, development of new imaging hardware may also improve *in vivo* CED experiments. A phased-array coil could be used to increase SNR and reduce the time required for  $T_1$  mapping and DCE-MRI scans. Reducing pre-infusion scan times may reduce cannula backflow issues by limiting the time available for blood clots to form occluding the cannula tip. The temporal resolution can also be increased by the increased efficiency afforded by a phased-array coil. In present DCE-MRI studies, the silica cannula was fixed to the skull with an adhesive increasing the difficulty of longitudinal studies and prohibiting adjustment of the cannula position based on MR data. An adaptation of the MR compatible stereotaxic frame presented in Chapter 4 could be used to fix the cannula during MR imaging. This would allow adjustments of the cannula position to be made if the placement is undesirable.

The Gd-albumin *in vivo* relaxivity measurements enable concentration profiles to be measured in the rat brain *in vivo* during CED. In addition to CED applications, the relaxivity of Gd-albumin could be used to study rat BBB leakiness in response to mechanical injury or disruption due to seizure activity. The tissue concentrations of Gd-albumin could be calculated as a function of time and incorporated into two-compartment models, similar to those employed in tumor studies of vascular leakiness (Pishko et al., 2011), to quantify BBB permeability. In future studies, MR-derived

concentration profiles may be validated by other imaging modalities such as autoradiography or confocal microscopy. Laser ablation inductively-coupled plasma mass spectroscopy (LA ICP-MS) could also be used to measure the concentration profiles of Gd-albumin in tissue. LA ICP-MS has micron resolution and could measure the concentration of Gd directly; however, there are only a few research institutions which have the necessary equipment. Additionally, measurements of Gd-albumin relaxivity could be performed *in vitro* to determine what biological factors are influencing relaxivity. For example, Gd-albumin relaxivity could be measured in suspensions of erythrocyte ghosts to determine the extent at which compartmentalization affects relaxivity. The aquaporin channels within erythrocyte ghost cell membranes can be altered to determine the effect of exchange rate on relaxivity. Gd-albumin relaxivity could also be measured in homogenized brain tissue to determine the influence of biological molecules on relaxivity. Results from compartmentalized media and homogenized tissue studies could be used to develop a suitable brain tissue analog for contrast agent relaxivity studies making relaxivity experiments at different field strengths easier and faster to conduct. This would also enable the *in vivo* relaxivities of new contrast agents (e.g. Gd-DTPA loaded-nanoparticles) to be estimated more efficiently.

In addition to calculating contrast agent concentration profiles using relaxivity, other methods of calculating contrast agent concentration could be explored. With the development of the Selective Wirelessly Adjustable Multifrequency Probe (SWAMP) and Automated Impedance Matching (AIM) systems, acquiring  $^1\text{H}$  and  $^{19}\text{F}$  images may be possible. Therefore, drugs, proteins, or nanoparticles could be labeled with  $^{19}\text{F}$  and then alternating  $^1\text{H}$  and  $^{19}\text{F}$  images could be acquired to visualize the distribution of the

tracer within tissue. Quantitative susceptibility mapping (QSM) provides another potential method of measuring contrast agent concentration as the susceptibility changes in tissue induced by the contrast agent could be measured.

One shortcoming of the MR measurements of magnetic susceptibility was the inability to tune the susceptibility of the Cu-Sn alloy to that of the brain. The addition of paramagnetic white Sn to diamagnetic Cu should have resulted in an alloy that matched the susceptibility of brain for some volume fraction of Sn; however, it is possible that during the casting process Sn switched allotropes to diamagnetic gray Sn creating increasingly diamagnetic alloys with increasing Sn content. Therefore, future studies will be aimed at creating alloys of silver (Ag) and palladium (Pd). Ag-Pd alloy systems have solid solubility across all compositions and neither element has an allotropic form. It should be expected that some combination of Ag and Pd will result in a conductive alloy that has the same magnetic susceptibility of the brain. In addition to matching the magnetic susceptibility of brain, biocompatibility studies will have to be conducted to insure the alloy can be safely implanted in the rat brain. Additional studies will also be required to investigate the susceptibility of the alloy throughout the manufacturing process used to produce cannulae and electrodes. Processes such as swaging, rolling and drawing could change microstructure of the material thus potentially altering the magnetic susceptibility. Changes to magnetic susceptibility incurred during manufacturing processes will have to be taken into account when defining the appropriate metal composition to susceptibility-match cannulae and electrodes to brain tissue.

## LIST OF REFERENCES

- Abbott NJ. Evidence for bulk flow of brain interstitial fluid: significance for physiology and pathology. *Neurochem Int*, 2004; 45: 545-52.
- Abbott NJ, Ronnback L, Hansson E. Astrocyte-endothelial interactions at the blood-brain barrier. *Nat Rev Neurosci*, 2006; 7: 41-53.
- Andersen AH. On the Rician distribution of noisy MRI data. *Magn Reson Med*, 1996; 36: 331-3.
- Andrew ER. *Nuclear Magnetic Resonance*, First ed. Cambridge University Press, 1955.
- Armitage P, Berry G. *Statistical Methods in Medical Research*, 3rd ed. ed. Blackwell Scientific: Oxford, UK, 1994.
- Astary GW, Kantorovich S, Carney PR, Mareci TH, Sarntinoranont M. Regional convection-enhanced delivery of gadolinium-labeled albumin in the rat hippocampus in vivo. *J Neurosci Methods*, 2010; 187: 129-37.
- Bagher-Ebadian H, Jiang Q, Ewing JR. A modified Fourier-based phase unwrapping algorithm with an application to MRI venography. *J. Magn. Reson. Imaging*, 2008; 27: 649-52.
- Bakker CJG, Bhagwandien R, Moerland MA, Fuderer M. Susceptibility Artifacts in 2dft Spin-Echo and Gradient-Echo Imaging - the Cylinder Model Revisited. *Magnetic Resonance Imaging*, 1993; 11: 539-48.
- Bakker CJG, Bhagwandien R, Moerland MA, Ramos LMP. Simulation of Susceptibility Artifacts in 2d and 3d Fourier-Transform Spin-Echo and Gradient-Echo Magnetic-Resonance-Imaging. *Magnetic Resonance Imaging*, 1994; 12: 767-74.
- Bakker CJG, de Leeuw H, Vincken KL, Vonken EJ, Hendrikse J. Phase gradient mapping as an aid in the analysis of object-induced and system-related phase perturbations in MRI. *Phys. Med. Biol.*, 2008; 53: N349-N58.
- Banks WA. Developing drugs that can cross the blood-brain barrier: applications to Alzheimer's disease. *BMC neuroscience*, 2008; 9 Suppl 3: S2.
- Belliveau JW, Kennedy DN, McKinstry RC, Buchbinder BR, Weisskoff RM, Cohen MS, Vevea JM, Brady TJ, Rosen BR. Functional Mapping of the Human Visual-Cortex by Magnetic-Resonance-Imaging. *Science*, 1991; 254: 716-9.
- Bernacki J, Dobrowolska A, Nierwinska K, Malecki A. Physiology and pharmacological role of the blood-brain barrier. *Pharmacol Rep*, 2008; 60: 600-22.
- Bertini I, Luchinat C. Chapter 3 Relaxation. *Coordination Chemistry Reviews*, 1996; 150: 77-110.

- Beuf O, Briguet A, Lissac M, Davis R. Magnetic resonance imaging for the determination of magnetic susceptibility of materials. *J. Magn. Reson. Ser. B*, 1996; 112: 111-8.
- Blasberg RG, Patlak C, Fenstermacher JD. Intrathecal chemotherapy: brain tissue profiles after ventriculocisternal perfusion. *The Journal of pharmacology and experimental therapeutics*, 1975; 195: 73-83.
- Bloch F, Hansen W, Packard M. Nuclear Induction. *Physical Review*, 1946; 69: 127.
- Bloembergen N. Proton Relaxation Times in Paramagnetic Solutions. *The Journal of Chemical Physics*, 1957; 27: 572-3.
- Bloembergen N, Morgan LO. Proton Relaxation Times in Paramagnetic Solutions. Effects of Electron Spin Relaxation. *The Journal of Chemical Physics*, 1961; 34: 842-50.
- Bloembergen N, Purcell EM, Pound RV. Relaxation Effects in Nuclear Magnetic Resonance Absorption. *Physical Review*, 1948; 73: 679-712.
- Bobo RH, Laske DW, Akbasak A, Morrison PF, Dedrick RL, Oldfield EH. Convection-Enhanced Delivery of Macromolecules in the Brain. *Proc Natl Acad Sci U S A*, 1994; 91: 2076-80.
- Bowers R. Magnetic Susceptibility of Copper Metal at Low Temperatures. *Physical Review*, 1956; 102: 1486-8.
- Bruce JN, Fine RL, Canoll P, Yun J, Kennedy BC, Rosenfeld SS, Sands SA, Surapaneni K, Lai R, Yanes CL, Bagiella E, Delapaz RL. Regression of recurrent malignant gliomas with convection-enhanced delivery of topotecan. *Neurosurgery*, 2011; 69: 1272-80.
- Burtea C, Laurent S, Vander Elst L, Muller RN. Contrast agents: magnetic resonance. *Handb Exp Pharmacol*, 2008: 135-65.
- Caravan P, Ellison JJ, McMurry TJ, Lauffer RB. Gadolinium(III) chelates as MRI contrast agents: Structure, dynamics, and applications. *Chemical Reviews*, 1999; 99: 2293-352.
- Caravan P, Farrar CT, Frullano L, Uppal R. Influence of molecular parameters and increasing magnetic field strength on relaxivity of gadolinium- and manganese-based T1 contrast agents. *Contrast media & molecular imaging*, 2009; 4: 89-100.
- Carlsson A, Starck G, Ljungberg M, Ekholm S, Forssell-Aronsson E. Accurate and sensitive measurements of magnetic susceptibility using echo planar imaging. *Magnetic Resonance Imaging*, 2006; 24: 1179-85.

- Chen MY, Lonser RR, Morrison PF, Governale LS, Oldfield EH. Variables affecting convection-enhanced delivery to the striatum: a systematic examination of rate of infusion, cannula size, infusate concentration, and tissue-cannula sealing time. *J Neurosurg*, 1999; 90: 315-20.
- Chen X, Astarly GW, Mareci TH, Sarntinoranont M. In Vivo Contrast-Enhanced MR Imaging of Direct Infusion into Rat Peripheral Nerves. *Annals of biomedical engineering*, 2011; 39: 2823-34.
- Chen X, Astarly GW, Sepulveda H, Mareci TH, Sarntinoranont M. Quantitative assessment of macromolecular concentration during direct infusion into an agarose hydrogel phantom using contrast-enhanced MRI. *Magn Reson Imaging*, 2008; 26: 1433-41.
- Chen X, Sarntinoranont M. Biphasic finite element model of solute transport for direct infusion into nervous tissue. *Annals of biomedical engineering*, 2007; 35: 2145-58.
- Cheng YC, Hsieh CY, Neelavalli J, Liu Q, Dawood MS, Haacke EM. A complex sum method of quantifying susceptibilities in cylindrical objects: the first step toward quantitative diagnosis of small objects in MRI. *Magn Reson Imaging*, 2007; 25: 1171-80.
- Cheng YC, Neelavalli J, Haacke EM. Limitations of calculating field distributions and magnetic susceptibilities in MRI using a Fourier based method. *Phys Med Biol*, 2009a; 54: 1169-89.
- Cheng YCN, Hsieh CY, Neelavalli J, Haacke EM. Quantifying effective magnetic moments of narrow cylindrical objects in MRI. *Phys. Med. Biol.*, 2009b; 54: 7025-44.
- Cherubini A, Peran P, Hagberg GE, Varsi AE, Luccichenti G, Caltagirone C, Sabatini U, Spalletta G. Characterization of white matter fiber bundles with T2\* relaxometry and diffusion tensor imaging. *Magn Reson Med*, 2009; 61: 1066-72.
- Cobb NJ, Surewicz WK. Prion diseases and their biochemical mechanisms. *Biochemistry*, 2009; 48: 2574-85.
- Damadian R. Tumor detection by nuclear magnetic resonance. *Science*, 1971; 171: 1151-3.
- de Graaf RA, Brown PB, McIntyre S, Nixon TW, Behar KL, Rothman DL. High magnetic field water and metabolite proton T-1 and T-2 relaxation in rat brain in vivo. *Magn. Reson. Med.*, 2006; 56: 386-94.
- Denk C, Torres EH, Mackay A, Rauscher A. The influence of white matter fibre orientation on MR signal phase and decay. *NMR Biomed*, 2010; 24: 246-52.
- Deoni SC. Magnetic resonance relaxation and quantitative measurement in the brain. *Methods Mol Biol*; 711: 65-108.

Does MD, Gore JC. Compartmental study of T(1) and T(2) in rat brain and trigeminal nerve in vivo. *Magn Reson Med*, 2002; 47: 274-83.

Donahue KM, Burstein D, Manning WJ, Gray ML. Studies of Gd-DTPA relaxivity and proton exchange rates in tissue. *Magn.Reson.Med.*, 1994; 32: 66-76.

Du YPP, Dalwani M, Wylie K, Claus E, Tregellas JR. Reducing susceptibility artifacts in fMRI using volume-selective z-shim compensation. *Magn. Reson. Med.*, 2007; 57: 396-404.

Dupont WD, Plummer WD, Jr. Power and sample size calculations for studies involving linear regression. *Controlled clinical trials*, 1998; 19: 589-601.

Edzes HT, Samulski ET. Measurement of Cross-Relaxation Effects in Proton Nmr Spin-Lattice Relaxation of Water in Biological-Systems - Hydrated Collagen and Muscle. *J. Magn. Reson.*, 1978; 31: 207-29.

Fiandaca MS, Varenika V, Eberling J, McKnight T, Bringas J, Pivrotto P, Beyer J, Hadaczek P, Bowers W, Park J, Federoff H, Forsayeth J, Bankiewicz KS. Real-time MR imaging of adeno-associated viral vector delivery to the primate brain. *Neuroimage*, 2008.

Foley CP, Nishimura N, Neeves KB, Schaffer CB, Olbricht WL. Flexible microfluidic devices supported by biodegradable insertion scaffolds for convection-enhanced neural drug delivery. *Biomed Microdevices*, 2009; 11: 915-24.

Franconi F, Lemaire L, Marescaux L, Jallet P, Le Jeune JJ. In vivo quantitative microimaging of rat spinal cord at 7T. *Magn. Reson. Med.*, 2000; 44: 893-8.

Freed JH. Dynamic Effects of Pair Correlation-Functions on Spin Relaxation by Translational Diffusion in Liquids .2. Finite Jumps and Independent T1 Processes. *J. Chem. Phys.*, 1978; 68: 4034-7.

Freedman FB, Johnson JA. Equilibrium and kinetic properties of the Evans blue-albumin system. *The American journal of physiology*, 1969; 216: 675-81.

Fung BM. Correlation of relaxation time with water content in muscle and brain tissues. *Biochimica et Biophysica Acta (BBA) - General Subjects*, 1977; 497: 317-22.

Garroway AN, Grannell PK, Mansfield P. Image-Formation in Nmr by a Selective Irradiative Process. *Journal of Physics C-Solid State Physics*, 1974; 7: L457-L62.

Groothuis DR, Vavra MW, Schlageter KE, Kang EW, Itskovich AC, Hertzler S, Allen CV, Lipton HL. Efflux of drugs and solutes from brain: the interactive roles of diffusional transcapillary transport, bulk flow and capillary transporters. *J Cereb Blood Flow Metab*, 2007; 27: 43-56.

Grösch L, Noack F. NMR relaxation investigation of water mobility in aqueous bovine serum albumin solutions. *Biochimica et Biophysica Acta (BBA) - Protein Structure*, 1976; 453: 218-32.

Haacke EM, Brown RW, Thompson MR, Venkatesan R. *Magnetic Resonance Imaging Physical Principles and Sequence Design*. John Wiley & Sons: New York, 1999.

Haar PJ, Broaddus WC, Chen ZJ, Fatouros PP, Gillies GT, Corwin FD. Gd-DTPA T1 relaxivity in brain tissue obtained by convection-enhanced delivery, magnetic resonance imaging and emission spectroscopy. *Phys Med Biol*, 2010; 55: 3451-65.

Hadaczek P, Yamashita Y, Mirek H, Tamas L, Bohn MC, Noble C, Park JW, Bankiewicz K. The "perivascular pump" driven by arterial pulsation is a powerful mechanism for the distribution of therapeutic molecules within the brain. *Molecular therapy : the journal of the American Society of Gene Therapy*, 2006; 14: 69-78.

Higashi T, Ashida N, Takeuchi T. Orientation of blood cells in static magnetic field. *Physica B*, 1997; 237: 616-20.

Hsu JJ, Glover GH. Mitigation of susceptibility-induced signal loss in neuroimaging using localized shim coils. *Magn Reson Med*, 2005; 53: 243-8.

Hwang LP, Freed JH. Dynamic Effects of Pair Correlation-Functions on Spin Relaxation by Translational Diffusion in Liquids. *J. Chem. Phys.*, 1975; 63: 4017-25.

Ihaka R, Gentleman R. R: A Language for Data Analysis and Graphics. *Journal of Computational and Graphical Statistics*, 1996; 5: 299-314.

Jagannathan J, Walbridge S, Butman JA, Oldfield EH, Lonser RR. Effect of ependymal and pial surfaces on convection-enhanced delivery. *J Neurosurg*, 2008; 109: 547-52.

Kc R, Henry ID, Park GHJ, Aghdasi A, Raftery D. New solenoidal microcoil NMR probe using zero-susceptibility wire. *Concepts in Magnetic Resonance Part B: Magnetic Resonance Engineering*, 2010; 37B: 13-9.

Kim H, Lizak MJ, Tansey G, Csaky KG, Robinson MR, Yuan P, Wang NS, Lutz RJ. Study of ocular transport of drugs released from an intravitreal implant using magnetic resonance imaging. *Annals of biomedical engineering*, 2005; 33: 150-64.

Kim JH, Astary GW, Chen X, Mareci TH, Sarntinoranont M. Voxelized model of interstitial transport in the rat spinal cord following direct infusion into white matter. *J Biomech Eng*, 2009; 131: 071007-1 - -8.

Kim JH, Mareci TH, Sarntinoranont M. A voxelized model of direct infusion into the corpus callosum and hippocampus of the rat brain: model development and parameter analysis. *Med Biol Eng Comput*, 2010; 48: 203-14.

Koay CG, Basser PJ. Analytically exact correction scheme for signal extraction from noisy magnitude MR signals. *J. Magn. Reson.*, 2006; 179: 317-22.

Koch KM, Hargreaves BA, Pauly KB, Chen W, Gold GE, King KF. Magnetic resonance imaging near metal implants. *J Magn Reson Imaging*, 2010; 32: 773-87.

Koch KM, Lorbiecki JE, Hinks RS, King KF. A multispectral three-dimensional acquisition technique for imaging near metal implants. *Magn Reson Med*, 2009; 61: 381-90.

Koch KM, Papademetris X, Rothman DL, de Graaf RA. Rapid calculations of susceptibility-induced magnetostatic field perturbations for in vivo magnetic resonance. *Phys Med Biol*, 2006; 51: 6381-402.

Korb JP, Bryant RG. The physical basis for the magnetic field dependence of proton spin-lattice relaxation rates in proteins. *J. Chem. Phys.*, 2001; 115: 10964-74.

Krauze MT, Saito R, Noble C, Tamas M, Bringas J, Park JW, Berger MS, Bankiewicz K. Reflux-free cannula for convection-enhanced high-speed delivery of therapeutic agents. *J Neurosurg*, 2005; 103: 923-9.

Krauze MT, Vandenberg SR, Yamashita Y, Saito R, Forsayeth J, Noble C, Park J, Bankiewicz KS. Safety of real-time convection-enhanced delivery of liposomes to primate brain: a long-term retrospective. *Exp Neurol*, 2008; 210: 638-44.

Landis CS, Li X, Telang FW, Coderre JA, Micca PL, Rooney WD, Latour LL, Vetek G, Palyka I, Springer CS, Jr. Determination of the MRI contrast agent concentration time course in vivo following bolus injection: effect of equilibrium transcytolemmal water exchange. *Magn Reson Med*, 2000; 44: 563-74.

Laske DW, Morrison PF, Lieberman DM, Corthesy ME, Reynolds JC, Stewart-Henney PA, Koong SS, Cummins A, Paik CH, Oldfield EH. Chronic interstitial infusion of protein to primate brain: determination of drug distribution and clearance with single-photon emission computerized tomography imaging. *J Neurosurg*, 1997; 87: 586-94.

Lauffer RB. Paramagnetic Metal-Complexes as Water Proton Relaxation Agents for Nmr Imaging - Theory and Design. *Chemical Reviews*, 1987; 87: 901-27.

Lauterbur PC. Image Formation by Induced Local Interactions: Examples Employing NMR. *Nature*, 1973; 242: 190-1.

Lee GC, Goodwill PW, Phuong K, Inglis BA, Scott GC, Hargreaves BA, Li L, Chen AC, Shah RN, Conolly SM. Pyrolytic Graphite Foam: A Passive Magnetic Susceptibility Matching Material. *J. Magn. Reson. Imaging*; 32: 684-91.

Lee JH, Durand R, Gradinaru V, Zhang F, Goshen I, Kim DS, Fenno LE, Ramakrishnan C, Deisseroth K. Global and local fMRI signals driven by neurons defined optogenetically by type and wiring. *Nature*, 2010; 465: 788-92.

- Lee SJ, Sun J, Flint JJ, Guo S, Xie HK, King MA, Sarntinoranont M. Optically based-indentation technique for acute rat brain tissue slices and thin biomaterials. *Journal of biomedical materials research. Part B, Applied biomaterials*, 2011; 97: 84-95.
- Levitt MH. *Spin Dynamics Basics of Nuclear Magnetic Resonance*. John Wiley & Sons, Ltd, 2001.
- Li W, Wu B, Liu C. Quantitative susceptibility mapping of human brain reflects spatial variation in tissue composition. *Neuroimage*, 2011; 55: 1645-56.
- Li X, Rooney WD, Springer CS, Jr. A unified magnetic resonance imaging pharmacokinetic theory: intravascular and extracellular contrast reagents. *Magn Reson Med*, 2005; 54: 1351-9.
- Lieberman DM, Laske DW, Morrison PF, Bankiewicz KS, Oldfield EH. Convection-enhanced distribution of large molecules in gray matter during interstitial drug infusion. *J Neurosurg*, 1995; 82: 1021-9.
- Liu C, Li W, Johnson GA, Wu B. High-field (9.4 T) MRI of brain dysmyelination by quantitative mapping of magnetic susceptibility. *Neuroimage*, 2011; 56: 930-8.
- Lonser RR, Gogate N, Morrison PF, Wood JD, Oldfield EH. Direct convective delivery of macromolecules to the spinal cord. *J Neurosurg*, 1998; 89: 616-22.
- Lonser RR, Walbridge S, Garmestani K, Butman JA, Walters HA, Vortmeyer AO, Morrison PF, Brechbiel MW, Oldfield EH. Successful and safe perfusion of the primate brainstem: in vivo magnetic resonance imaging of macromolecular distribution during infusion. *J Neurosurg*, 2002; 97: 905-13.
- Lu WM, Pauly KB, Gold GE, Pauly JM, Hargreaves BA. SEMAC: Slice Encoding for Metal Artifact Correction in MRI. *Magn. Reson. Med.*, 2009; 62: 66-76.
- Mansfield P, Grannell PK. "Diffraction" and Microscopy in Solids and Liquids by NMR. *Phys Rev B*, 1975; 12: 3618-34.
- Mansfield P, Maudsley AA, Baines T. Fast Scan Proton Density Imaging by Nmr. *Journal of Physics E-Scientific Instruments*, 1976; 9: 271-8.
- Mardor Y, Rahav O, Zauberman Y, Lidar Z, Ocherashvilli A, Daniels D, Roth Y, Maier SE, Orenstein A, Ram Z. Convection-enhanced drug delivery: increased efficacy and magnetic resonance image monitoring. *Cancer Res*, 2005; 65: 6858-63.
- Marques JP, Bowtell R. Application of a Fourier-based method for rapid calculation of field inhomogeneity due to spatial variation of magnetic susceptibility. 2005; 25B: 65-78.
- Martinez-Santesteban FM, Swanson SD, Noll DC, Anderson DJ. Magnetic field perturbation of neural recording and stimulating microelectrodes. *Phys Med Biol*, 2007; 52: 2073-88.

Maruthamuthu M, Subramanian E. Binding of Evans Blue onto Poly (N-Vinyl-2-Pyrrolidone). *Polym. Bull.*, 1985; 14: 207-12.

Mazel T, Simonova Z, Sykova E. Diffusion heterogeneity and anisotropy in rat hippocampus. *Neuroreport.*, 1998; 9: 1299-304.

McConnell HM. Reaction Rates by Nuclear Magnetic Resonance. *J. Chem. Phys.*, 1958; 28: 430-1.

Meyerand ME, Cremillieux Y, Wadghiri YZ, Azzawi A, Hoopes PJ, Dunn JF. In vivo gradient echo microimaging of rodent spinal cord at 7 T. *Magn Reson Med*, 1998; 40: 789-91.

Michaeli S, Garwood M, Zhu XH, DelaBarre L, Andersen P, Adriany G, Merkle H, Ugurbil K, Chen W. Proton T-2 relaxation study of water, N-acetylaspartate, and creatine in human brain using Hahn and Carr-Purcell spin echoes at 4T and 7T. *Magn. Reson. Med.*, 2002; 47: 629-33.

Mihai G, Nout YS, Tovar CA, Miller BA, Schmalbrock P, Bresnahan JC, Beattie MS. Longitudinal comparison of two severities of unilateral cervical spinal cord injury using magnetic resonance imaging in rats. *Journal of Neurotrauma*, 2008; 25: 1-18.

Morkenborg J, Taagehoj JF, Vaever PN, Frokiaer J, Djurhuus JC, Stodkilde-Jorgensen H. In vivo measurement of T1 and T2 relaxivity in the kidney cortex of the pig--based on a two-compartment steady-state model. *Magn Reson Imaging*, 1998; 16: 933-42.

Morrison PF, Chen MY, Chadwick RS, Lonser RR, Oldfield EH. Focal delivery during direct infusion to brain: role of flow rate, catheter diameter, and tissue mechanics. *The American journal of physiology*, 1999; 277: R1218-29.

Motl S, Zhuang Y, Waters CM, Stewart CF. Pharmacokinetic considerations in the treatment of CNS tumours. *Clin Pharmacokinet*, 2006; 45: 871-903.

Muller-Bierl BM, Martirosian P, Graf H, Boss A, Konig C, Pereira PL, Schick F. Biopsy needle tips with markers - MR compatible needles for high-precision needle tip positioning. *Med. Phys.*, 2008; 35: 2273-8.

Narayana P, Abbe R, Liu SJ, Johnston D. Does loss of gray- and white-matter contrast in injured spinal cord signify secondary injury? In vivo longitudinal MRI studies. *Magn. Reson. Med.*, 1999a; 41: 315-20.

Narayana P, Fenyves D, Zacharopoulos N. In vivo relaxation times of gray matter and white matter in spinal cord. *Magn Reson Imaging*, 1999b; 17: 623-6.

Neuwelt EA. Mechanisms of disease: The blood-brain barrier. *Neurosurgery*, 2004; 54: 131-40.

Ogawa S, Lee TM. Magnetic resonance imaging of blood vessels at high fields: in vivo and in vitro measurements and image simulation. *Magn Reson Med*, 1990; 16: 9-18.

Pardridge WM. Drug delivery to the brain. *J Cereb Blood Flow Metab*, 1997; 17: 713-31.

Parekh MB, Carney PR, Sepulveda H, Norman W, King M, Mareci TH. Early MR diffusion and relaxation changes in the parahippocampal gyrus precede the onset of spontaneous seizures in an animal model of chronic limbic epilepsy. *Experimental Neurology*, 2010; 224: 258-70.

Paxinos G, Watson C. *The Rat Brain in Stereotaxic Coordinates*, 4th ed. Academic Press: San Diego, 1998.

Pedersen M, Morkenborg J, Jensen FT, Stodkilde-Jorgensen H, Djurhuus JC, Frokiaer J. In vivo measurements of relaxivities in the rat kidney cortex. *J Magn Reson Imaging*, 2000; 12: 289-96.

Pickup S, Wood AK, Kundel HL. Gadodiamide T1 relaxivity in brain tissue in vivo is lower than in saline. *Magn Reson Med*, 2005; 53: 35-40.

Pintaske J, Martirosian P, Graf H, Erb G, Lodemann KP, Claussen CD, Schick F. Relaxivity of gadopentetate dimeglumine (Magnevist), gadobutrol (Gadovist), and gadobenate dimeglumine (MultiHance) in human blood plasma at 0.2, 1.5, and 3 Tesla (vol 41, pg 213, 2006). *Investigative Radiology*, 2006; 41: 213-21.

Pishko GL, Astary GW, Mareci TH, Sarntinoranont M. Sensitivity analysis of an image-based solid tumor computational model with heterogeneous vasculature and porosity. *Annals of biomedical engineering*, 2011; 39: 2360-73.

Pollak P, Krack P, Fraix V, Mendes A, Moro E, Chabardes S, Benabid AL. Intraoperative micro- and macrostimulation of the subthalamic nucleus in Parkinson's disease. *Mov Disord*, 2002; 17 Suppl 3: S155-61.

Purcell EM, Torrey HC, Pound RV. Resonance Absorption by Nuclear Magnetic Moments in a Solid. *Physical Review*, 1945; 69: 37-8.

Rabi II, Zacharias JR, Millman S, Kusch P. A new method of measuring nuclear magnetic moment. *Physical Review*, 1938; 53: 318.

Raghavan R, Brady ML, Rodriguez-Ponce MI, Hartlep A, Pedain C, Sampson JH. Convection-enhanced delivery of therapeutics for brain disease, and its optimization. *Neurosurg Focus*, 2006; 20: E12.

Rogawski MA. Convection-enhanced delivery in the treatment of epilepsy. *Neurotherapeutics : the journal of the American Society for Experimental NeuroTherapeutics*, 2009; 6: 344-51.

Rohrer M, Bauer H, Mintonovitch J, Requardt M, Weinmann HJ. Comparison of magnetic properties of MRI contrast media solutions at different magnetic field strengths. *Invest Radiol*, 2005; 40: 715-24.

Ruoslahti E. Brain extracellular matrix. *Glycobiology*, 1996; 6: 489-92.

Sampson JH, Brady M, Raghavan R, Mehta AI, Friedman AH, Reardon DA, Petry NA, Barboriak DP, Wong TZ, Zalutsky MR, Lally-Goss D, Bigner DD. Colocalization of gadolinium-diethylene triamine pentaacetic acid with high-molecular-weight molecules after intracerebral convection-enhanced delivery in humans. *Neurosurgery*, 2011; 69: 668-76.

Sampson JH, Brady ML, Petry NA, Croteau D, Friedman AH, Friedman HS, Wong T, Bigner DD, Pastan I, Puri RK, Pedain C. Intracerebral infusate distribution by convection-enhanced delivery in humans with malignant gliomas: descriptive effects of target anatomy and catheter positioning. *Neurosurgery*, 2007; 60: ONS89-99.

Sarntinoranont M, Banerjee RK, Lonser RR, Morrison PF. A computational model of direct interstitial infusion of macromolecules into the spinal cord. *Annals of biomedical engineering*, 2003; 31: 448-61.

Sarntinoranont M, Chen X, Zhao J, Mareci TH. Computational Model of Interstitial Transport in the Spinal Cord using Diffusion Tensor Imaging. *Ann.Biomed.Eng.*2006.Aug.;34.(8.):1304.-21.Epub.2006.Jul.11., 2006; 34: 1304-21.

Saunders N, Miodownik AP. "Cu-Sn (Copper-Tin)", *Binary Alloy Phase Diagrams*. ASM Handbooks Online. ASM International, 1990.

Schenck JF. The role of magnetic susceptibility in magnetic resonance imaging: MRI magnetic compatibility of the first and second kinds. *Med. Phys.*, 1996; 23: 815-50.

Schweser F, Deistung A, Lehr BW, Reichenbach JR. Differentiation between diamagnetic and paramagnetic cerebral lesions based on magnetic susceptibility mapping. *Med Phys*, 2010; 37: 5165-78.

Schweser F, Deistung A, Lehr BW, Reichenbach JR. Quantitative imaging of intrinsic magnetic tissue properties using MRI signal phase: an approach to in vivo brain iron metabolism? *Neuroimage*, 2011; 54: 2789-807.

Smith JH, Garcia JJ. A nonlinear biphasic model of flow-controlled infusion in brain: fluid transport and tissue deformation analyses. *Journal of biomechanics*, 2009; 42: 2017-25.

Solomon I. Relaxation Processes in a System of Two Spins. *Physical Review*, 1955; 99: 559-65.

Song DK, Lonser RR. Convection-enhanced delivery for the treatment of pediatric neurologic disorders. *J Child Neurol*, 2008; 23: 1231-7.

Stanisz GJ, Henkelman RM. Gd-DTPA relaxivity depends on macromolecular content. *Magn Reson Med*, 2000; 44: 665-7.

Stopa B, Rybarska J, Drozd A, Konieczny L, Krol M, Lisowski M, Piekarska B, Roterman I, Spolnik P, Zemanek G. Albumin binds self-assembling dyes as specific polymolecular ligands. *International journal of biological macromolecules*, 2006; 40: 1-8.

Suyalatu, Kondo R, Tsutsumi Y, Doi H, Nomura N, Hanawa T. Effects of phase constitution on magnetic susceptibility and mechanical properties of Zr-rich Zr-Mo alloys. *Acta Biomater*, 2011; 7: 4259-66.

Sykova E, Nicholson C. Diffusion in brain extracellular space. *Physiol Rev*, 2008; 88: 1277-340.

Tang YW, Huang TY. Real-time feedback optimization of z-shim gradient for automatic compensation of susceptibility-induced signal loss in EPI. *Neuroimage*; 55: 1587-92.

Tao L, Nicholson C. Diffusion of albumins in rat cortical slices and relevance to volume transmission. *Neuroscience*, 1996; 75: 839-47.

Thomale UW, Tyler B, Renard VM, Dorfman B, Guarnieri M, Haberl HE, Jallo GI. Local chemotherapy in the rat brainstem with multiple catheters: a feasibility study. *Child's nervous system : ChNS : official journal of the International Society for Pediatric Neurosurgery*, 2009; 25: 21-8.

Thorne RG, Nicholson C. In vivo diffusion analysis with quantum dots and dextrans predicts the width of brain extracellular space. *Proc Natl Acad Sci U S A*, 2006; 103: 5567-72.

Toth E, Helm L, Merbach AE. Relaxivity of MRI contrast agents. *Contrast Agents I*, 2002; 221: 61-101.

Varenika V, Dickinson P, Bringas J, LeCouteur R, Higgins R, Park J, Fiandaca M, Berger M, Sampson J, Bankiewicz K. Detection of infusate leakage in the brain using real-time imaging of convection-enhanced delivery. *J Neurosurg*, 2008; 109: 874-80.

Vogelbaum MA. Convection enhanced delivery for the treatment of malignant gliomas: symposium review. *Journal of neuro-oncology*, 2005; 73: 57-69.

Wang J, Pantopoulos K. Regulation of cellular iron metabolism. *Biochem J*; 434: 365-81.

Weber T, Vroemen M, Behr V, Neuberger T, Jakob P, Haase A, Schuierer G, Bogdahn U, Faber C, Weidner N. In vivo high-resolution MR imaging of neuropathologic changes in the injured rat spinal cord. *AJNR*, 2006; 27: 598-604.

Weiss N, Miller F, Cazaubon S, Couraud PO. The blood-brain barrier in brain homeostasis and neurological diseases. *Biochim Biophys Acta*, 2009; 1788: 842-57.

Yang CG, Deng WR, Alagappan V, Wald LL, Stenger VA. Four-Dimensional Spectral-Spatial RF Pulses for Simultaneous Correction of B(1)+ Inhomogeneity and Susceptibility Artifacts in T(2)\*-Weighted MRI. *Magn. Reson. Med.*; 64: 1-8.

Yin D, Forsayeth J, Bankiewicz KS. Optimized cannula design and placement for convection-enhanced delivery in rat striatum. *J Neurosci Methods*, 2010; 187: 46-51.

Yushkevich PA, Piven J, Hazlett HC, Smith RG, Ho S, Gee JC, Gerig G. User-guided 3D active contour segmentation of anatomical structures: significantly improved efficiency and reliability. *Neuroimage*, 2006; 31: 1116-28.

Zimmerman JR, Brittin WE. Nuclear Magnetic Resonance Studies in Multiple Phase System - Lifetime of a Water Molecule in an Adsorbing Phase on Silica Gel. *J. Phys. Chem.*, 1957; 61: 1328-33.

Zimmermann DR, Dours-Zimmermann MT. Extracellular matrix of the central nervous system: from neglect to challenge. *Histochem Cell Biol*, 2008; 130: 635-53.

## BIOGRAPHICAL SKETCH

Garrett William Astary was born in Conyers, Georgia. He earned his Bachelor of Science degree from the Georgia Institute of Technology in Biomedical Engineering graduating summa cum laude in 2006. While attending Georgia Tech, he performed undergraduate research in the Cardiovascular Fluid Mechanics Laboratory headed by Dr. Ajit Yoganathan. In fall of 2006, he moved to Gainesville, Florida to pursue his doctoral degree at the University of Florida in Biomedical Engineering under the mentorship of Drs. Malisa Sarntinoranont and Thomas H. Mareci. While at the University of Florida, he used Magnetic Resonance Imaging to study the potential of convection-enhanced delivery for treating epilepsy. Additionally he has contributed to the development of a new metal alloy that has similar magnetic properties to brain tissue minimizing distortions in MR images. He received his Ph.D. in Biomedical Engineering from the University of Florida in fall of 2011.